USGS Award Number: G14AP00067

Assessing Lateral Spread Hazards in Areas Prone to Great and Long-Duration Earthquakes

Michael D. Bunn
Graduate Student
School of Civil and Construction Engineering
Oregon State University
101 Kearney Hall
Corvallis, OR 97331
email: bunnmi@oregonstate.edu

Daniel T. Gillins, Ph.D., P.L.S.
Assistant Professor
101 Kearney Hall
School of Civil and Construction Engineering
Oregon State University
Corvallis, OR 97331
541-737-4865 (voice)
541-737-3052 (fax)
email: dan.gillins@oregonstate.edu

Term of Award:
06/23/2014 – 06/22/2015

Abstract

Lateral spread is a pervasive type of liquefaction-induced ground failure that occurs on gentle slopes or near free-faces, such as river channels. Resulting horizontal displacements can reach up to several meters, and can be considerably damaging to foundations, bridges, roadways, pipelines, etc. In the 1990s, Bartlett and Youd (1992a, 1995) introduced an empirical model for predicting liquefaction-induced lateral spread displacements. Since then, this model has become popular in engineering practice; numerous additional empirical models have also been developed.

This report studied case histories of lateral spreading due to great (moment magnitude 8.0 or greater) subduction zone earthquakes, which are the product of large-scale ruptures along the boundary where one tectonic plate descends beneath another. These complex ruptures are capable of producing enormous energy, and strong shaking for much longer durations than those produced by more common crustal earthquakes. Although existing empirical models are based on large databases of lateral spreading case histories, a significant majority of these databases involve major (moment magnitude 6.0 to 8.0) crustal earthquakes. Furthermore, the only two subduction zone earthquakes incorporated in the case history databases for existing empirical models occurred prior to 1970, and lack ground motion recordings.

To overcome this gap in the case history databases, available lateral spreading case history data from four great earthquakes (Alaska 1964, Peru 2007, Chile 2010, and Japan 2011) was compiled to initiate the creation of a great earthquake lateral spread case history (GELCH) database. An evaluation of the case histories from the GELCH database showed that lateral spreading occurred at locations having corrected standard penetration

test (SPT) $(N_1)_{60}$ values less than 15, with the exception of two sites previously identified by Bartlett and Youd (1995). In addition, this research found that popular empirical models (e.g., from Rauch and Martin (2000), Youd et al. (2002), Zhang et al. (2004), and Gillins and Bartlett (2014)) all failed to accurately predict lateral spread displacements at every case history in the GELCH database. These failures were likely caused by the complex ruptures of the subduction zone earthquakes, which presented uncertainty in the form of duration of shaking and seismic directivity. Based on these findings, this report provided recommendations for the types of critical data needed to further populate the GELCH database, and gave ideas for how to develop a new empirical model that is capable of predicting accurate lateral spread displacements due to great subduction zone earthquakes.

Contents

Chapter 1: Introduction

Definition of Liquefaction-Induced Lateral Spreading

Soil liquefaction occurs when saturated soil loses shear resistance during cyclic loads generated by earthquakes. Cohesionless soils that are saturated, loosely deposited, young, and poorly cemented are most susceptible to liquefaction. When large loads are rapidly applied or repeated many times, excess pore-water pressure in saturated soil will build up as the soil does not have sufficient time to dissipate the pressure. More pore-water pressure builds up when loosely deposited soils attempt to reach a denser state under loading. Such undrained conditions result in a decrease of the effective stresses of the soil, causing the soil to lose shear resistance and behave more like a liquid.

When liquefaction occurs, a number of different types of ground failure may occur, generally depending on the topography. On flat ground, blocks of mostly intact surficial soil above a liquefied layer may collide and jostle during ground shaking, opening cracks at the ground surface. On steep slopes, large blocks of mostly intact soil above the liquefied layer may be violently thrown tens of meters, resulting in catastrophic landslide displacements known as flow failures. But on gentle slopes (typically from 0.3 to 5%), the blocks of mostly intact, surficial soil above the liquefied layer of soil may slowly displace down slope or towards a free-face (e.g., river channel or sudden depression). For example, see Figure 1.1. These displacements, known as lateral spreads, are the focus of this research. Unlike flow failures, in which soil masses may achieve high velocities and travel large distances, lateral spreads tend to move slowly and displace no more than several meters.

Despite the less aggressive ground failure associated with it, lateral spreading is more pervasive, having potential to inflict the greatest amount of damage during an earthquake (McCulloch & Bonilla, 1970). Flow failures are rare, and the built-up environment is less commonly located on steep terrain. Lateral spreading does not threaten human life as much as tsunamis or landslides, but it can be considerably damaging to foundations, bridges, roadways, pipelines, etc. Losses in soil density can lead to buoyant uplift in subsurface infrastructure and lateral movement can shear deep foundations.

Because of its pervasiveness, the prediction of lateral spreading has become an important topic in geotechnical earthquake engineering. Knowing where lateral spreading is a risk and having an estimate of its severity, may indicate if, and to what extent, mitigation is necessary for a particular construction site. Many popular models in engineering practice for predicting lateral spread displacements were derived empirically by studying earthquake case histories. Empirical models are only applicable to the earthquakes and ground conditions from which they were developed.

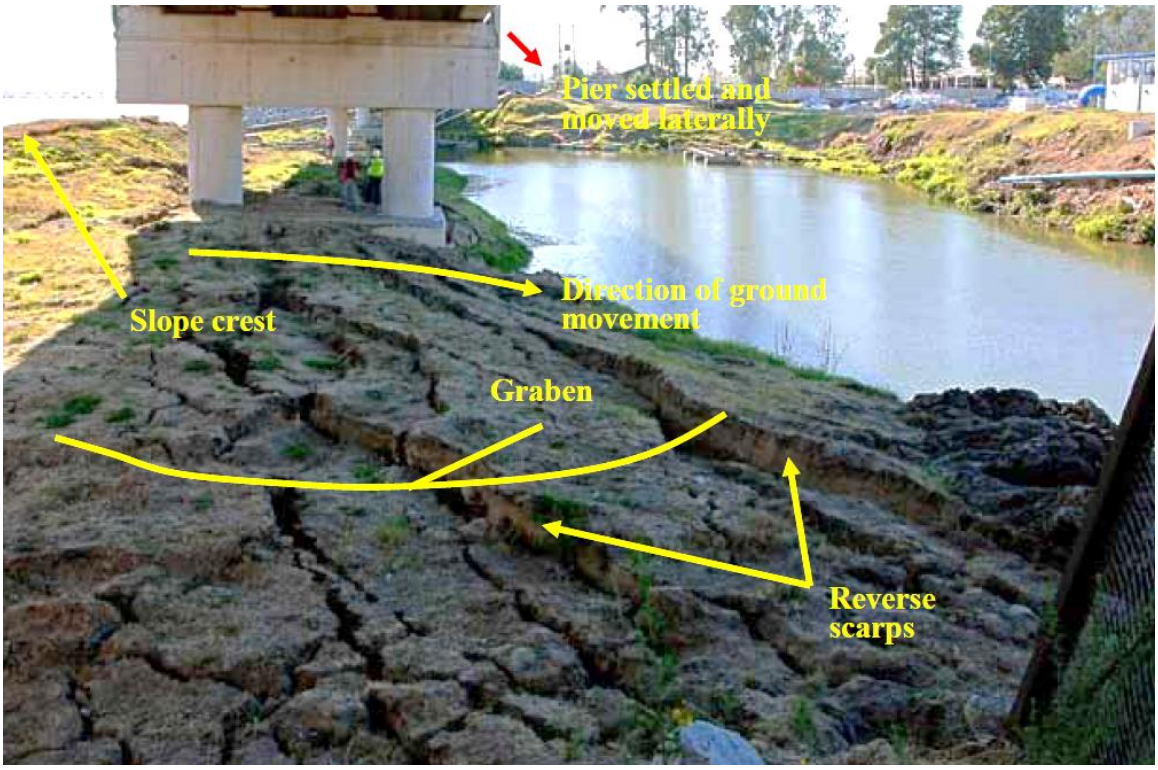

Figure 1.1: Photograph showing the formation of discrete soil blocks caused by lateral spreading (From FHWA 2010).

Different Approaches for Predicting Lateral Spread Displacements

A number of different approaches exist for predicting lateral spread displacements. Some techniques entail numerical analysis, while others are empirical, such as those listed in Table 1.1. What is important to understand is that empirical methods rely on observed lateral spreading during previous earthquakes, while numerical methods focus on the expected underlying physical relationships and laboratory testing. Some methods include aspects of both techniques, and will hereafter be referred to as semi-empirical. Semi-empirical and fully empirical models tend to be easier to understand and apply, and generally receive more use in the engineering practice

(SCDOT 2010, ODOT 2014, among others). For the reasons that they are used further and that they are fundamentally vested in data from previous earthquakes, empirical and semi-empirical forms, and not numerical methods, will be focus of this paper.

Table 1.1: Abridged list of techniques used to estimate lateral spread displacements

Technique	Source
Empirical approaches based on case histories	Youd and Perkins (1987) Hamada et al. (1987) Bartlett and Youd (1995) Rauch and Martin (2000) Youd et al. (2002) Bardet et al. (2002) Gillins and Bartlett (2014)
Semi-empirical approaches based on case histories and laboratory results	Faris et al. (2004) Zhang et al. (2004)

Problem Statement

This paper focuses on studying case histories of lateral spreading due to great (moment magnitude 8.0 or greater) subduction zone earthquakes. Although the empirical and semi-empirical models above are based on large databases of lateral spreading case histories, a significant portion of these databases involve major (moment magnitude 6.0 to 8.0) crustal earthquakes. It is unclear if the models listed in Table 1.1 are appropriate or could be extrapolated for predicting lateral spread displacements due to great subduction zone earthquakes.

The reason why it is important to discriminate between great and major crustal earthquakes is that they are each driven by different geological processes. Great subduction zone earthquakes are the product of large-scale ruptures along the boundary where one tectonic plate descends beneath another. Such earthquakes release significant energy with moment magnitudes equal to 8.0 or greater. Crustal earthquakes occur on faults located within a tectonic plate and generally have lower magnitudes and produce less severe shaking. Besides stronger shaking, subduction zone earthquakes rupture over greater distances, resulting in significantly longer durations and ground motions affecting larger regions. To compare durations, strong ground motions during the 1989 Loma Prieta earthquake, a major crustal event along the San Andreas Fault, lasted approximately 8 to 15 seconds (Plafker and Galloway 1989). In dramatic contrast, strong ground motions during the 2010 Maule, Chile, Earthquake, a great subduction event, lasted up to two minutes in some locations (Boroschek et al. 2010).

The motivation for studying lateral spreading, specifically with a focus on subduction zone earthquakes is based on the combination of risk and a lack of preparedness. In the Pacific Northwest, and various other regions worldwide, large population centers are located in close proximity to subduction zones. Offshore from Northern California to British Columbia, the Cascadia Subduction Zone could produce an earthquake with a magnitude up to 9.0 that shakes for as long as four to six minutes (DOGAMI, 2013). Such a great event would impart catastrophic damage to a large region. While this research does not directly address regional preparedness, it does allow for future work in that field.

Research Steps

This paper presents the following research on lateral spreading during great subduction zone earthquakes:

1. Available lateral spreading case history data was compiled to initiate the creation of the Great Earthquake Lateral Spread Case History (GELCH) database. The database has been organized into a geographic information system (GIS) to aid in visualization and to better relate data obtained from different sources. Case histories were compiled in this database from the following 4 earthquakes: Alaska 1964 (M9.2), Peru 2007 (M8.0), Chile 2010 (M8.8.), and Japan 2011 (M9.0).
2. The GELCH database was examined to determine if lateral spreading had occurred at locations with corrected standard penetration test (SPT) $(N_1)_{60}$ values exceeding 15. This step was important to determine the validity of the T_{15} parameter used by several of the empirical lateral spread prediction methods, as discussed hereinafter.
3. The GELCH database was used to assess the performance of extrapolating the Rauch and Martin (2000), Youd et al. (2002), Zhang et al. (2004), and Gillins and Bartlett (2014) empirical methods for predicting lateral spread displacements during great subduction zone events with M > 8.0.
4. Recommendations were made regarding future research of lateral spreading during great subduction zone earthquakes.

Report Organization

Chapter 2 of this report reviews, with some detail, previous empirical and semi-empirical models for predicting lateral spread displacements. The review explains how to apply each model and is meant to explain why this research is necessary. Chapter 3 presents compiled case histories of lateral spreading during great subduction zone earthquakes. This chapter presents background on the location of each case history and its subduction zone earthquake. Existing empirical and semi-empirical models are then applied for predicting lateral spreading at each of the new case histories. The results of chapter 3 are then discussed in chapter 4, along with any proposed modifications to the existing models, and discussion of lessons learned. Finally, chapter 5 presents the conclusions and key findings of this work.

Chapter 2: Literature Review

Introduction

The purpose of this chapter is to summarize previous empirical and semi-empirical methods for predicting lateral spread displacements. The writing has been organized chronologically, with the one exception being for the work of Bartlett and Youd (1992a, 1995), Youd et al. (2002), Bardet et al. (2002), and Gillins and Bartlett (2014), which share many features, and we believed that they are best described together. To further improve organization, a listing of the variables presented may be found in Table 2.5 at the close of this chapter. The table includes variable names, units, and associated authors, and may serve as a useful reference during this, and later chapters.

Hamada et al. (1986)

The first major effort made toward predicting ground displacements associated with lateral spreading came in Hamada et al. (1986). Hamada et al. (1986) began by using aerial photos from before and after the 1964 Niigata, Japan, and the 1983 Nihonkai-Chubu, Japan, earthquakes to map horizontal ground displacements caused by each event. The maps consisted of numerous displacement vectors, illustrating the magnitude and direction of movement. Hamada et al. (1986) then used borehole data from near the mapped displacements to identify liquefiable soil layers and evaluated this information to develop cross-sections illustrating the extent of each layer. By comparing the mapped vectors with the cross-sections, Hamada et al. (1986) were able to identify where surficial soils had appeared to displace as discrete blocks.

Treating the soil as discrete units, Hamada et al. (1986) were able to determine an average ground slope, Θ (%), the thickness of liquefiable layers, H (m), and an average displacement, D (m), for each block. A regression analysis was then performed on the averaged values from each block to produce equation 2.1. The ground slope used in the equation is taken to be the greater of the slope beneath the liquefiable layer and the slope of the ground surface.

$$D \approx 0.75\sqrt[2]{H}\sqrt[3]{\theta} \tag{2.1}$$

Hamada et al. (1986) compared actual displacement values against those predicted using equation 2.1, and found that roughly 60 percent of the predicted values were between one-half to twice their observed value. According to Hamada and O'Rourke (1992), this scatter in data is likely influenced by poor correlation between measured displacements and the slope of the liquefied layer. Hamada and O'Rourke (1992) present several possible sources of error in deriving equation 2.1, including the incorporation of borehole data obtained more than 100 meters from the observed displacements and difficulties estimating the slope beneath the liquefiable layer. After limiting borehole data to that within 25 meters of displacements and extending the distance over which the ground slopes were calculated, Hamada and O'Rourke (1992) obtained improved correlations between the thickness of each liquefied layer and displacement, with the poor relationship between ground slopes and displacements being maintained.

Youd and Perkins (1987)

At nearly the same time as Hamada et al. (1986), Youd and Perkins (1987) were working to develop an empirical method of assessing the expected severity of damage caused by liquefaction so that they could perform regional hazard mapping. They began by defining a parameter called liquefaction severity, *S* (inches), which describes measured displacements from previous earthquakes, and *R* (km), which represents the distance from a site to the nearest seismic energy source. Because numerous values may be measured at a single location, Youd and Perkins then defined the liquefaction severity index (*LSI*) as the largest of the observed or expected measurements.

Youd and Perkins identified several factors that were likely to influence the *LSI*, displayed in Table 2.1, and applied assumptions to normalize data from each earthquake. The LSI then became a function of only ground motions and distance from the seismic energy source. Based on the close relationship between ground motions and earthquake magnitude, and the logarithmic attenuation of displacements with increased distance, Youd and Perkins further simplified the factors. The final factors were then fit to the data using a multiple linear regression analysis to create equation 2.2.

$$\log LSI = -3.49 - 1.86 \log R + 0.98 M_w \qquad (2.2)$$

In applying equation 2.2, it is important to consider the assumptions made, which are stated in the third column of Table 2.1. Most of the assumptions were made regarding the geological setting, meaning that the equation should only be used in the regions similar to the western United States having been deposited relatively recently.

Table 2.1. Estimated susceptibility of sedimentary deposits to liquefaction during strong seismic shaking (after Youd and Perkins 1978)

Type of Deposit (1)	General Distribution of Cohesionless sediments in deposits (2)	Likelihood that Cohesionless Sediments, When Saturated, Would be Susceptible to Liquefaction (by Age of Deposit)			
		<500 yr (3)	Holocene (4)	Pleistocene (5)	Pre-Pleistocene (6)
(a) Continental Deposits					
River Channel	Locally Variable	Very High	High	Low	Very Low
Floodplain	Locally Variable	High	Moderate	Low	Very Low
Alluvial Fan and Plain	Widespread	Moderate	Low	Low	Very Low
Marine Terraces/ Plains	Widespread	-----	Low	Very Low	Very Low
Delta and Fan-delta	Widespread	High	Moderate	Low	Very Low
Lacustrine and Playa	Variable	High	Moderate	Low	Very Low
Colluvium	Variable	High	Moderate	Low	Very Low
Talus	Widespread	Low	Low	Very Low	Very Low
Dunes	Widespread	High	Moderate	Low	Very Low
Loess	Variable	High	High	High	Unknown
Glacial Till	Variable	Low	Low	Very Low	Very Low
Tuft	Rare	Low	Low	Very Low	Very Low
Tephra	Widespread	High	High	?	?
Residual Soils	Rare	Low	Low	Very Low	Very Low
Sebkha	Locally Variable	High	Moderate	Low	Very Low
(b) Coastal Zone					
Delta	Widespread	Very High	High	Low	Very Low
Esturine	Locally Variable	High	Moderate	Low	Very Low
Beach					
High Wave Energy	Widespread	Moderate	Low	Very Low	Very Low
Low Wave Energy	Widespread	High	Moderate	Low	Very Low
Lagoonal	Locally Variable	High	Moderate	Low	Very Low
Fore Shore	Locally Variable	High	Moderate	Low	Very Low
(c) Artificial					
Uncompacted Fill	Variable	Very High	-----	-----	-----
Compacted Fill	Variable	Low	-----	-----	-----

Bartlett and Youd (1992a, 1995), Youd et al. (2002), Bardet et al. (2002), and Gillins and Bartlett (2014)

Several years after the works of Hamada et al. (1986) and Youd and Perkins (1987), Bartlett and Youd (1992a, 1995) acknowledged that both methods failed to address many of the factors known to contribute to liquefaction-induced permanent ground deformations. In order to produce a more robust approach, they compiled case histories from lateral spreading during several American and Japanese earthquakes and added further geological, topographical, and geotechnical factors to what was already included in the previous two analyses.

In total, the case history database included 467 displacement vectors, with 337 from Japan and 111 from the United States. For the Japanese earthquakes, horizontal ground displacements were taken from the work of Hamada et al. (1986) and, as mentioned earlier, were measured using photogrammetric techniques. For the American earthquakes, displacement values came from different methods, ranging in complexity from taped distances during ground surveys to photogrammetry. Based on the different methods, Bartlett and Youd (1992a, 1995) state a range in accuracy of the displacement vectors from ±0.01 m to ±0.75m. The added geological, topographical and geotechnical factors came from seismological reports, topographical maps and subsurface investigations. Inverse distance weighting was then used to tie each factor to the location of an observed lateral spreading displacement vector.

Noticing that the Japanese data came from the seismically similar 1964 Niigata and 1983 Nihonkai-Chubu earthquakes, Bartlett and Youd (1992a, 1995) were able to produce preliminary multiple linear regression (MLR) models that normalized

seismological parameters and allowed for the geological, topographical and geotechnical factors to be examined independently. From this study, Bartlett and Youd (1992a, 1995) found that the lateral spreading case history database could be divided into two categories based on the topography: (1) lateral spreads that occurred toward a free face (e.g., abrupt change in elevation such as a river channel or a steep depression); and (2) lateral spreads that occurred on a gradual slope without a free face. For the free face cases, the magnitude of ground deformation increased with proximity to the free face, prompting Bartlett and Youd (1992a, 1995) to create a descriptive parameter that could then be incorporated into their statistical analyses. The result was the free face ratio, W (%), which is defined by equation 2.3 with the height of the free face, H, and the horizontal distance from the base of the free face to the displaced ground, L.

$$W\ (\%) = 100H\ /\ L \tag{2.3}$$

Bartlett and Youd (1992a) also defined ground slope, S (%), for several relationships between topography and the location of displacements. In its simplest form, the ground slope used for a long uniform slope is the change in elevation divided by its corresponding change in the horizontal direction. Although these long uniform slopes do occur, it is more common for natural slopes to exhibit varying gradients, with each distinct slope being bounded by a toe, at its bottom, and a crest, at its top. To determine whether a displacement is affected by a particular slope, Bartlett and Youd (1992a, 1995) plotted lower and upper lines of influence as a function of the change in elevation

between slope toe and crest. The ground slope parameter for a given displacement is then computed based on its location relative to the toe and crest.

Bartlett and Youd (1992a, 1995) also found a relationship between ground displacements and the thickness of the liquefied soil layer. To evaluate this relationship, values of T_{10}, T_{15} and T_{20} (all in meters), were computed at each case history and were defined as the cumulative thickness of all saturated and cohesionless (having a clay content of less than 15%) layers in a soil profile with an SPT $(N_1)_{60}$ of less than 10, 15 and 20, respectively. Through regression analyses, Bartlett and Youd (1992a, 1995) found that the T_{15} parameter provided not only the best fit with predicting lateral spread displacements, but also aligned with the observation that lateral spreading typically only occurred in soils having $(N_1)_{60} < 15$ for earthquake magnitudes, M, less than 8.0. However, Bartlett and Youd did note that for the M9.2 1964 Alaska Earthquake, the only subduction zone earthquake in their case history database, lateral spreading was observed at two sites where $(N_1)_{60} > 15$ (i.e., in other words, at sites where $T_{15} = 0$).

In addition to free face ratio and thickness of liquefied layers, Bartlett and Youd (1992a, 1995) also noticed correlations between horizontal displacements and both the average fines content, F_{15} (%), and mean grain size, $D50_{15}$ (mm), of the T_{15} layer. The parameters were then analyzed together with other seismological and topographical variables to produce a multilinear regression model for predicting horizontal displacements due to lateral spreading, D_H.

Following the publishing of Bartlett and Youd (1992a, 1995) and widespread use of their MLR, Youd et al. (2002) introduced a new set of equations that both revised and expanded upon the earlier model. To first address errors associated with the case history

database of Bartlett and Youd (1992a, 1995), Youd et al. (2002) corrected several erroneous estimates of ground displacement and removed sites where the presence of structures had inhibited lateral movement. Youd et al. (2002) then introduced several new case histories, predominately incorporating sites where coarse-grained soils had liquefied.

Aside from the case history database, Youd et al. (2002) changed the form of both the $D50_{15}$ and R parameters. To improve the model's performance with coarse-grained soils, the logarithm of $D50_{15}$ was now incorporated into the regression. Additionally, R, the distance to the nearest seismic energy source, was adjusted to become a function of earthquake magnitude to avoid overestimates of displacement as R became small. The adjusted distance, R^*, is defined in the equations below.

$$R^* = R_o + R \tag{2.4}$$

$$R_o = 10^{(0.89M - 5.64)} \tag{2.5}$$

The parameters, including both R^* and R, were then analyzed using a multiple linear regression, like that of Bartlett and Youd (1992a, 1995), to produce the following equations that have become quite popular in engineering practice.

The model for free faces:

$$\begin{aligned} \log(D_H) = {} & -16.713 + 1.532M - 1.406 \log R^* - 0.012R + 0.592 \log W \\ & + 0.540 \log T_{15} + 3.413 \log(100 - F_{15}) \\ & - 0.795 \log(D50_{15} + 0.1\ mm) \end{aligned} \tag{2.6}$$

And the model for sites with gently sloping ground:

$$\log(D_H) = -16.213 + 1.532M - 1.406\log R^* - 0.012R + 0.338\log S + 0.540\log T_{15} + 3.413\log(100 - F_{15}) - 0.795\log(D50_{15} + 0.1\ mm) \quad (2.7)$$

As in the model of Youd and Perkins (1987), distance to the seismic energy source is represented as *R* (km), but horizontal ground displacement is now written as D_H (m). The results of the Youd et al. (2002) model were verified in a manner similar to how Hamada et al. (1986) had done prior, with 88.4 percent of predicted values being between one-half to twice their actual value. Further presentation of the Youd et al. (20002) model's ability to match the data is expressed in the combined MLR's coefficient of determination (r^2) being 82.6 percent, and the standard deviation of the model, $\sigma_{logDH,}$ equal to 0.1970.

Bardet et al. (2002) set out to perform regional hazard mapping using the MLR of Bartlett and Youd (1992a, 1995), but found that the lack of available *D50* and fines content data introduced a large amount of uncertainty to their analysis. In attempt to avoid this problem, they removed both parameters and performed a new statistical regression using the Bartlett and Youd (1995) case history database. The regression was performed on two datasets, the first including all displacements from Bartlett and Youd (1995), and the second including only displacements smaller than 2 meters. The purpose behind this division was to compare the behavior of smaller displacements (dataset B),

which could be mitigated through engineering, with the larger displacements (dataset A), which were considered to result in total loss.

The regressed model for dataset A:

$$\log(D_H + 0.1) = -6.815 - 0.465 + 1.017M - 0.278\log R - 0.026R + 0.497\log W + 0.454\log S + 0.558\log T_{15} \quad (2.8)$$

And the regressed model for dataset B

$$\log(D + 0.1) = -6.747 - 0.162 + 1.001M - 0.289\log R - 0.021R + 0.090\log W + 0.203\log S + 0.289\log T_{15} \quad (2.9)$$

The results of the regression show that there is no benefit to using one equation over the other, as they demonstrate similar accuracy, and Bardet et al. (2002) recommends that they be used interchangeably. Comparison of these results to the Bartlett and Youd (1992a, 1995) model demonstrates that accuracy is generally lost by removing the $D50_{15}$ and F_{15} parameters.

In addition to the removal of the particle size descriptors, is also evident that each equation includes both free face and ground slope parameters. During application, Bardet et al. expect the user to assume a coefficient of zero for the topographic descriptor that they are not using. For example, if a free face condition is assumed for the first equation, the *S* coefficient of 0.454 would be changed to 0.

To address the same problem as Bardet et al. (2002) (i.e., *D50* and fines content are at times not reported on borehole logs), Gillins and Bartlett removed the $D50_{15}$ and F_{15} parameters and replaced them with indices based on the qualitative soil descriptions

included in the boring logs. To do so, soil indices, *SI*, were assigned as values ranging from 1 through 6 meant to describe all expected soil types. Corresponding *SI* values and soil types are presented in Table 2.2.

Table 2.2: Descriptions of T_{15} layers in Youd et al. (2002) database (adapted from Gillins and Bartlett, 2014).

Typical Soil Descriptions in Database	General USCS Symbol	Soil Index *SI*
Silty gravel with sand, silty gravel, fine gravel	GM	1
Very coarse sand, sand and gravel, gravelly sand	GM-SP	2
Coarse sand, sand with some gravel	SP	2
Sand, medium to fine sand, sand with some silt	SP-SM	3
Fine sand, sand with silt	SM	4
Very fine sand, silty sand, dirty sand, silty/clayey sand	SM-ML	4
Sandy silt, silt with sand	ML	5
Nonliquefiable material (not part of T_{15})	CL	6

Selection of an appropriate soil index for each soil layer is done using Table 2.2. Generally, a user would compare their soil description to the typical description provided, and possibly, with the provided USCS symbol.

To incorporate the soil index values into a multiple linear regression, Gillins and Bartlett (2014) defined a new variable known as x_i (unitless), which is defined as the thickness of the layers in the site profile that comprise T_{15} with $SI = i$ divided by the total cumulative thickness of T_{15}. If, for example, a soil index of 3 is not represented in a boring, the value of the variable x_3 would equal zero. The resulting equation is presented below. The coefficients result from a multiple linear regression using the Youd et al. (2002) database.

The model for free faces:

$$\log D_H = -8.208 - 0.344 + 1.318M - 1.073 \log R^* - 0.016R + 0.445 \log W + 0.592 \log T_{15} - 0.683x_1 - 0.200x_2 + 0.252x_3 - 0.040x_4 - 0.535x_5 \quad (2.10)$$

And the model for sites with gently sloping ground:

$$\log D_H = -8.208 + 1.318M - 1.073 \log R^* - 0.016R + 0.337 \log S + 0.592 \log T_{15} - 0.683x_1 - 0.200x_2 + 0.252x_3 - 0.040x_4 - 0.535x_5 \quad (2.11)$$

As done prior, the performance of the above equations was evaluated by comparing observed values with the values predicted by each equation. For the Gillins and Bartlett (2014) model, 81.4% of the predicted displacements fall between one-half and twice their corresponding observed value. These results are only slightly less accurate than those of Youd et al. (2002), and are an improvement over the model created by simply removing $D50_{15}$ and F_{15}. For the Gillins and Bartlett (2014) model, (r^2) is 79.0 percent, and $\sigma_{logDH,}$ equals 0.2232.

Rauch and Martin (2000)

Working from the efforts of Bartlett and Youd (1992a, 1995) and Hamada et al. (1986), Rauch and Martin (2000) presented an alternative empirical method for estimating lateral spread displacements. The Empirical Prediction of Liquefaction-induced Lateral Spreads (EPOLLS) model redefined the case histories examined by Bartlett and Youd (1995) by adopting a similar approach to Hamada et al. (1986) that was less concerned with individual displacement vectors and more interested in the deformation of discrete soil masses. Rauch and Martin decided to combine multiple displacement vectors that Bartlett and Youd modeled as individual case histories to a single, large soil block of displacement. The result was a reduction of case studies from the 467 of Bartlett and Youd (1992a, 1995) to the 71 of EPOLLS, despite Rauch and Martin having added further cases to the database. This different approach to displacements also means that the equations developed by Rauch and Martin (2000) predict single average displacements for a soil mass, rather than the numerous displacement vectors that might result from a Bartlett and Youd (1992a, 1995) analysis.

Like the methods of Bartlett and Youd (1992a, 1995) and Youd and Perkins (1987), Rauch and Martin (2000) identified numerous parameters that were considered to influence lateral spread displacements. The three major categories identified included seismological, topographical and geotechnical parameters, with the latter incorporating the most detailed site information. These parameters are displayed in Table 2.3, and were then carried over to a statistical analysis, with Rauch and Martin performing several analyses to create a multiple-tiered model for estimating horizontal ground displacements. With their model, the underlying idea was that each tier could incorporate more detail than its predecessor, and that after evaluation the tiers could be added together to form predictions based on the maximum amount of information available for a particular case study.

Table 2.3: Definition of EPOLLS parameters (From Rauch and Martin, 2000).

Variable	Units	Definition
M_w	-	Moment magnitude of earthquake
R_f	km	Shortest horizontal distance from site to surface projection of fault rupture or zone of seismic energy release
A_{max}	g	Peak horizontal acceleration at ground surface of site of site that would occur in absence of excess pore pressures liquefaction generated by earthquake
T_d	s	Duration of strong earthquake motions at site, defined as time between first and last occurrence of surface acceleration $\geq$0.05 g
L_{slide}	m	Maximum horizontal length from head to toe of lateral spread in prevailing direction of movement
S_{top}	%	Average slope across surface of lateral spread, measured as change in elevation over distance from head to toe
H_{face}	m	Height of free face, measured vertically from toe to crest of free face
Z_{FSmin}	m	Average depth to minimum factor of safety in potentially liquefiable soil
Z_{liq}	m	Average depth to top of liquefied soil

The first tier of the model, Regional-EPOLLS (R-EPOLLS), incorporates mostly data relating to the seismology surrounding a study site and is generally the easiest value to compute. Much like the previously described equations, Rauch and Martin (2000) performed a multiple linear regression to obtain the coefficients for the following equation. Descriptions of the parameters used may be found in Table 2.3.

$$D_R = (613M_W - 13.9R_f - 2420A_{max} - 11.4T_d)/1000 \quad (2.12)$$

$$Avg_{Horz} = (D_R - 2.21)^2 + 0.149$$

Alternative to the previously mentioned methods, Rauch and Martin (2000) used a square-root, not logarithmic, relationship between predicted displacements and the various independent variables. Because of this difference, Rauch and Martin (2000) added the 0.149 in an attempt to minimize potential bias. Additionally, the authors point out that the negative influence of T_d and A_{max} is unexpected, as an increase in earthquake duration or ground acceleration would be expected to produce more displacement, not less. Despite the negative signs being theoretically problematic, they are maintained in the model because they produce the best fit to the database. Note that this is the first empirical model presented that incorporates the parameters T_d and A_{max}.

The second tier of the model, Site-EPOLLS (S-EPOLLS), was developed to add further detail to analyses using R-EPOLLS if additional data was available. The database of 71 case histories was reduced to 57 where adequate topographic information was available. Several topographic parameters were then added to equation 2.12 and new coefficients were determined by fitting the expanded equation to the reduced database. The result of the regression is presented below. Once again, the parameters are defined in Table 2.3.

$$D_S = (0.523L_{slide} + 42.3S_{top} + 31.3H_{face})/1000 \quad (2.13)$$

$$Avg_{Horz} = (D_R + D_S - 2.44)^2 + 0.111$$

Like the equation before it, equation 2.13 has been adjusted for bias associated with the square-root relationship. In developing the S-EPOLLS model, Rauch and Martin (2000) experimented with several additional variables, including *Slide_Area*, *Direct_Slide*, and *Free_Face?*. The latter, term for example is simply 1 when free faces are present, or 0 when they are absent. It was omitted from the final model because it was found not be statistically significant per the regression results. *Slide_Area* and *Direct_Slide*, the direction of movement, were removed from the model because they were difficult to determine in many cases. The selected parameters for S-EPOLLS are similar to those used by Bartlett and Youd (1992a, 1995) and Youd et al. (2002), with L_{slide} and H_{face}, serving a similar purpose as the free face ratio, *W*.

The final tier of the model, Geotechnical-EPOLLS (G-EPOLLS), is meant for sites where geotechnical investigations have been performed. The database used to fit G-EPOLLS was reduced to include 44 case studies where adequate information was available and the following equation was produced. Factors of safety against liquefaction, necessary for calculating Z_{FSmin} and Z_{liq}, were determined based on the guidelines of the NCEER Workshop on Evaluation of Liquefaction Resistance of Soils (NCEER 1997).

$$D_G = (50.6Z_{FSmin} - 86.1Z_{liq})/1000 \quad (2.14)$$

$$Avg_{Horz} = (D_R + D_S + D_G - 2.49)^2 + 0.124$$

The ability of each of equations 2.12 through 2.14 to fit their respective case histories improves as the number of descriptive parameters increases, and as with the previous methods, extrapolation or use of the models at sites that are not similar to those in the case history database is not recommended.

Semi-Empirical Methods

The methods discussed thus far have all been empirical, meaning that their derivation comes solely from the ability to correlate various variables to observed lateral spread displacements. Another way to predict these displacements comes in the form of semi-empirical methods, which are developed as some combination of statistical regression and underlying physical relationships. The first of these methods was presented by Zhang et al. (2004) primarily to address failure of existing models to incorporate laboratory knowledge, but also to introduce a method that used data from both the SPT and the increasingly popular cone penetration test (CPT).

Zhang et al. (2004) first used the method of Youd et al. (2001) to determine the factor of safety against liquefaction triggering, *FS*, and the relative density, D_r, of soils from SPT results. Using the laboratory-developed relationship from Ishihara and Yoshimine (1992) and Seed (1979), a correlation was then found for using *FS* and *Dr* to estimate maximum cyclic shear strain, γ_{max}. Zhang et al. then developed a new parameter known as the lateral displacement index (*LDI*), defined according to the equation below. As can be seen, the *LDI* is found by integrating γ_{max} for all potentially liquefiable layers

(i.e., any layer with *FS* less than 2.0) at a site. Zhang et al. recommended that the maximum depth to be considered (i.e., Z_{max}) in equation 2.15 is never more than 23 m.

$$LDI = \int_0^{Z_{max}} \gamma_{max} dz \tag{2.15}$$

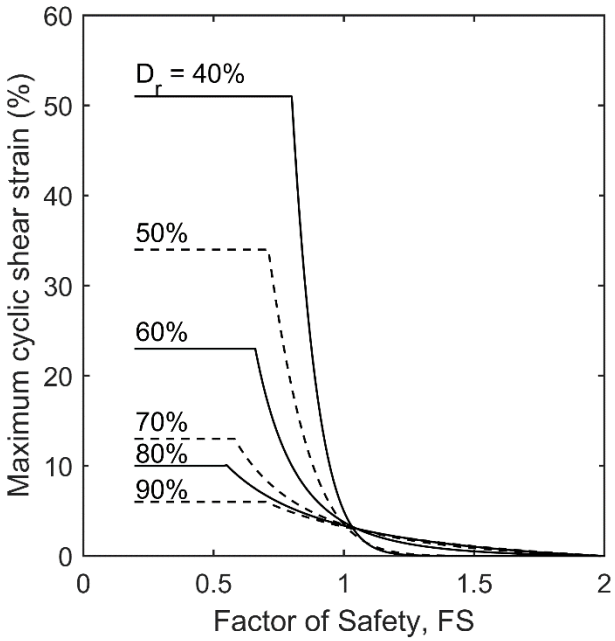

Figure 2.2: Relationship between maximum cyclic shear strain and factor of safety for different relative densities of clean sands (From Zhang et al. 2004).

This equation assumes that lateral displacements are closely related to the potential for liquefaction at a site. The *LDI* is computed in units of distance, but its purpose is solely to indicate a relative magnitude of lateral displacement to be expected.

In order to predict the lateral displacement at a site, the LDI must then be paired with topographic parameters.

To incorporate topographic parameters into their analysis, Zhang et al. (2004) developed a case history database built largely of information previously used in developing the models of Bartlett and Youd (1992a, 1995) and Rauch and Martin (2000). As with prior methods, Zhang et al. (2004) performed a regression on the database to produce a pair of equations, which are presented below.

The model for gently sloping ground (0.2% < S < 3.5%):

$$LD = (S + 0.2) * LDI \tag{2.16}$$

And the model for sites with a free face (4 < L/H < 40):

$$LD = 6 * (L/H)^{-0.8} * LDI \tag{2.17}$$

The equations may also be combined in cases that have free faces bounded by gently sloping ground, and in any case, the parameters are defined as predicted lateral displacement, LD (cm), distance from the toe of a free face, L, height of the free face, H, and ground slope, S (%). When evaluated against their own case history database, equations 2.16 and 2.17 tend to produce predicted displacements ranging from 50% to 200% of the observed displacement, but the authors suggest that further evaluation is necessary before knowing the reliability of the equations (Zhang et al. 2004).

Another semi-empirical method is the probabilistic approach of Faris et al. (2006). The method is fundamentally based on the laboratory and field testing of Wu (2002), which correlated SPT N-values with a parameter called the strain potential index. By evaluating the strain potential index for each corrected SPT blowcount along the depth of a boring, and then summing the resulting values, Faris et al. (2006) developed a parameter called the Displacement Potential Index (*DPI*).

The strain potential index is determined graphically using Figure 2.3, and is limited by the conditions under which Wu (2002) performed cyclic simple shear tests. First, Wu only tested clean sands, which caused overestimates of strain potential in soils with fines. To circumvent this issue, Faris et al. (2006) created an adjustment factor, ΔN_{FC}, for $(N_1)_{60cs}$ based on an assumed relationship between the corrected SPT blow count value and fines content.

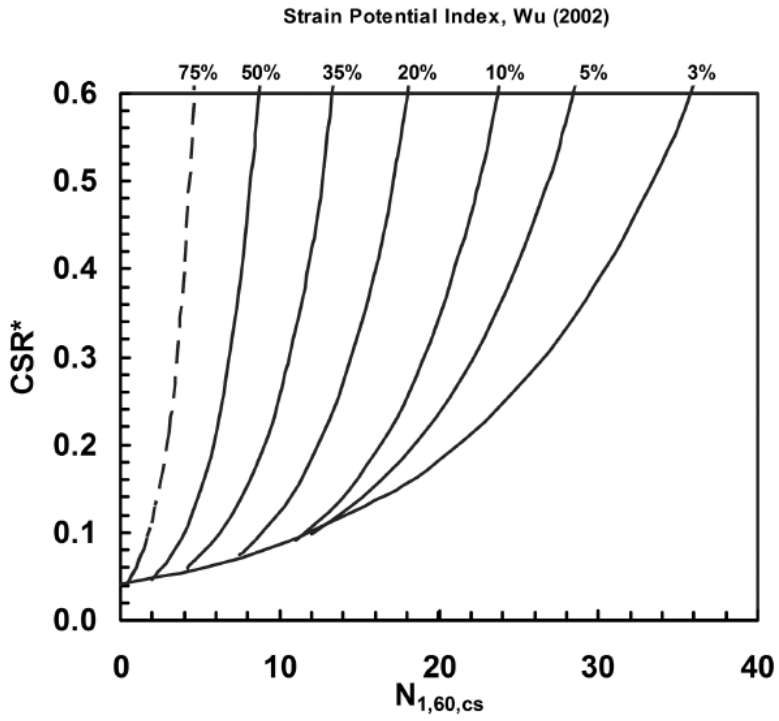

Figure 2.3: Strain potential index curves used for *DPI* analysis (From Faris et al., 2006).

A second limitation in Wu (2002) was that $(N_1)_{60cs}$ and the CSR were only evaluated for shear strain potential indices up to 50%. Faris et al. (2006) determined that, because of the high shear strains experienced during lateral spreading, larger strain potential indices would be necessary. Working from the trend of Wu's plotted curves, the authors extrapolated a new curve for a shear strain potential index of 75%.

In addition to the *DPI*, Faris et al. (2006) also created the variable α to represent the ratio of horizontal driving shear stresses to the effective vertical stress. Since driving shear forces are a result of site topography, α is calculated as either the average ground slope across a displaced block (in percent), or the ratio of free face height to one-quarter the length of the block. In the case that both a free face and ground slope are present, α then becomes the sum of the two values.

In order to create a model to predict lateral spread displacements, Faris et al. (2006) developed a database of lateral spread case histories. Of the initial 45 sites that were compiled, 4 were observed to be the result of slumping and were removed. The probabilistic approach was then implemented by grading the quality of case history data and assigning weights based on the grades. Once the database was complete, an equation incorporating *DPI*, α, and M_w was fit to the data to produce the following equation.

$$H_{max} = \exp(1.0443 \ln DPI_{max} + 0.0046 \ln \propto + 0.0029 M_w) \qquad (2.5)$$

In the equation, H_{max} (m) represents the maximum horizontal displacement and DPI_{max} is the largest value for *DPI* in a sliding mass of soil. M_w is also included, despite

its usage in calculating *CSR* to further account for the increase in duration associated with larger magnitudes.

Conclusion

The preceding sections summarized several empirical and semi-empirical approaches for predicting lateral spread displacements. Many of the methods appear to provide similar results when evaluated against their own case histories, however, none have been verified using data from recent subduction zone earthquakes. Existing case history databases also incorporate limited data from great earthquakes, which is shown in Table 2.4. These limitations, and an understanding of each method's derivation and implementation, are critical background to consider before moving in the following chapters of this report. The summary of variables introduced during this chapter may also be found in Table 2.5, following Table 2.4.

Of the earthquakes listed in Table 2.4, only the 1923 Kanto, Japan earthquake, and the 1964 Alaska earthquake were caused by subduction zone ruptures. An additional problem with both of these subduction datasets is that they both occurred prior to the incorporation of modern seismic instrumentation, requiring that any ground motions used, such as A_{max} in the Rauch and Martin (2000) model, be estimated. Further, other parameters, such as earthquake magnitude or *R*, should be considered to have a lower quality due to the limited understanding of earthquakes at the time of each event. These difficulties mean that there may be less confidence in existing models, and quite possibly, that they may not agree with the data from new case histories compiled using modern measuring techniques.

Table 2.4: Earthquakes considered by empirical lateral spread prediction methods.

Year	Earthquake	M_w	Type	Youd et al. (2002)	Rauch and Martin (2000)	Zhang et al. (2004)	Faris et al. (2006)
1906	San Francisco, California	7.9	Crustal	**X**	**X**	**X**	**X**
1923	Kanto, Japan	7.9	Subduction		**X**	**X**	
1948	Fukui, Japan	7.3	Crustal		**X**	**X**	
1964	Southern Alaska	9.2	Subduction	**X**	**X**	**X**	**X**
1964	Niigata, Japan	7.5	Crustal	**X**	**X**	**X**	**X**
1971	San Fernando, California	6.4	Crustal	**X**	**X**	**X**	**X**
1979	Imperial Valley, California	6.5	Crustal	**X**	**X**	**X**	**X**
1983	Nihonkai-Chubu, Japan	7.7	Crustal	**X**	**X**	**X**	**X**
1983	Borah Peak, Idaho	6.9	Crustal	**X**	**X**		**X**
1987	Superstition Hills, California	6.6	Crustal	**X**	**X**	**X**	**X**
1989	Loma Prieta, California	7	Crustal	**X**	**X**	**X**	**X**
1990	Luzon, Philippines	7.8	Crustal		**X**	**X**	**X**
1991	Telire-Limon, Costa Rica	7.6	Crustal		**X**		
1993	Hokkaido Nansei-oki, Japan	7.7	Crustal		**X**	**X**	**X**
1994	Northridge, California	6.7	Crustal		**X**		**X**
1995	Kobe, Japan	6.8	Crustal	**X**			

Table 2.5: Listing of variables discussed in Chapter 2.

Source	Symbol	Units	Definition
Hamada et al. (1986)	D	m	Predicted lateral spread displacement
	H	m	Thickness of liquefied layer
	Θ	%	Average ground slope across liquefied block
Youd and Perkins (1987), Bartlett and Youd (1992, 1995), Youd et al. (2002), Bardet et al. (2002), Gillins and Bartlett (2014)	M	-	Earthquake moment magnitude
	R	km	Horizontal distance to the nearest seismic energy source or nearest fault rupture
Bartlett and Youd (1992, 1995), Youd et al. (2002), Bardet et al. (2002), Gillins and Bartlett (2014)	D_H	m	Predicted lateral spread displacement
	S	%	Ground slope
	W	%	Free-face ratio
	T_{15}	m	Cumulative thickness of saturated cohesionless sediments with $(N_1)_{60} \leq 15$
Bartlett and Youd (1992, 1995), Youd et al. (2002)	$D50_{15}$	mm	Average mean grain size over T_{15}
	F_{15}	%	Average fines content over F_{15}
Youd et al. (2002), Gillins and Bartlett (2014)	R^*	km	R adjusted for earthquake magnitude
Rauch and Martin (2000)	R_f	km	Distance from site to surface projection of fault rupture or zone of seismic energy release
	A_{max}	g	Peak horizontal acceleration
	T_d	s	Duration of strong earthquake motions > 0.05g
	L_{slide}	m	Maximum horizontal length from head to toe of lateral spread
	S_{top}	%	Average slope across the surface of a lateral spread
	H_{face}	m	Height of free face from toe to crest
	Z_{FSmin}	m	Average depth to minimum factor of safety in potentially liquefiable soil
	Z_{liq}	m	Average depth to top of liquefied soil
	D_G	m	Interim displacement parameter using Geotechnical-EPOLLS
	D_S	m	Interim displacement parameter using Site-EPOLLS
	D_R	m	Interim displacement parameter using Regional-EPOLLS
	Avg_{Horz}	m	Predicted lateral spread displacement (an average across a slide area)
Zhang et al. (2004)	LD	cm	Predicted lateral spread displacement
	L	m	Distance from the toe of a free face
	H	m	Height of the free face
	LDI	cm	Lateral Displacement Index
	Z_{max}	m	Maximum depth below all the potential liquefiable layers with a FS less than 2.0.
	γ_{max}	%	Maximum amplitude of cyclic shear strains
Faris et al. (2006)	H_{max}	m	Predicted lateral spread displacement
	DPI	-	Sum of strain potential indices over the length of a boring
	DPI_{max}	-	Maximum DPI in the vicinity of a displaced block
	α	-	The ratio of horizontal driving shear stresses to the effective vertical stress
Gillins and Bartlett (2014)	x_i	-	Thickness of layers in the site profile that comprise T_{15} with $SI = i$ divided by the total cumulative thickness of T_{15}

Chapter 3: Analysis of Case Histories

Introduction

This chapter details the development of the GELCH database. First, there is a brief overview of the 1964 Great Alaska earthquake, then the chapter provides background on the compilation of new case histories of lateral spreading from 3 great subduction zone earthquakes that have occurred in the past 8 years: Peru 2007, Chile 2010, and Japan 2011. Each new case history is described in its own section, providing background on the site conditions and the seismic event, followed by an explanation of how each variable was estimated for later use in the evaluation of existing empirical or semi-empirical lateral spread displacement models. The following chapter presents the results of that evaluation.

Each of the case histories described in this chapter also appear in the geographic information system (GIS) version of the GELCH database, and may be accessed by visiting the senior author's webpage. Some necessary comments to be made for the three new case histories, are that factors of safety, *FS*, against liquefaction triggering were determined according to procedures of Boulanger and Idriss (2010, 2014), and that geotechnical variables at a lateral spread displacement vector or slide area were interpolated by inverse-distance weighting (IDW) of nearby SPT borehole data. IDW interpolation was chosen because it was the same approach taken by Bartlett and Youd (1992a, 1995) and Youd et al. (2002). The reason for selecting the Boulanger and Idriss (2010, 2014) triggering relationships is that it considers the most up to date case history data.

1964 Great Alaska Earthquake

Introduction to the 1964 Alaska Case Histories

The Great Alaska Earthquake of March 27, 1964, devastated southern Alaska, and played an important role in the shaping of modern geotechnical earthquake engineering. The magnitude 9.2 earthquake destroyed much of Alaska's transportation infrastructure and resulted in, at its time, $311 million in damage (Bartlett and Youd, 1992b). The scale of the event drew significant attention from engineers and scientists, and was relatively well-documented.

The earthquake was the result of the Pacific plate subducting beneath the North American plate along the eastern extent of the Aleutian Subduction Zone in Southeast Alaska. Widespread coseismic ground deformations significantly affected coastlines throughout the region, but little evidence of surface faulting was observed (Plafker, 1969). Aside from these observations, the timing and location of fault rupture is poorly understood due to a lack of strong ground motion recording stations in Alaska, and less maturity in the field of seismology at the time of the earthquake.

Bartlett and Youd (1992b) compiled several lateral spread case histories from data gathered following the 1964 Alaska earthquake. Due to the limited availability of measured lateral spread displacements, Bartlett and Youd's cases included exclusively conditions along the Alaska Railroad where McCulloch and Bonilla (1970) had documented the deformation of bridge abutments toward their respective channels. For each of the bridge sites, Bartlett and Youd further incorporated geotechnical data from numerous sources, and augmented site information with amplitudes and durations of

ground motions estimated from using attenuation models. To fill out the case histories, Bartlett and Youd also did some surveying during the summer of 1989 to obtain topographic data for the bridge sites.

Due to a lack of visible fault ruptures, Bartlett and Youd (1992b) were required to come up with a new method for defining *R* in the Alaska 1964 case histories. Their solution was to define *R* as the horizontal distance to the pivot line, a contour representing zero subsidence or uplift, from the mapped coseismic deformations of Plafker (1969). A sketch of the pivot line used for the 1964 Alaska earthquake, and the associated zero deformation contours can be found in Figure 3.1. This definition of *R* was intended to best represent the distance to the seismic energy source. Such a definition is unique to empirical models for estimating lateral spread displacements.

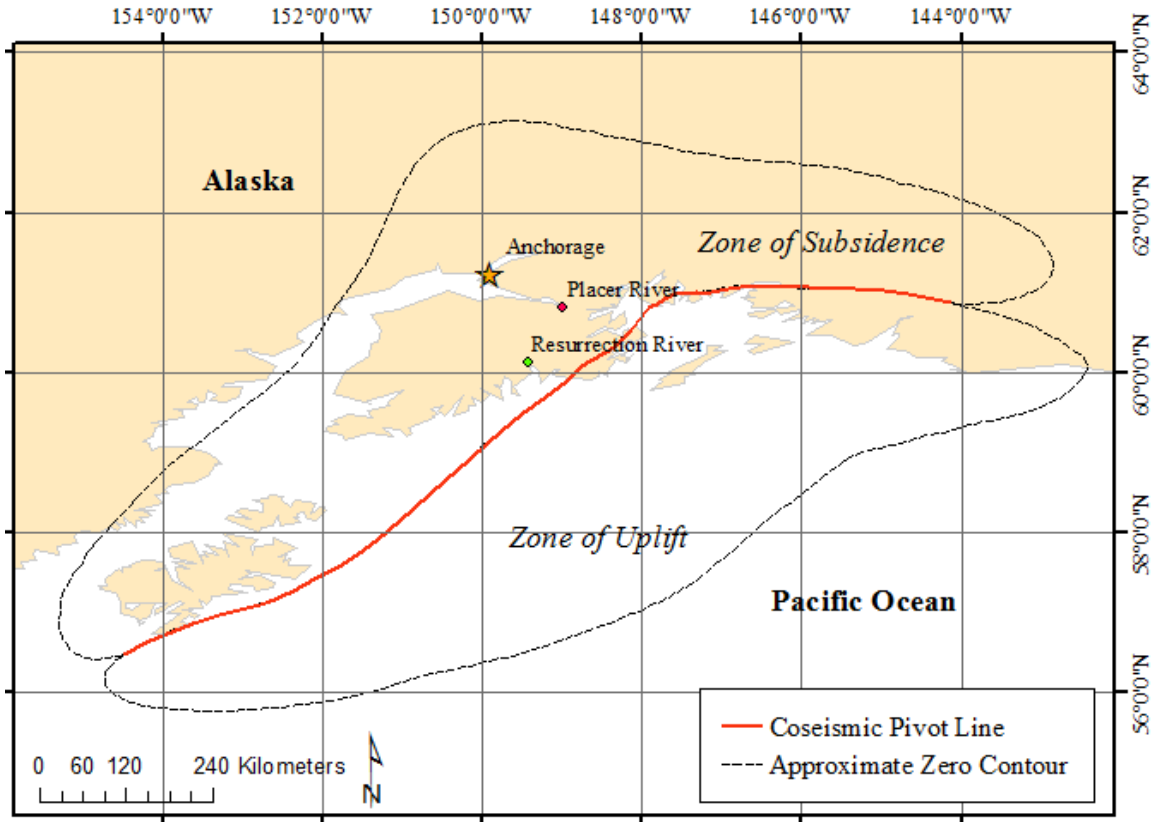

Figure 3.1: Location of the Bartlett and Youd (1992b) pivot line in relation to vertical cosiesmic deformation (Adapted from Plafker, 1969).

The case histories of Bartlett and Youd (1992b) were incorporated into the database used to later develop all their empirical lateral spread models (Bartlett and Youd 1995, Youd et al. 2002). These case histories comprise the only data in the Bartlett and Youd database that involve magnitude 8 or greater earthquakes. Youd et al. (2002) acknowledge that despite the incorporation of 1964 Alaska earthquake case histories, and their model's reasonable accuracy at predicting displacements, the sparsity of data associated with magnitude 8 or greater earthquakes makes application of the their model ill-advised for use with great earthquakes. In other words, due to a lack of case history

data, it is simply unknown if their model performs well for predicting lateral spreading during great subduction zone earthquakes. Additionally, the Alaska earthquake is the only earthquake in the Bartlett and Youd (1992b) database where soils having SPT $(N_1)_{60}$ values greater than 15 were known to have undergone lateral spreading. This exception is important to investigate because it may prompt changes in practice for regions like the Pacific Northwest that are susceptible to subduction zone earthquakes.

Difficulties with the Alaska Data

Several difficulties exist with the Alaska data and should be addressed prior to the development of new case histories. First, as mentioned above, two sites with SPT $(N_1)_{60}$ values typically greater than 15 were affected by lateral spreading; behavior that was not observed in other cases documented by Bartlett and Youd (1992b) in Alaska. Due to their unique behavior, only the two omitted cases will be discussed in this section. These two case histories were not used in their regressions (Bartlett and Youd 1995; Youd et al. 2002), while seven of the other Alaska sites were used. Second, strong ground motion recordings were absent in Alaska during the 1964 earthquake, reducing confidence in estimated ground accelerations and durations of shaking. Finally, the measurements of displacement information from bridge abutments assumes that bridge foundations provided no resistance to the lateral spreading. This final difficulty was well-addressed by Bartlett and Youd (1992b), but will be mentioned here due to its significance to new case histories.

Normalized SPT blowcounts have informally grown to become an index for estimating a number of soil behaviors, and it is currently common practice to assume that

lateral spreading is unlikely to occur in sites having $(N_1)_{60}$ values exceeding 15. The fact that a possible exception to this norm occurred during the Great Alaska earthquake is critical to this research because it hints that a subduction zone earthquake may present conditions that cannot be accounted for by current empirical/semi-empirical lateral spread prediction models. The two lateral spread locations having predominantly high $(N_1)_{60}$ values were at the Resurrection and Placer rivers. At the Resurrection River, similar manifestations of lateral spreading resulted in the compression of three railroad bridges (milepost 3.0, 3.2, and 3.3) as their embankments deformed into the channel. Alternatively, at the Placer River, lateral spreading occurred elsewhere from a bridge, as the river floodplain liquefied beneath the railroad embankment (near Highway Bridge #629). Very little confidence exists in the Placer River data, as it was not used in any model. Alternatively, the adequacy of the Resurrection River data is subjective, as it was omitted from the regressions of Bartlett and Youd (1995), Youd et al. (2002), Zhang et al. (2004) and Faris et al. (2006), but incorporated into that of Rauch and Martin (2000). To better understand the uncertainty of cases from each location, both are detailed individually in the following paragraphs.

The three Resurrection River bridges are located in a similar geologic environment across a 500 m length of the Alaska Railroad. The subsurface information, which was provided by McCulloch and Bonilla (1970), includes one standard-weight, 140 pound SPT boring, and three over-weight 342 pound SPT borings. All four borings were corrected from N to $(N_1)_{60}$, but no specific correction was applied to account for the heavier three borings being over-weight. The different forms of hammer show little agreement at shallow depths (less than 5 m), where, after normalization, the 342 pound

hammer results show the presence of a loose layer that does not appear in those from the 140 pound hammer. A comparison of the borings at the Resurrection River is provided in Figure 3.2. Note that the plotted values for the 342 pound hammer have not been corrected for an irregular sampler diameter, which Bartlett and Youd (1992b) suggest may account for variability between the plotted value and the true $(N_1)_{60}$ of up to 20 percent. It is perhaps most important to note that for the standard 140 pound hammer, all $(N_1)_{60}$ values shown in Figure 3.2a are all greater than 15.

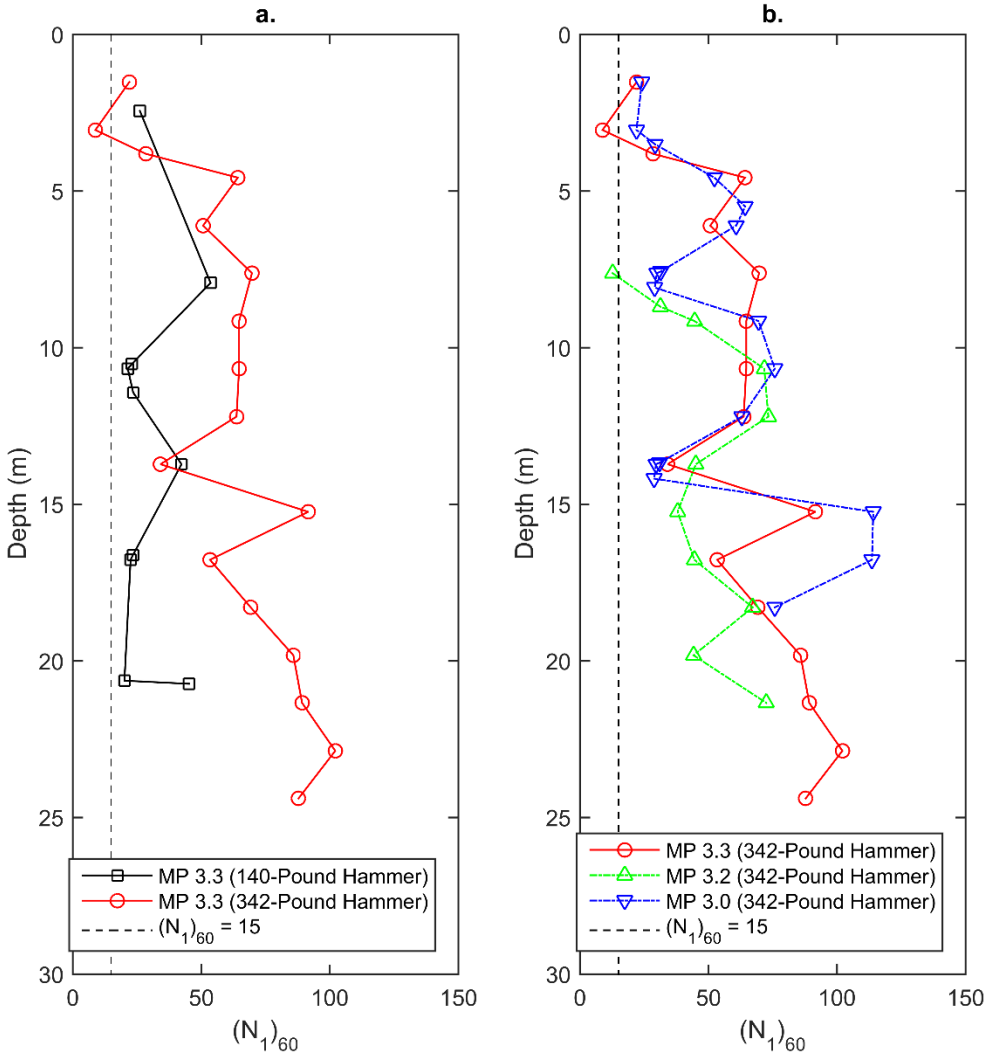

Figure 3.2: Comparison of (a.) penetration tests performed at MP 3.3 and (b.) non-standard penetration tests in the Resurrection River floodplain. Water table is at ground surface.

Other important observations about the Resurrection River bridges are that the underlying soils classify as predominately gravel (Ross et al. 1973), and that the distance to a seismic energy source (R) is 31 km, the shortest of any of the Alaska case histories

(Bartlett and Youd, 1992b). Ross et al. (1973) suggest that the presence of gravels may have artificially increased SPT blow-counts, an assertion which is based on the fact that larger particles are at times difficult to pass through the sampler opening (Fletcher, 1965).

As was the case at the Resurrection River, ground displacement information for the Placer River came from the work of McCulloch and Bonilla (1970). Dissimilarly, the displacements for the Placer River appear to be rough approximates and their specific locations are uncertain. Confidence in subsurface information for the site may also be threatened by the disagreement of SPT results in Figure 3.3, which is based on values found in Bartlett and Youd (1992b). The reliability of available data is further reflected in that it was not used to produce any of the empirical or semi-empirical models published to date.

The second difficulty with the Alaska case histories is that there are no strong ground motion recordings available for the event. As mentioned earlier, Bartlett and Youd (1992b) used the attenuation methods of Joyner and Boore (1988) and Krinitzky and Chang (1988), respectively, to estimate values for PGA and duration. Due to the nature of earthquakes and the availability of data, values resulting from some extent of estimation are almost an expectation, but the values for the Alaska earthquake are an exception because they are not constrained by any known values. The reason why constraining values are important is that recent great earthquakes have demonstrated a wide range of rupture patterns and directions of energy release, which can be discerned from ground motion recordings. The potential for variability will be evident in future sections of this report.

The final difficulty with the Alaska case histories is that the data comes from exclusively railroad bridges built with similar construction practices in comparable geologic environments. By lacking any significant differences, it becomes impossible to identify any biases that might exist due to this combination of conditions. Bartlett and Youd (1992b) acknowledge that this concern can be limited by noting that most of the wooden bridge piles provided little resistance to lateral spreading, by either breaking, or being carried along with the soil. For bridges along the Alaska Railroad, this assumption is reasonable; however, for modern concrete bridges, such an assumption may not be valid as discussed in this report.

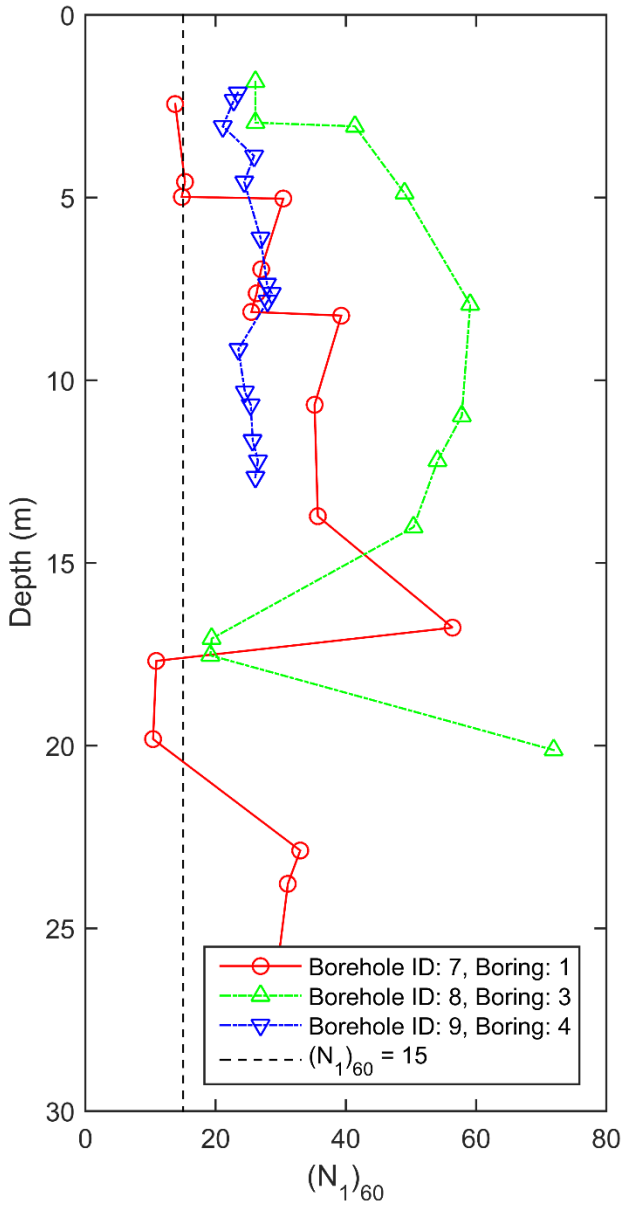

Figure 3.3: Adjusted blow-counts from borings in the vicinity of the Placer River floodplain. Water table is assumed to be at ground surface.

Katori City, Japan

2011 Tohoku Earthquake

The M_w 9.0 Tohoku Earthquake of March 11, 2011, and its associated tsunami presented one of the most severe natural disasters to occur in modern times. Due to the severe effects of the tsunami on critical infrastructure, most notably the Fukushima Daiichi nuclear power plant, and the availability of related media, liquefaction-induced lateral spreading received limited attention following the earthquake. This lack of attention can be attributed in part to the nonviolent nature of lateral spreading, which as mentioned previously, tends to produce costly damage with less risk to human life. Deformation caused by lateral spreading can be seen in Figure 3.4, where the banks of an artificial channel have deformed to damage adjacent roadways and retaining structures.

Figure 3.4: Displacement of channel banks in Katori due to lateral spreading (Ashford et al. 2011).

Most liquefaction associated with the Tohoku earthquake occurred in the recently deposited sediments of the Tone River on Japan's Kanto Plain. Land use in this region ranges from urban to agricultural, and it is topographically dominated by broad floodplains. During the last four centuries, significant anthropogenic reshaping has led to the deposition of alluvial deposits over a more widespread area. The result is that many locations are characterized by loose sediments with standard penetration resistances from N = 7 to 13, often capped by poorly engineered fills with resistances as low as N = 0 to 2. (Pradel et al. 2014).

The tectonic rupture responsible for the Tohoku Earthquake occurred offshore of Japan's east coast, and involved the deformation of an approximately 500 km long interface between the Pacific and Okhotsk Plates (Hayes 2011). The fault plane and slip distribution were developed using standard waveform inversion methods (Hayes 2011, Shao et al. 2011, Wei and Sladen 2011, among others) and, in general, the fault solutions all show the presence of a single strong rupture followed by a smaller, but still noticeable, second rupture having occurred roughly two minutes later. For most of the affected region, the smaller rupture is barely noticeable in ground motion records and lies outside the roughly one-minute of strong shaking experienced in most places (NIED 2011).

Due to its distance from the rupture plane, widespread liquefaction at the Tone River is recognized as being uncharacteristic. From previous discussion, the low standard penetration resistance of the alluvial soils is likely a major contributor to the occurrence of liquefaction, but Pradel et al (2014) also suggest that the river's location on the deep sedimentary basin of the Kanto Plain helped to exaggerate ground motions, which also may have led to an increase in the extent of liquefaction.

The Katori City Site

The city of Katori is located approximately 70 km northeast of Tokyo along lowlands on the lower shores of the Tone River. Much of the city is situated on low-sloping sandy soils that are traversed by numerous irrigation channels. Lateral spreading occurred throughout the city, both near free faces (see Figure 3.4) and on gently sloping terrain. For much of the city, very deep and loose alluvial deposits are covered by up to 5 meters of equally loose reclaimed land (Tsukamoto et al. 2012). Such deposits are

especially prone to severe liquefaction hazard, particularly when considering that the underlying sediments may also amplify ground motions at the site (Koketsu and Kikuchi 2000).

Building the Case History

Displacement measurements were taken from Martin (2014), who used optical image correlation methods on high-resolution pre and post-earthquake satellite imagery to detect the lateral movement of surficial soils. Partially processed results of the Martin analysis were provided by Rathje (2015) as two 32-meter by 32-meter resolution raster images showing the north-south and east-west components of displacement, as displayed in Figure 3.5. The primary difference in processing between the provided data, and that presented by Martin, was erroneous displacements on, or near, major waterways had not yet been filtered out as noise due to the moving water. In other words, a large portion of the displacements that were identified by comparing pre and post-earthquake imagery were not from lateral spreading; rather, they were simply due to river flow.

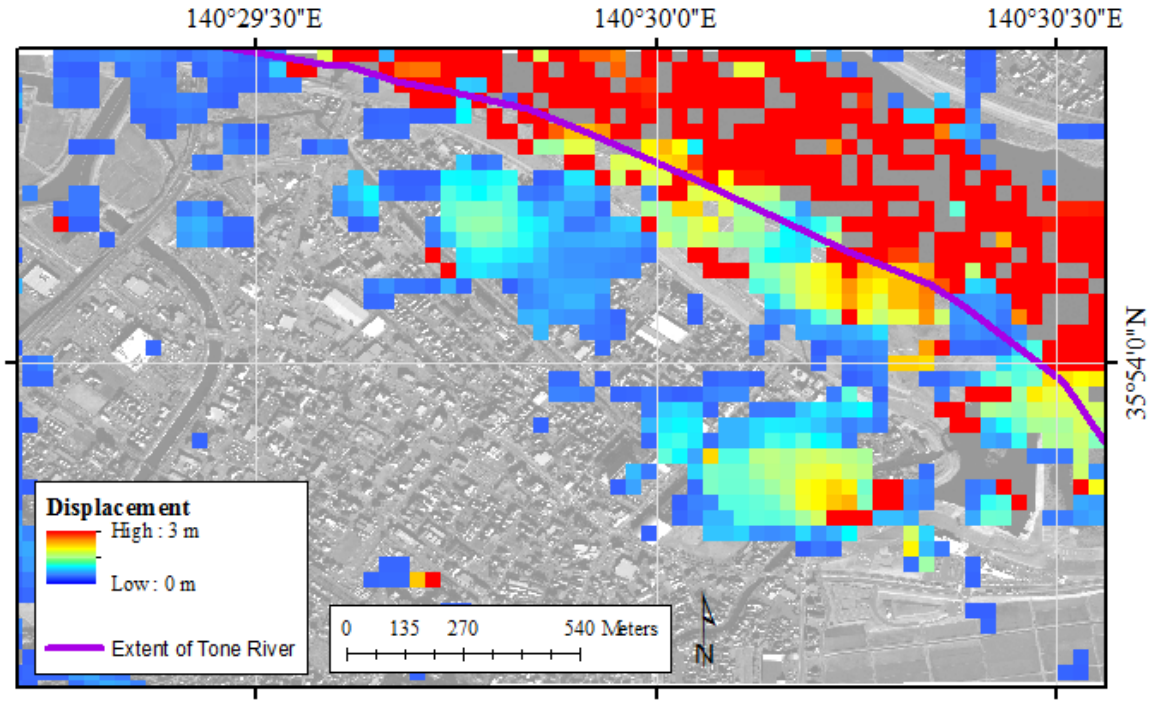

Figure 3.5: Unfiltered ground displacements of Martin (2014) at Katori (Rathje, 2015).

The first step in bringing the provided data to the level presented by Martin was to filter out and remove the displacements associated with the waterways. Using a post-earthquake satellite image, also from Rathje (2015), waterways and complex topographic features (i.e. levees, concrete lined canal walls) were identified and used to remove displacement measurements that likely did not occur. The source of topographic data will be discussed shortly, but for now it is useful to point out that its resolution was too poor to confidently analyze displacements that occurred near the free faces. The displacements that we believe were influenced by free faces were filtered out of this analysis.

To simplify computations and visualization, the remaining north-south and east-west raster cells were then converted into points, and combined to create a grid of points

attributed with the magnitude and azimuth of each 32x32-meter cell. Working with vector data, as opposed to raster data, was important for this step because it allowed for the size and direction of each displacement to be viewed as an arrow symbol in ArcGIS®. It also allowed the collection of additional attributes, such as displacement, slope, and aspect. An example of this benefit can be seen in Figure 3.6.

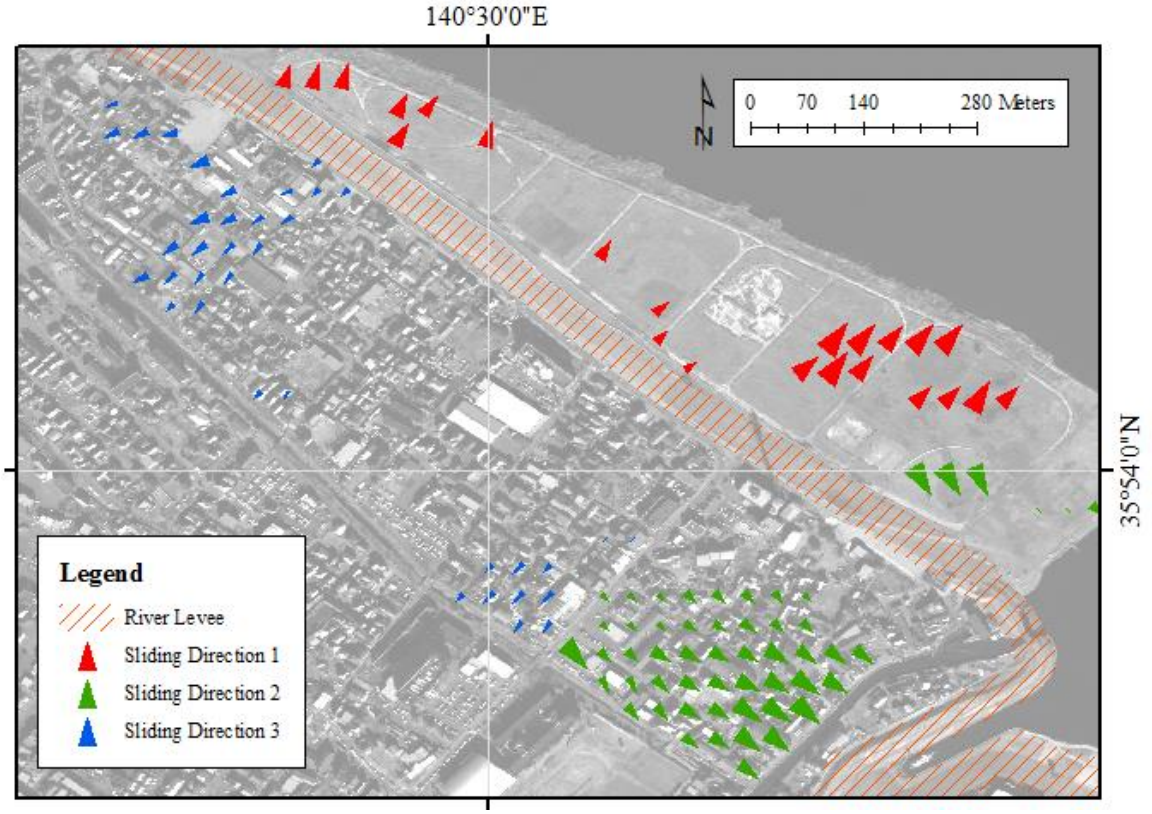

Figure 3.6: Location, relative magnitude and direction of displacements following filtering.

Following the compilation of attributes, the data was analyzed to determine which displacements were adequate for the purposes of this research. The filtering process involved the removal of all displacements of magnitude greater than 3 meters, on slopes

exceeding 6 percent, or with azimuths corresponding with each of the primary compass directions (i.e. 0, 90, 180, and 270 degrees). Filtering values were determined based on visual interpretation of the histograms in Figures 3.7 and 3.8. Figure 3.7 shows that before filtering, an overwhelming majority of displacements have magnitudes less than 3 meters. From the figure, it was assumed that points with higher displacements were the result of noise associated with the optical satellite image correlation. Figure 3.8 shows that before filtering, a significant amount of displacements occurred in exact compass directions (i.e., 0, 90, 180, or 270 degrees). Upon further investigation, these displacements did not correspond with the local orientation of ground slope, and are also assumed to result from the limitations of optical image correlation.

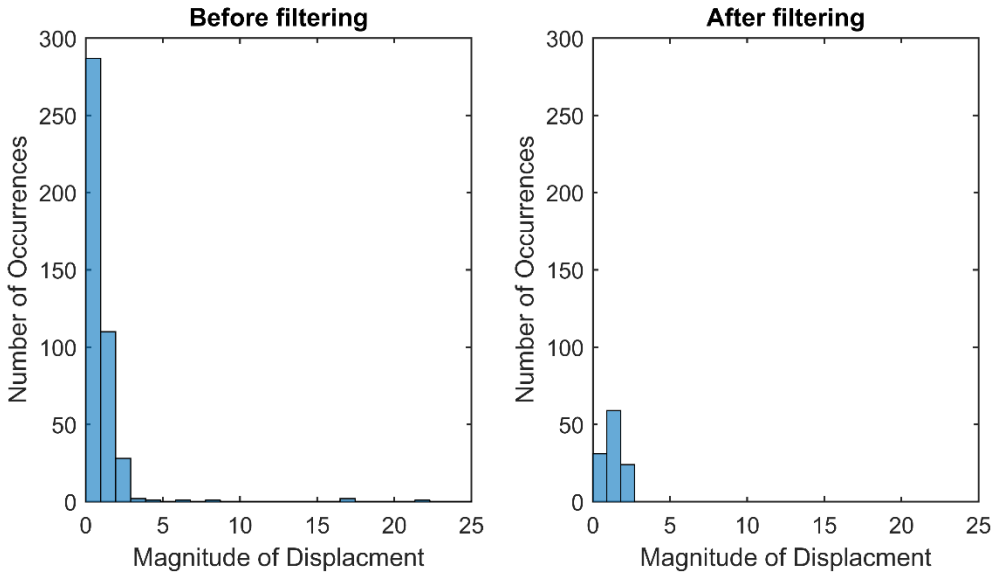

Figure 3.7: Histograms showing the effect of filtering on the number and distribution of displacements.

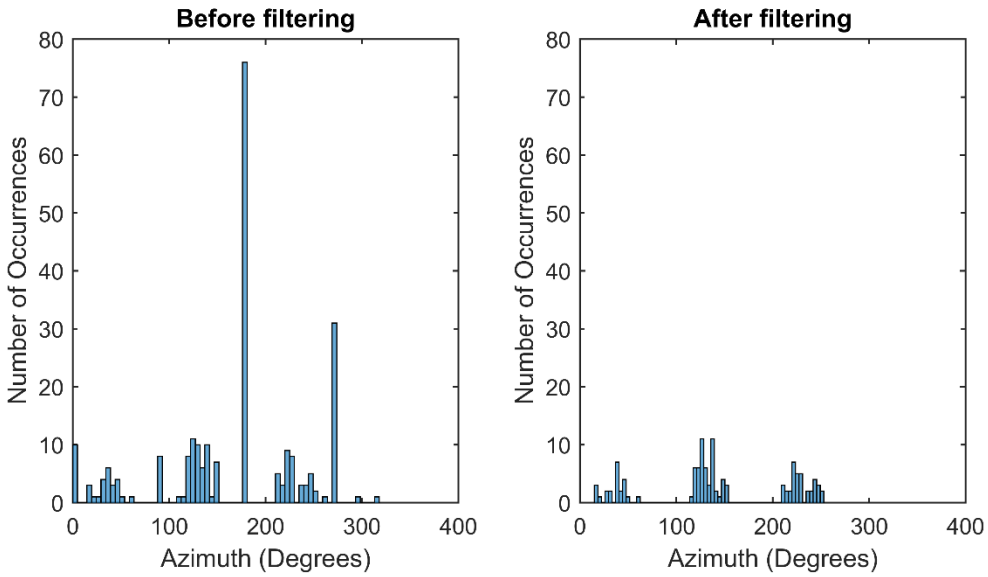

Figure 3.8: Histograms showing the effect of filtering on the value and distribution of displacement azimuths.

The histogram of displacements after filtering in Figure 3.8 shows the existence of three well-defined sliding directions. When mapped in Figure 3.6, these sliding directions show strong spatial correlation, with displacements intuitively occurring in the direction of waterways (downslope), and in some cases constrained free faces.

To better understand which of the remaining displacements were selected for evaluation, it is important to consider local topography. Elevation data for Katori came from a 30-meter by 30-meter Shuttle Radar Topography Mission (SRTM) digital elevation model (DEM). The 30-meter resolution is too coarse to discern slope anywhere other than locations with smooth topographic features, and in addition, the elevations provided near the Tone River are erratic with several large overestimates. To mitigate the weaknesses of the DEM, and as previously mentioned, displacements along the Tone

River were removed from consideration. All other displacements were assumed to be reasonably well described by the DEM.

Earthquake parameters came from several sources. The moment magnitude of 9.0 was selected based on the estimations of the United States Geological Survey (USGS 2015b) and Japan's National Research Institute for Earth Science and Disaster Prevention (NIED 2011). NIED also provided the ground motion data for the seismic station CHB004, which lies within 1 km of the estimated displacements. SPT blowcounts at CHB004 are similar to those near the sites with lateral spread displacements for depths less than 10 m, as can be seen in Figure 3.8, but the ground motion station appears to rest upon denser soils with increasing depth.

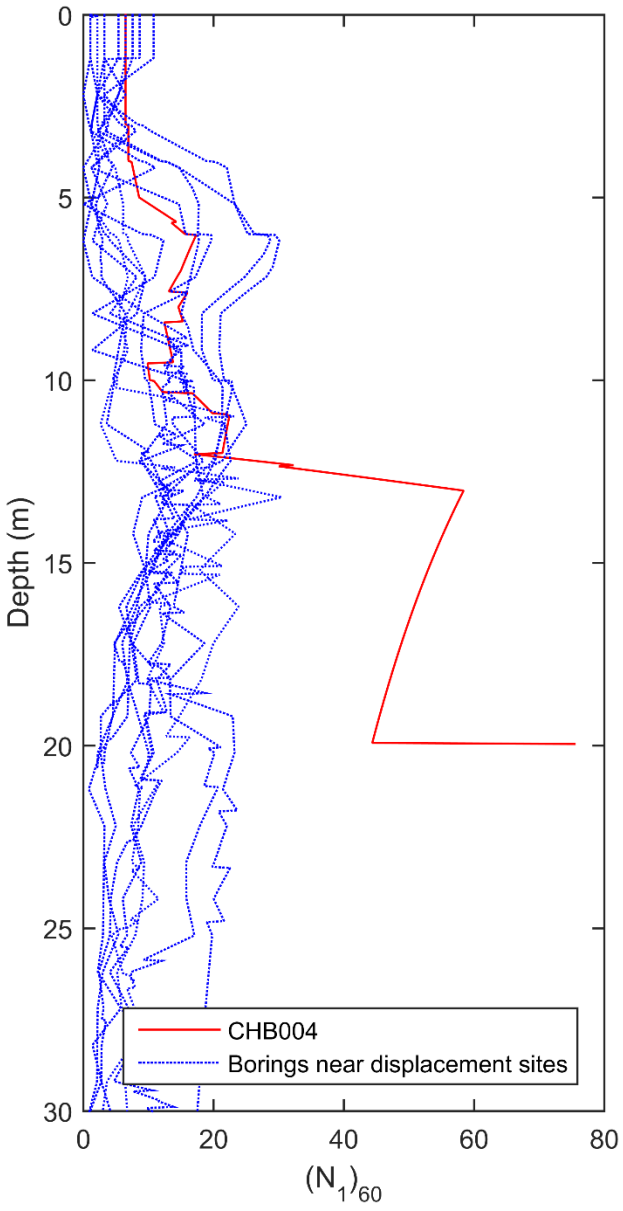

Figure 3.9: Comparison of CHB004 to borings within 150 m of areas with lateral spread displacements.

For the purpose of this analysis, site conditions are close enough to use the ground motions recorded at CHB004 (NIED 2011). The three components of ground motion at CHB004 are presented in Figure 3.10, with the east-west direction having observed the greatest shaking. As seen on the figure, the selected PGA and duration were 0.30g and 68 seconds, respectively. Duration is only used by the Rauch and Martin (2000) lateral spread model, and is computed as a bracketed value at 0.05g, as suggested in their work.

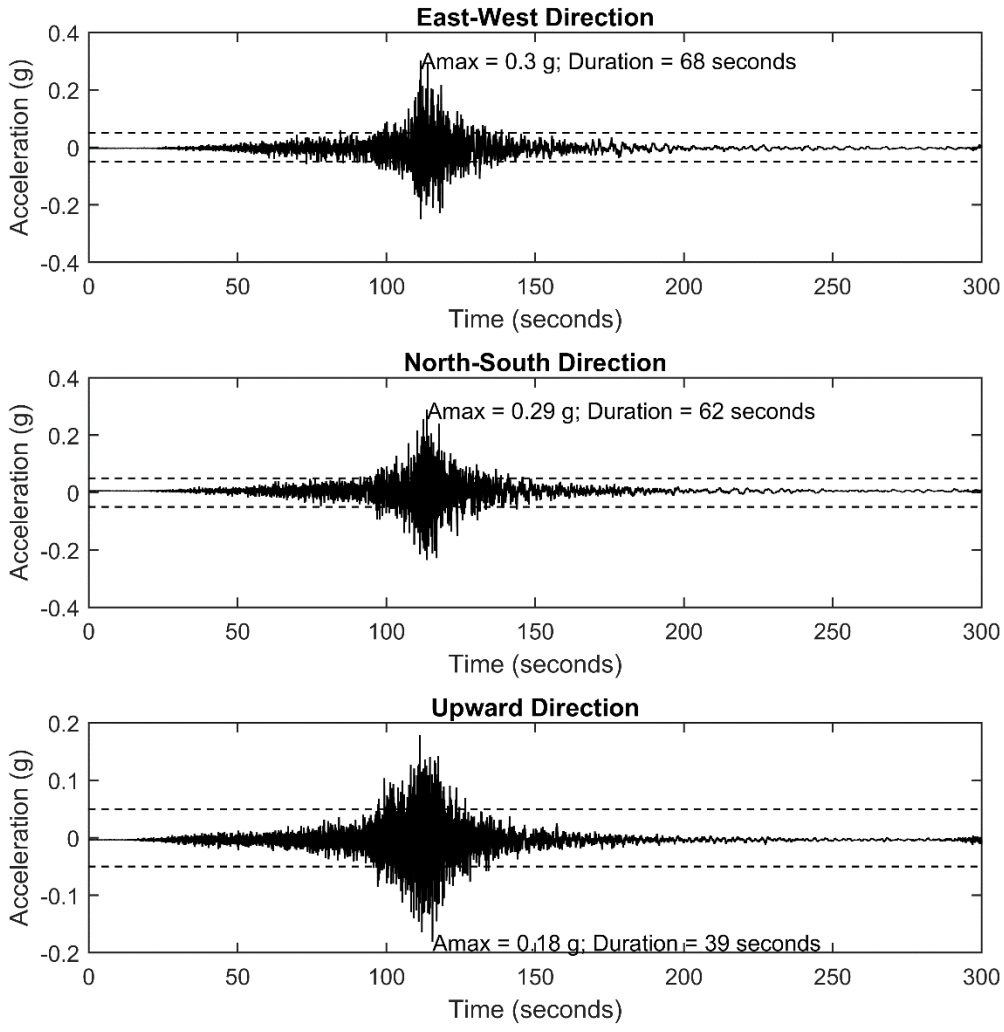

Figure 3.10: Ground motions recorded at CHB004 (K-NET 2011).

The final seismic parameter is the distance to a seismic energy source, *R*. As done by Bartlett and Youd (1992a) with their Alaska case histories, this value was measured as the distance from the lateral spreading case histories in Katori to the nearest point on the coseismic deformation pivot line (i.e. the hinge between subsidence and uplift) taken from the work of Simons et al. (2011). The contours in Figure 3.11 are those presented by Simons et al. (2011), while the pivot line was approximated by the authors of this report. Additional uncertainty exists because the lateral spreading case histories in Katori seem to be west of the southern end of the pivot line where the contours diverge, a complication which will be discussed later in this report.

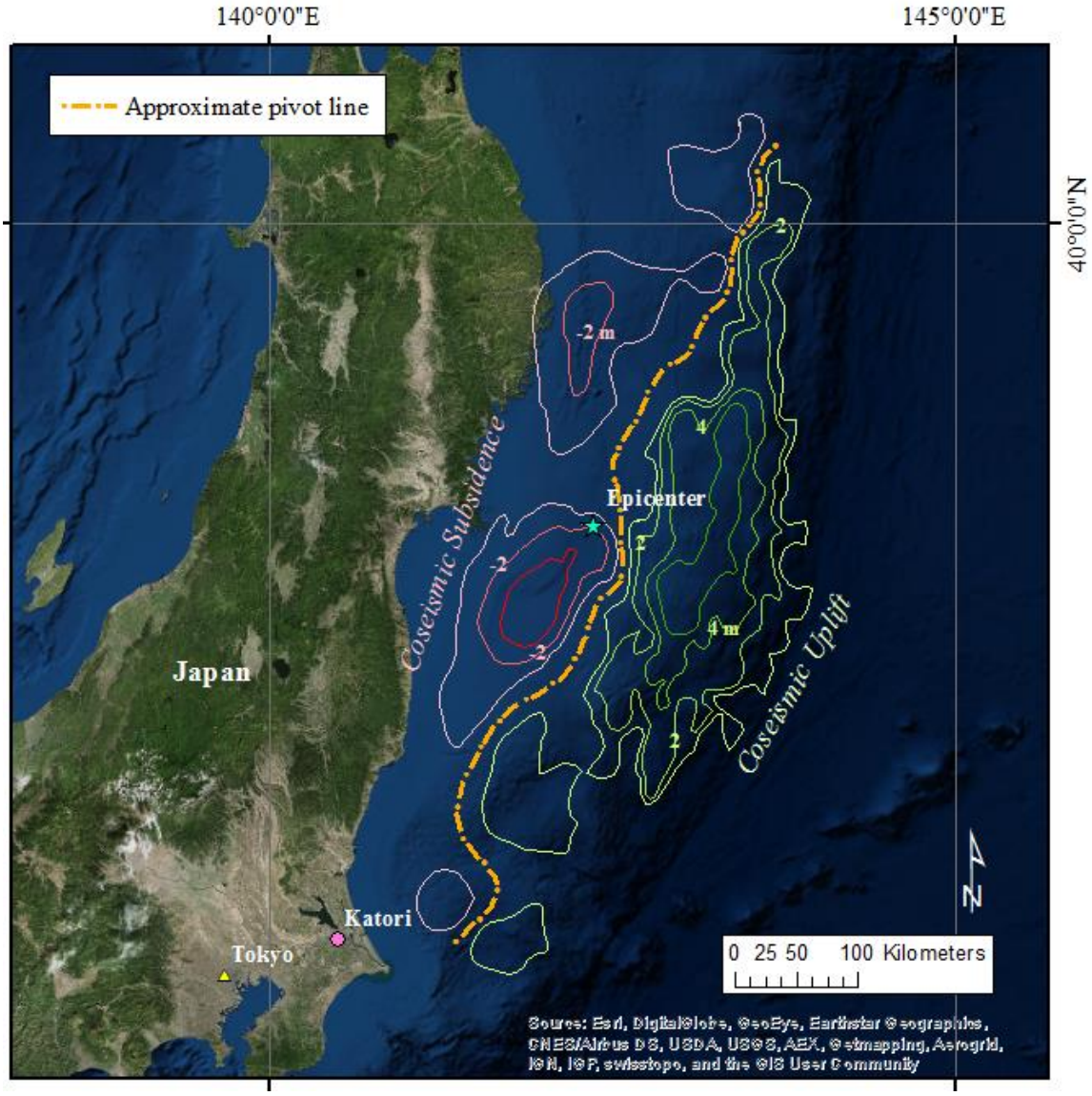

Figure 3.11: Map of vertical coseismic deformation during the Tohoku earthquake (after Simons et al. 2010).

The final data used for the Katori case history concerns geotechnical data. For the most part, this information came from the Chiba Prefecture Geological Information Bank (Chiba 2015). The Information Bank includes a geographic information system with hundreds of geotechnical borings from throughout the prefecture. In Katori, 40+ borings

located within 150 m of a displacement vector were selected and digitized. The borings all provided SPT N-values, soil descriptions, and water table elevations, but do not include laboratory results with soil particle information or unit weights. Because unit weights are necessary at many steps in the analysis, values were estimated using Kulhawy and Mayne (1990) and verified using the local values presented in other sources (NIED 2011, Tsukamoto 2012).

The data compiled for this earthquake was inserted into the empirical models of Rauch and Martin (2000) and Gillins and Bartlett (2014), and the semi-empirical model of Zhang et al. (2004) to estimate lateral spread displacements. Chapter 4 evaluates the performance of these models by comparing the predictions from these models with the observed displacements shown in Figure 3.6.

Canchamana Lateral Spread, Peru

2007 Central Coast of Peru Earthquake

On August 15, 2007 a magnitude 8.0 earthquake struck the Peruvian coast near the cities of Ica and Pisco, killing hundreds of people and destroying more than 50,000 buildings. Strong ground motions were felt for hundreds of kilometers from the rupture, including in the Peruvian capitol of Lima, approximately 150 kilometers away. Most severe damage occurred in those cities closer to the rupture plane, where strong ground shaking exceeded 60 seconds (Marek et al. 2007).

The rupture behind the Central Coast of Peru Earthquake was significant in that it was defined by the rupture of two distinct asperities nearly one-minute apart. The ruptures are noticeable in estimated slip models, Figure 3.12, and in recorded ground

motions, Figure 3.13. Ground motion recordings exist from Ica, located on the modeled fault plane of Ji and Zeng (2007), and Lima further to the north. From these records, the Ica stations observed stronger ground motions during the first rupture; however, the Lima stations experienced greater ground motions following the second rupture.

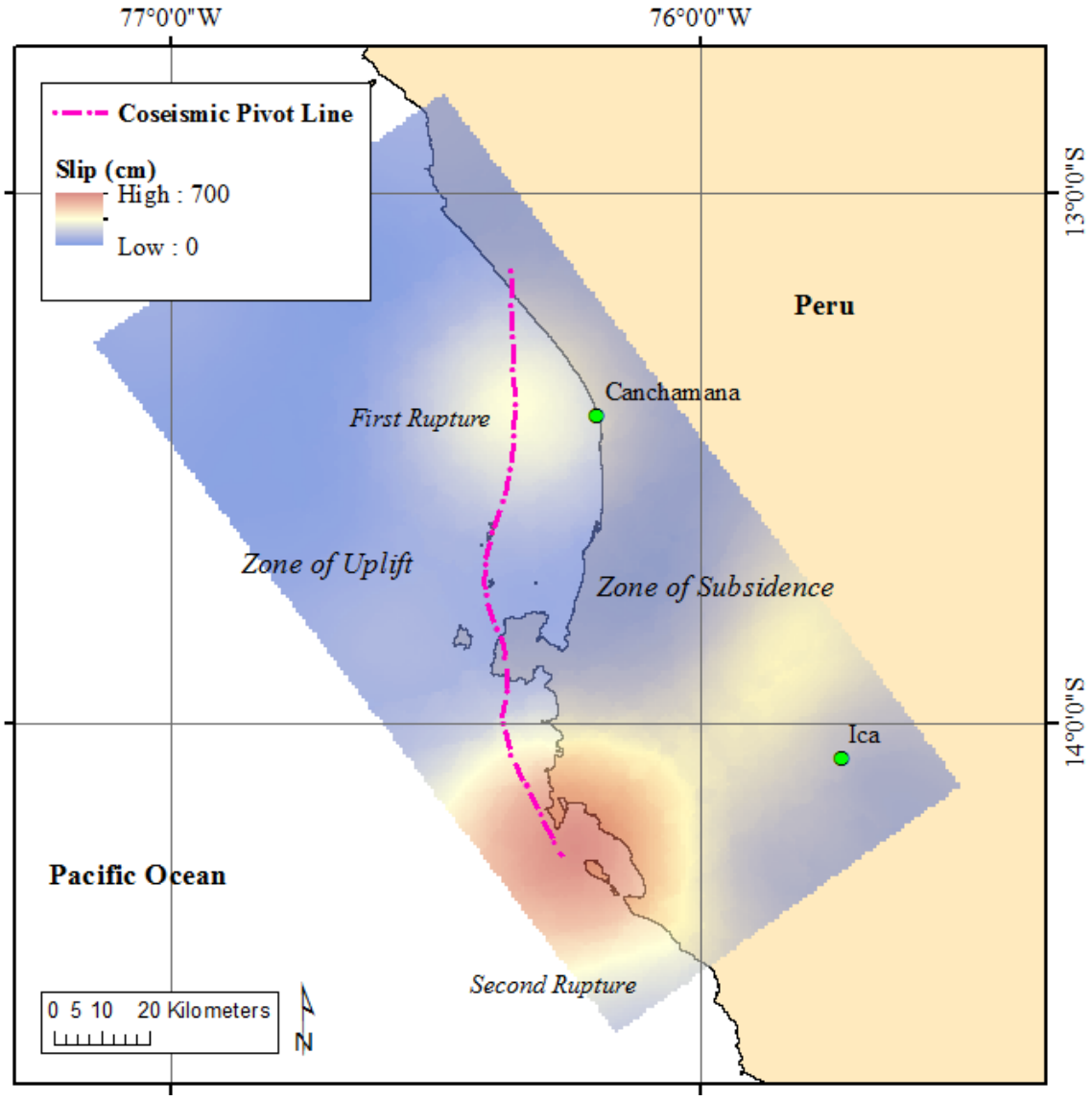

Figure 3.12: Coseismic slip model showing the ruptures of the 2007 Peru earthquake (adapted from Ji and Zeng, 2007).

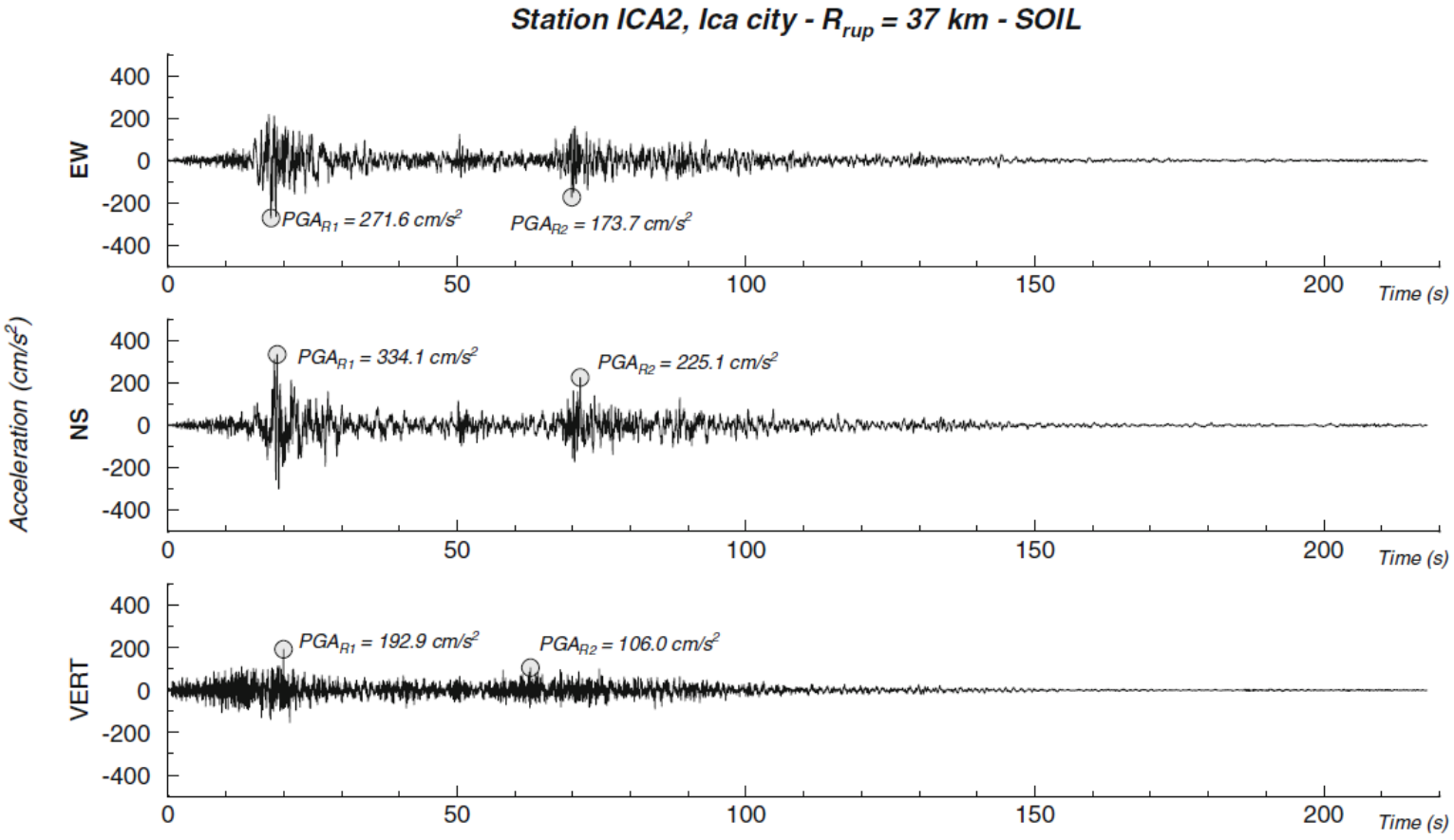

Figure 3.13: Ground motions recorded in Ica, Peru (From Tavera et al. 2009).

Despite being extremely arid, the effected region is characterized by agricultural land in the low sloping floodplains of rivers flowing from the nearby mountains. The result was widespread occurrence of lateral spreading, typically in places where it caused little to no structural damage. Examples of observed liquefaction include ground fractures, sand boils, and collapsed irrigation ditches. Although much of this liquefaction is documented in photographs and writing, very few measurements were made and a limited number of subsurface geotechnical investigations were performed due to economic infeasibility.

The Canchamana Site

An exception to this lack of data comes with the Canchamana lateral spread that occurred along the Peruvian coast near the earthquake's first major rupture. At the Canchamana lateral spread, portions of the marine terrace displaced downslope away from nearby coastal bluffs. This situation, as illustrated in Figure 3.14, was studied extensively by groups that included the Geotechnical Extreme Event Reconnaissance Association (GEER) and the Centro Peruano Japonés de Investigaciones Sísmicas y Mitigación de Desastres (CISMID). Marek et al. (2007) report that, along with remote sensing, the groups performed site investigations using multichannel analysis of shear waves (MASW) and standard penetration testing (SPT).

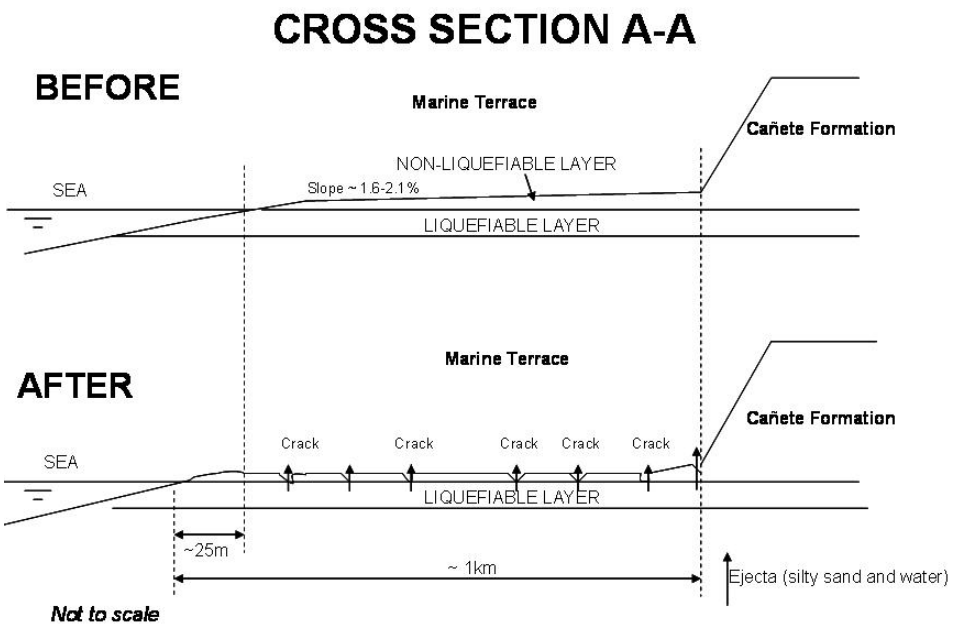

Figure 3.14: Cross section of Canchamana lateral spread (From Marek et al. 2007).

The Canchamana site is located upon a marine terrace composed of geologically recent silts and sands with both alluvial and marine origins. Because of these different forms of deposition, the size and shape of soil particles across the site tends to be highly variable (Marek et al. 2007). At the easternmost extent of observed liquefaction, the marine terrace gives way to the small coastal bluffs of the Cañete formation, labeled in Figure 3.14. Much unlike the soils that liquefied, the Cañete formation is a dense stratum of gravels and cobbles in a matrix of silts and sands with minor lenses of salt (INGEMMET, 2008). The deposition of the Cañete formation occurred more recently than much of the alluvium on the upper marine terrace, and the expectation is that it rests upon silts and sands that did not liquefy due to higher confining pressures. This lack of ground failure is a critical assumption, but reasonable considering that displacements, to be discussed later, were not clearly observed on the formation. By accepting the Cañete

formation as being static during the earthquake, it was then ignored as a driving force behind displacements on the adjacent marine terrace.

Seismically, the Canchamana site lies within the fault plane boundaries estimated by Ji and Zeng (2007). The entire site is additionally located in a region of coseismic subsidence (Sladen 2010).

Building the Case History

Compiling the data necessary to build a case history first required knowing the magnitude of ground displacements for a site. For the Canchamana lateral spread, the displacements were obtained following the preliminary work of Cox et al. (2011), who compared Quickbird Ortho-ready Standard (ORS) satellite imagery from before and after the 2007 event to measure relative ground movement. The results of their analysis were 92 measured displacements, with an average lateral displacement of 1.8 meters, across an approximately six kilometer length of the marine terrace. In addition to the marine terrace displacements, the analysis resulted in 131 measured displacements in other areas, such as on the Cañete formation. The average displacement of these additional points was 0.8 meters, which shows relative movement between the marine soils and the other areas, while also demonstrating significant uncertainty in the measurements. Displacements outside of the marine terrace were considered to be noise resulting from the coarse satellite image resolution, and were removed prior to analysis.

Cox et al. (2011) attributed this difficulty to three sources. First, the satellite imagery's resolution of 0.6 by 0.6 meters paired with inaccuracies inherent to the Quickbird ORS, which is not intended for high accuracy applications. Second, the 90

meter resolution Shuttle Radar Topography Mission (SRTM) and 30 meter resolution Advanced Spaceborne Thermal Emission and Reflection Radiometer (ASTER) digital elevation models (DEM) used to orthorectify the Quickbird ORS imagery may have lacked sufficient detail. This second problem is most pronounced when using the pre-earthquake DEMs to orthorectify the post-earthquake imagery, in absence of a post-earthquake DEM. In the case that earthquake motions and duration are significant enough to produce widespread ground deformations, the earlier DEM may not be an accurate representation of the post-earthquake surface. Third, and lastly, Cox et al. acknowledge that the density of ground control points was greater at on the higher elevation Cañete formation than for the low marine terrace. This inconsistency in control points may have created a bias in the completed orthoimages.

Figure 3.15 illustrates the filtered displacements at the Canchamana lateral spread, with each displacement vector (depicted as stemless arrows) being sized and oriented according to their magnitude and azimuth, respectively. Detail on the filtering is described later in this section.

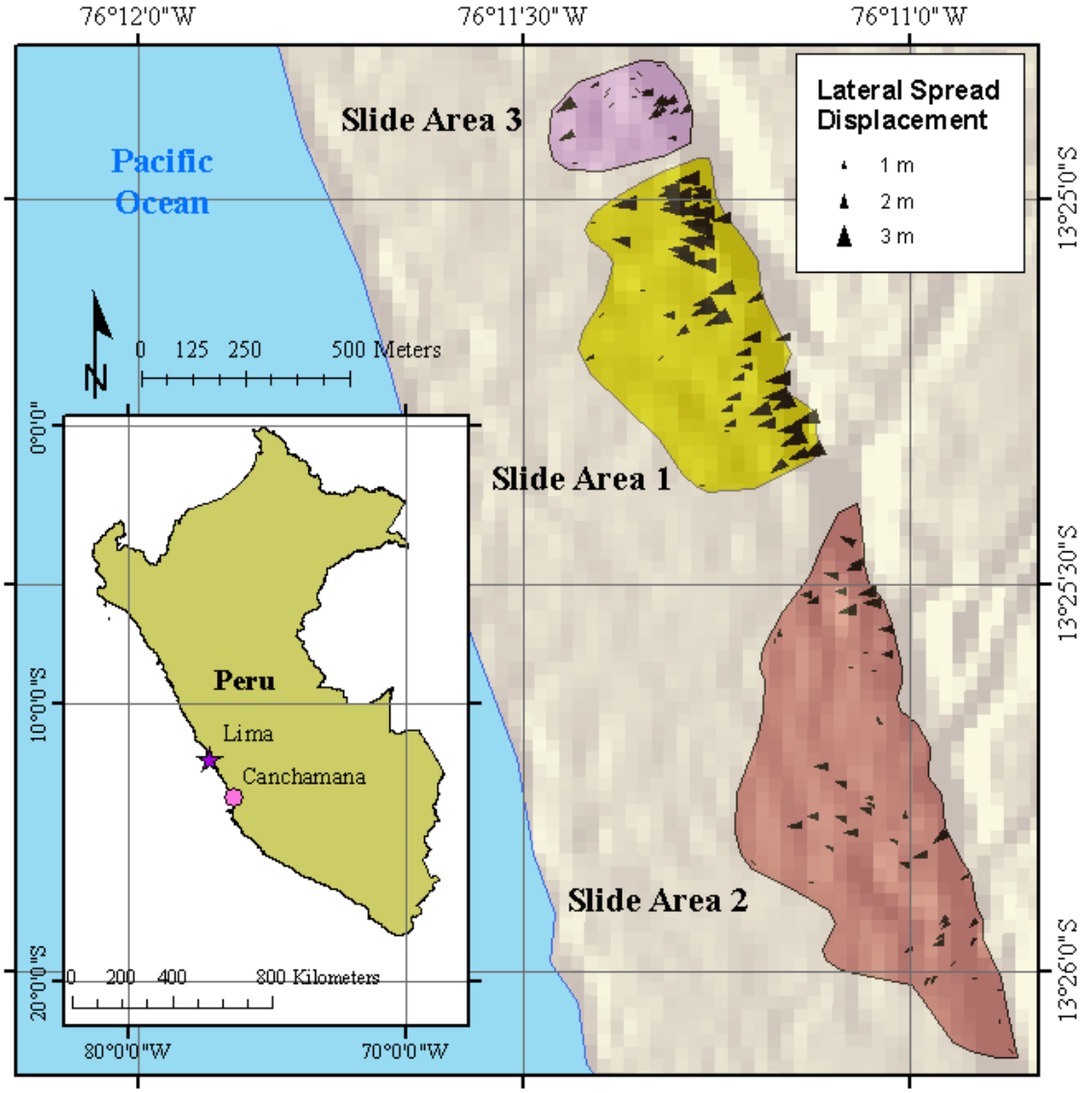

Figure 3.15: Map showing the final analyzed displacements at Canchamana site. Size and orientation of black arrows reflects the magnitude and azimuth of each displacement, respectively.

Other parameters necessary for developing the case history for the Canchamana lateral spread relate to the strength of the earthquake, local topography, and site geotechnical data. In order to assess exiting empirical models, earthquake strength is

demonstrated through moment magnitude, *R*, peak ground acceleration (PGA), and durations of strong ground motions. Earthquake moment magnitude is easily obtained from a variety of sources, and in this case, the 8.0 value came from the USGS Earthquake Hazards Program (EHP). *R* was first measured as the distance from Canchamana to the coseismic deformation pivot line, displayed in Figure 3.12. Because the site is located outside of the western United States or Japan, *R* was then adjusted to R_{eq}, as outlined by Youd et al. (2002). PGA and duration estimates did not exist for the site, and the following paragraphs describe their determination.

In addition to magnitudes, the EHP also provides different ShakeMaps, which include mapped PGA contours. The ShakeMap for the 2007 Peru earthquake may be seen in Figure 3.16. Development of these contours is rather complex, incorporating measured ground motions and site conditions with empirical attenuation models, and a detailed description can be found in Wald et al. (2006). This complexity is evident from the high variability of estimated PGA near the locations of the two rupture asperities. Due to the site's proximity to the ruptures and the inherent uncertainties that come with any ShakeMap, it is difficult to select a PGA value with any confidence. In an attempt to validate the estimates, measured ground motions were considered along with the ShakeMap. To first assess the difference between recorded ground motions and the ShakeMap, PGA values taken from the map at the locations of recording stations were plotted against actual measurements of PGA. The results are displayed in Figure 3.17, and show that the two seismic stations located within the rupture plane (stations ICA 2 and PCN) have both been underestimated by the ShakeMap. In an attempt to overcome

this apparent underestimation of PGA, the highest mapped value of PGA on the ShakeMap at the Canchamana site, 0.35 g, was selected for use in the analysis.

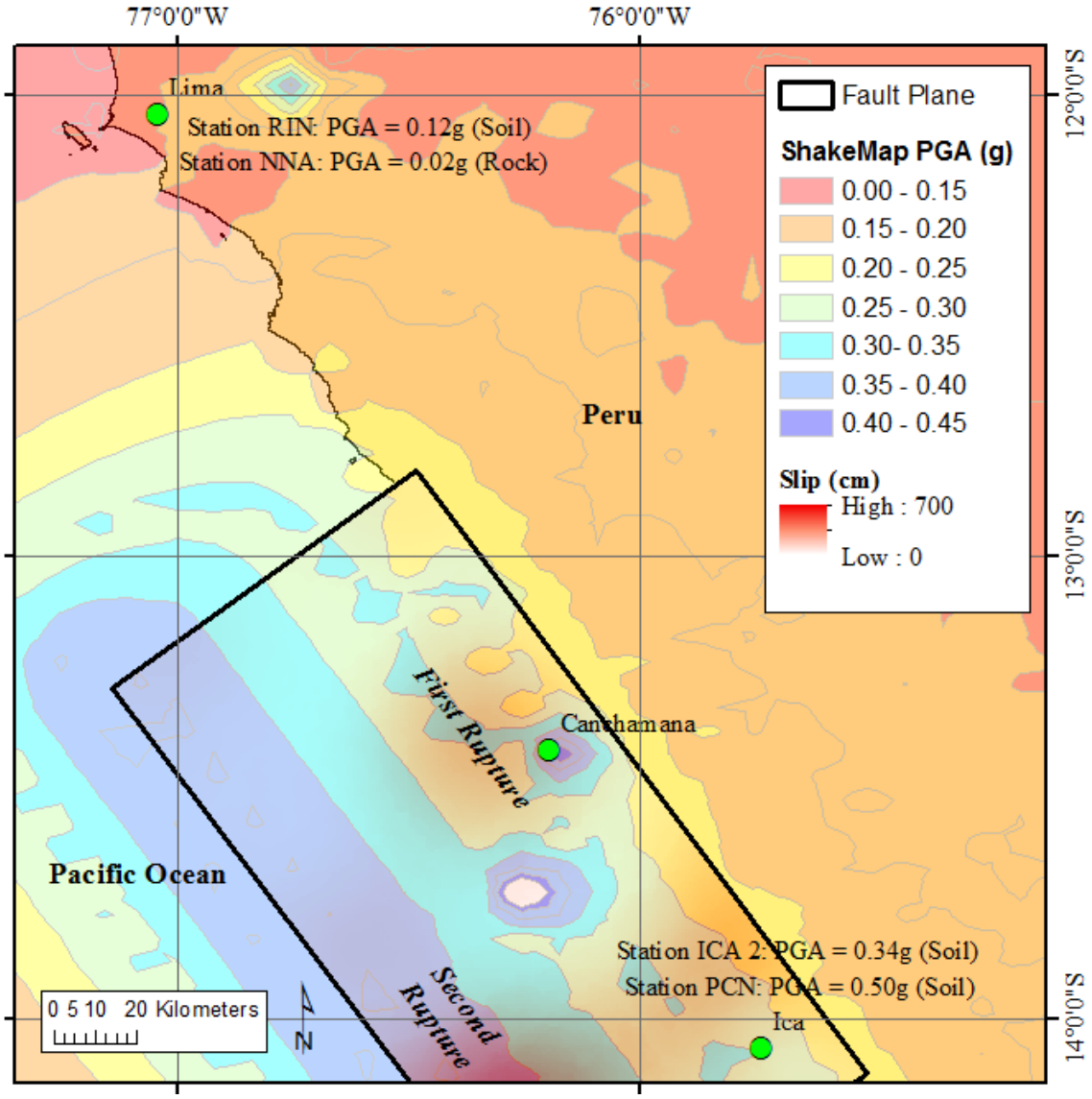

Figure 3.16: Map showing the USGS ShakeMap alongside recorded ground motions in the vicinity of Canchamana.

Prior to moving on, it is necessary to point out that the two seismic stations located within the fault plane (ICA 2 and PCN) are also the only seismic stations that are

not north of the two major ruptures. Some directivity may be apparent, because seismic stations to the north recorded larger PGA values from the second rupture, whereas ICA 2 and PCN recorded larger PGA values during the first rupture. Since the ShakeMap PGA was determined without considering directivity, and Canchamana is generally eastward of the first rupture, it is reasonable for this specific case to assume that the ShakeMap underestimates PGA.

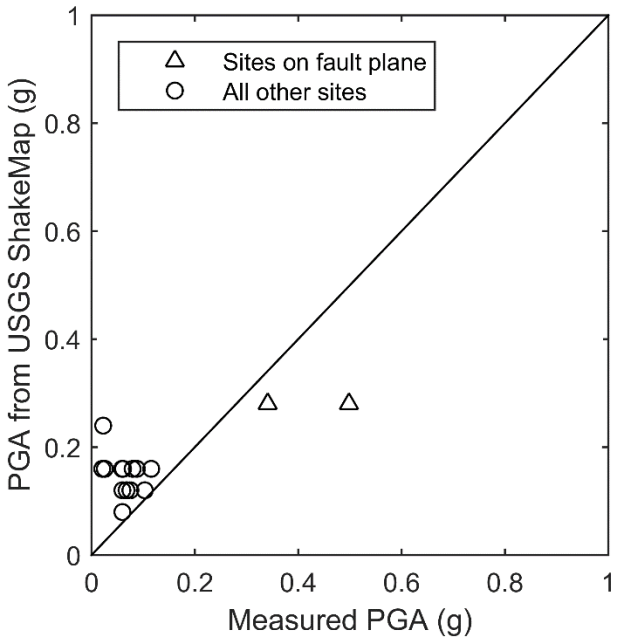

Figure 3.17: Comparison of PGA from Shakemap to PGA observed at ground motion recording stations throughout Chile.

Much like PGA, duration exhibits significant spatial variability. But unlike PGA, duration is not widely reported and is not available in a ShakeMap format. This lack of data leaves only ground motion recordings for selecting the parameter. The nearest ground motion recordings to the Canchamana site came from stations ICA2 and PCN

(Tavera et al., 2009), both located in the city of Ica, more than 75 kilometers away. The station ICA2 is located on soft soils, similar to those of the Canchamana lateral spread, and its PGA value of 0.34 g aligns with assumed PGA for the Canchamana site. Due to this similarity, the ICA2 acceleration time series (Tavera et al., 2009) was used with the definition from Rauch and Martin (2000) to determine a bracketed duration of 100 seconds.

Local topography for the Canchamana site was available with slopes provided by Cox (2014) and a 1-arcsecond by 1-arcsecond SRTM DEM downloaded from the USGS EarthExplorer website. The slopes from Cox (2014) were provided in tabular form with slopes corresponding to each displacement vector. As an attempt at data validation, the SRTM DEM was processed using ArcGIS® to develop an alternative source of slope data. A comparison of slopes from both sources is provided in Figure 3.18. From the figure, it is apparent that the SRTM DEM tends to provide higher estimates for slope. Since the two sources are distinctly different, it became critical to identify the better source. The slopes from Cox (2014) were selected for analysis because the DEM derived slopes appear to be unrealistic when considering photographs taken at the site (Marek et al. 2007, Cox 2014). With the expectation that lateral spreading occurs downslope, the displacements provided by Cox (2014) were then filtered based on the agreement between their direction and provided slope aspects. Figure 3.19 shows the effect of removing displacements whose azimuth was not within 1 dataset standard deviation of the aspect of the slope. Only the remaining displacements were used for analysis.

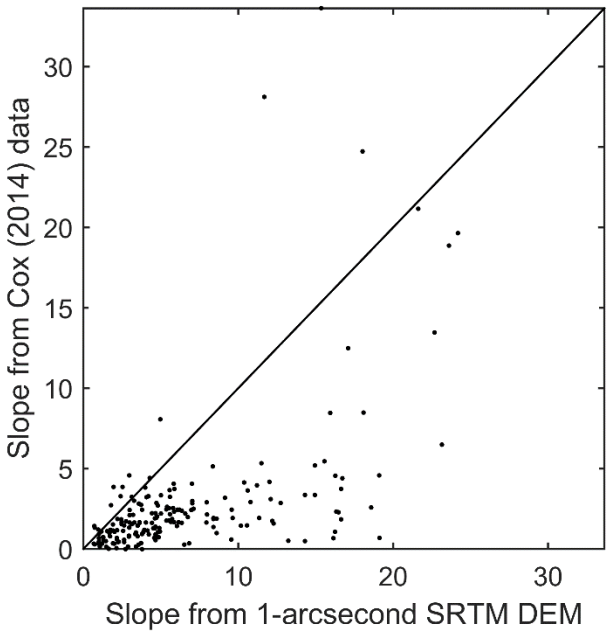

Figure 3.18: Comparison of slope data from Cox (2014) and SRTM DEM.

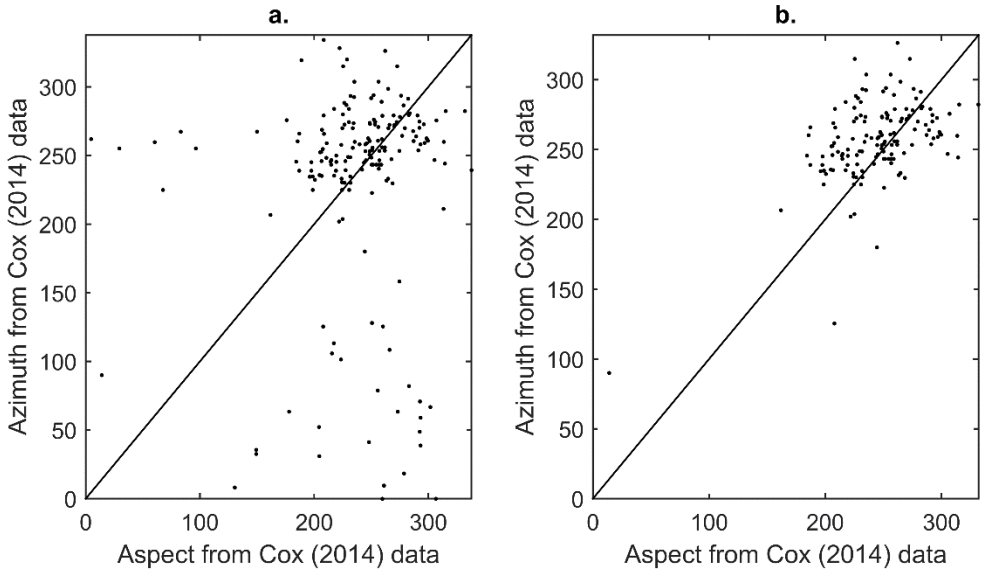

Figure 3.19: Relationship between displacement azimuth and slope aspect at each of the Canchamana displacements, (a) before filtering and (b) after filtering.

As previously mentioned, knowledge of soil conditions at the Canchamana site comes from SPT and MASW tests performed by GEER and CISMID. The SPT data also includes laboratory results for sample soil, which were necessary in obtaining mean grain size and fines content for the different soil layers.

Similar to the Katori case history data, the data compiled for this earthquake was inserted into the empirical models of Rauch and Martin (2000) and Gillins and Bartlett (2014), and the semi-empirical model of Zhang et al. (2004) to estimate lateral spread displacements. Chapter 4 evaluates and discusses the performance of these models.

Mataquito Bridge, Chile

2010 Maule, Chile Earthquake

On February 27, 2010 a magnitude 8.8 earthquake struck the central Chilean coast, causing damage throughout the nation's most populated regions. The most severe damage occurred along the coast, with Chile's second largest city, Concepcion, seeing the destruction of numerous important structures. Significant damage occurred as far away as the capitol of Santiago, hundreds of kilometers away from the earthquake's epicenter. The earthquake is commonly referred to as the Maule Earthquake, after one of the most affected regions.

Like the Central Coast of Peru Earthquake, the Maule Earthquake occurred along a portion of the Nazca Plate subducting beneath the South American continent. As was the case in Peru in 2007, fault rupture models indicated that the earthquake was defined by the rupture of two asperities over a lengthy fault plane (Hayes, 2010; Shao et al. 2010; Sladen, 2010). In this case, the fault plane extended for approximately 500 kilometers

from the coast near Santiago, Chile's most populous city, south to Concepcion. Along the coastline, the majority of damage was caused by tsunami waves, with lateral spreading only being observed at some port facilities. Immediately inland, ground shaking and lateral spreading were far more common, with lateral spreading generally affecting bridges and other structures near waterways. Further inland, places like Santiago were predominately damaged by the strong ground motions, with little lateral spreading having occurred (Bray et al. 2010).

Coseismic deformations associated with the Maule Earthquake were estimated in several models (Hayes, 2010; Sladen, 2010; Lorito et al., 2011; Pulido et al., 2011). The most unique of these models was that of Sladen (2010), who estimated the pivot line between subsidence and uplift to have occurred many kilometers onshore. The other models (Hayes, 2010; Pulido et al., 2011) show that the pivot line is located in the vicinity of the coastline. These remaining models tend to agree with measurements of coastal elevation change made by Farias et al. (2010). According to Pulido et al. (2011), the only significant difference between their estimated deformations and the measured deformations of Farias et al. (2010) occurred near the Arauco Peninsula at the southern end of the rupture plane. The same observations were made by Kelson et al. (2012) regarding the deformations of Lorito et al. (2011). As part of this work, the model of Hayes (2010) was similarly compared to the Farias et al. (2010) deformations. The results of the comparison are shown in Figure 3.20, which demonstrates a similarly weak prediction at the same location.

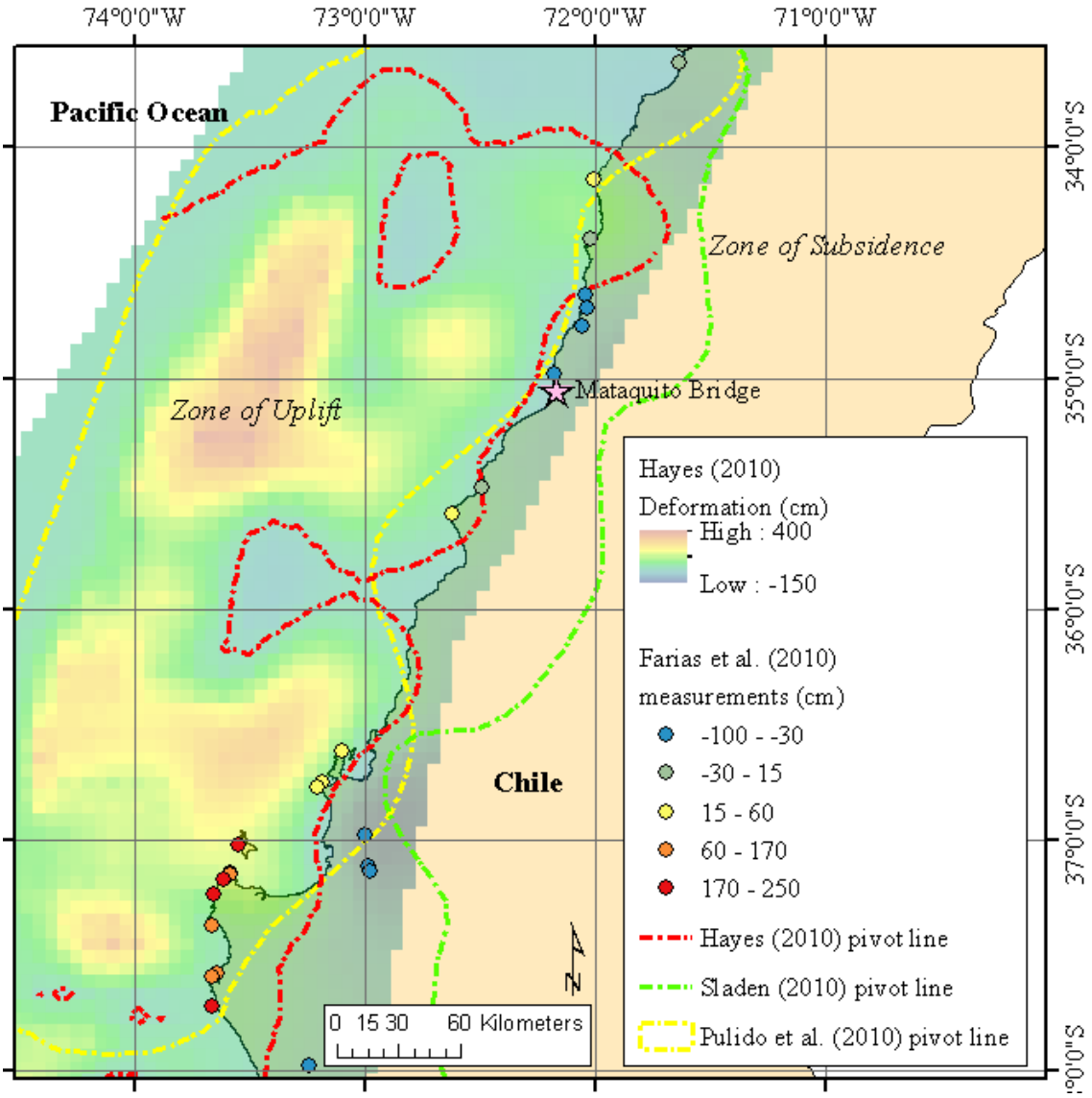

Figure 3.20: Comparison of deformations estimated by Hayes (2010) and measured by Farias et al. (2010), with coseismic pivot lines included for reference.

For this research, poorly understood deformations in the vicinity of the Arauco Peninsula are not an important problem because of the lack of lateral spreading case history data in that region. For more critical locations, such as Concepcion, the models of

Hayes (2010), Lorito et al. (2011), and Pulido et al. (2011) all perform reasonably the same. The difficulty then comes with discriminating between these three models.

The Mataquito Bridge

The Mataquito Bridge is a 280 meter long two-lane highway bridge constructed in 2007 (Petrus 2006; MOP 2007). Geologically, the bridge is situated upon the recent alluvial sediments that comprise the coastal plain formed by the Mataquito River. Due to its modern construction and the occurrence of liquefaction, the bridge has been studied by several researchers in the years since the Maule Earthquake (Bray et al. 2010, Ledezma et al. 2012, Verdugo et al. 2012, McGann and Arduino 2014, Serrano 2014, among others). Available data comes from geotechnical investigations performed in 1996 and 2005, construction drawings from 2006, and limited post-earthquake measurements.

Lateral spreading at the Mataquito Bridge resulted in the formation of numerous cracks along the banks of the Mataquito River. These displacements are shown in Figure 3.21, and appear to be less severe in the immediate vicinity of the bridge. McGann and Arduino (2014) suggest that pile pinning restricted lateral spreading, meaning that the observed displacements may not correctly reflect free lateral movement.

Figure 3.21: Lateral spreading at the northeast abutment of the Mataquito Bridge (From FHWA, 2011).

Building the Case History

Displacement information for the Mataquito Bridge was taken from Bray et al. (2010), who reported that the bridge displaced laterally 180 cm over a distance of roughly 65 m at its northeast abutment. The overall amount of displacement was computed by measuring and summing each individual surficial crack across the 65 m distance, much like many of the measurements used by Bartlett and Youd (1995b). From construction drawings (Serrano 2014), the 65 m is assumed to be a measurement from the base of the abutment to the approximate river shoreline. The bridge span consists of eight 35 m

spans, each supported by reinforced concrete columns resting on 1.5 m diameter piles, which implies that the lateral spread occurred in the presence of at least one pier.

Earthquake strength parameters for the Mataquito Bridge came from several sources. An earthquake moment magnitude of 8.8 was provided by the USGS Earthquake Hazards Program. Ground accelerations were adapted from the University of Chile's National Strong Motion Network (Boroschek et al. 2010), which operates two recording stations within 40 km of the Mataquito site. The first of the two stations is located in Constitucion (station COT), 38 km south of the Mataquito Bridge. Borings from COT show similar soil conditions to those observed in the Mataquito borings (Boroschek et al. 2012), which is reasonable considering Constitucion's geologically comparable location at the mouth of the Maule River (MOP 2012). The second station is located in Hualeñe (station HUA), 35 km east of the Mataquito Bridge. Hualeñe is situated on the Mataquito River floodplain, and despite the presence of larger grained soils, still rests upon similar sediments to the Mataquito Bridge (Boroschek et al. 2012).

Based on the similarities between the Mataquito site and stations COT and HUA, peak ground accelerations and durations from each site were averaged using a first order inverse distance weighting scheme. The resulting PGA and duration were estimated as 0.54 g and 115 seconds, respectively. The provided duration was computed based on 0.05 g bracketed duration, as outlined by Rauch and Martin (2000). After comparison to the PGA provided on the USGS ShakeMap, also 0.54 g, the estimated value of PGA seems appropriate and the expectation is that the estimated duration is similarly reasonable.

The determination of seismic energy source distance had potential to be very complex due to the multitude of available coseismic deformation models. In the

introduction, three models were selected as performing reasonably, and the models of Hayes (2010) and Pulido et al. (2011) are mapped in the accompanying GELCH geodatabase. In the vicinity of the Mataquito Bridge, the pivot lines from each model are located at a nearly identical distance from the bridge. Accordingly, the value for R was selected as 10 km. As was the case with the Canchamana case history, R_{eq} was determined and used in analysis. The pivot line from Sladen (2010) is not used as it does not conform to the other mapped pivot lines, and does not fit well with the measurements of subsidence and uplift near the coast by Farias et al. (2010).

Topographical and subsurface information for the Mataquito Bridge come from the same source, the geotechnical report of Petrus (2006). The report includes scaled cross sections, and the slope was computed as an average over the 65 m displacement length and its corresponding elevation change. Subsurface information comes from six SPT borings, three from 1996 and three from 2005. Numerous water table elevations were recorded during the subsurface investigations and vary by nearly 10 m. None of the recorded water tables were from February, and there is further uncertainty introduced by climatological changes from year to year. A report from the Chilean Ministry of Public Work's Water Division (MOP 2010) shows that river flow rates in the Maule Region were close to average levels during February 2010. The corresponding report for November 2005, when the most recent borings were performed, shows that the river flows were also near average. Using these observations, and the average flows provided for the Mataquito River at Licanten (MOP 2012), the flow rate in February would be approximately 40 percent of that in November. From the Petrus cross sections, and their respective local datum, the estimated river elevation to accompany the reduced flow

would be approximately negative 2 m. This water table elevation was assumed to occur horizontally, and applied to each boring to determine a depth to ground water for the purpose of analysis.

Geotechnical parameters for the Mataquito Bridge came from the six previously mentioned borings. All borings were located within 200 m of the displaced soil, and were therefore incorporated into the analysis, with their respective contributions being determined using inverse distance weighting. The computed parameters associated with the liquefied soil layer seem to correspond well with the liquefiable soils identified by Petrus (2006), adding confidence to the proper selection of values.

Like the previous case histories discussed, the data compiled for this earthquake was inserted into the empirical models of Rauch and Martin and Gillins and Bartlett (2014), and the semi-empirical model of Zhang et al. (2004) to estimate lateral spread displacements. The following chapter discusses results.

Chapter 4: Discussion of Results

Evaluation of Occurrence/Non-occurrence of Lateral Spread from the GELCH Database

As mentioned several times during this report, the possible occurrence of lateral spreading in soils having $(N_1)_{60}$ values greater than 15 during subduction zone earthquakes has been a primary concern of this research. Aside from the two aforementioned cases from Alaska in 1964, all of the SPT borings included in the GELCH database have exhibited at least one layer (and at times a large number of layers)

of liquefiable soils having an $(N_1)_{60}$ value less than 15. To better illustrate this trend, Figure 4.1 compares profiles of $(N_1)_{60}$ with depth for the three new earthquakes incorporated into GELCH Database. This observation is still not conclusive, considering the limited amount of data and the margin of error associated with SPT results, but for now, the results seem to support that assertion that soils having $(N_1)_{60}$ greater than 15 tend not to undergo lateral spreading. It remains unclear why the two sites in Alaska underwent lateral spreading despite having corrected blow counts much greater than 15, but it is possible that since these sites predominantly consisted of gravels, that the larger particles may have stuck to the sampler opening impeding progress and thereby inflated the $(N1)60$ measurements. Much more case history data and future work is needed to determine if lateral spreading can occur with moderately dense soils (i.e., where $(N_1)_{60}$ equals 15 to 30) during subduction zone earthquakes. For now, our only conclusion is that it appears that lateral spreading at sites with moderately dense soils is less common.

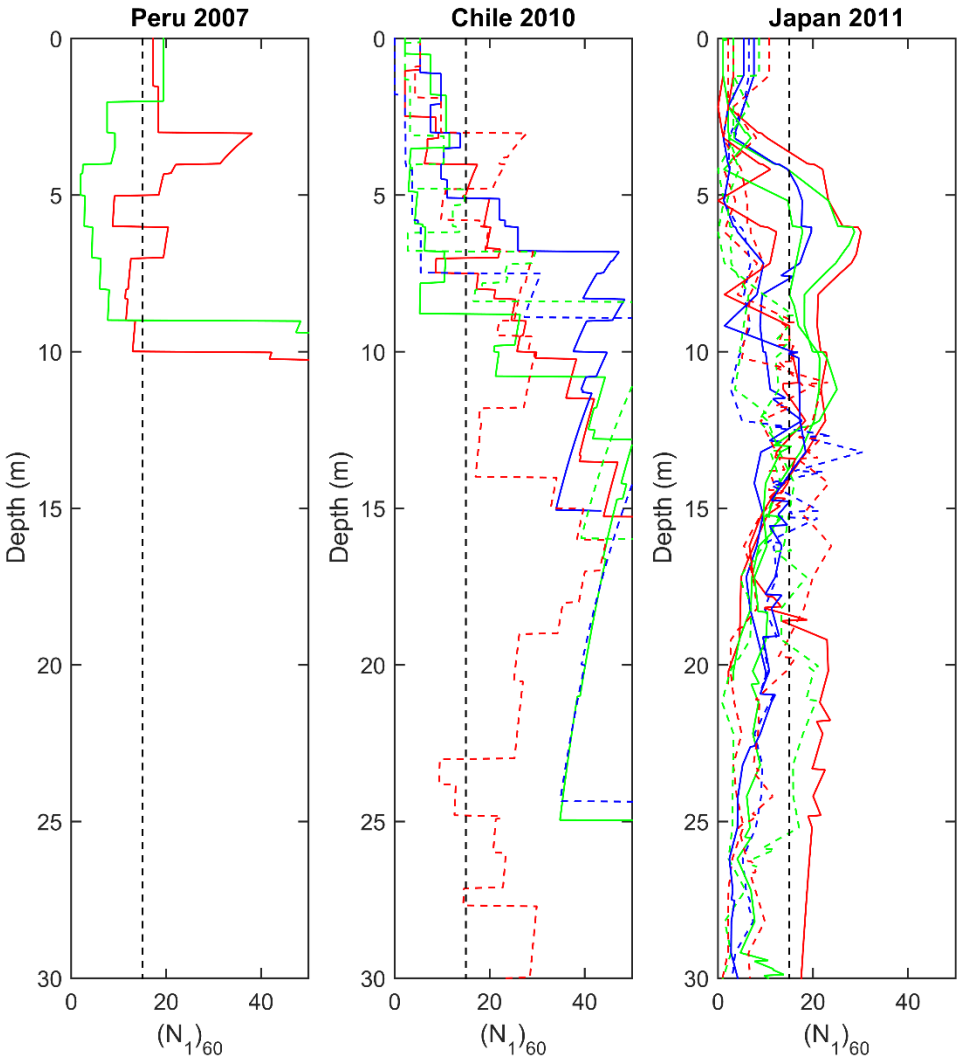

Figure 4.1: Plot showing borings within 200 meters of a displacement in the GELCH Database. The dashed line indicates an $(N_1)_{60}$ of 15, and the groundwater table lies within the upper 5 meters of all profiles.

Assessment of the Rauch and Martin (2000), Youd et al. (2002), Zhang et al. (2004) and Gillins and Bartlett (2014) Empirical Models Using the GELCH Database

Comparison of Predictions from Youd et al. (2002) and Gillins and Bartlett (2014)

Because it is the only case history with laboratory test results to supplement boring logs, Canchamana is the only case history with directly available fines and grain size data. For this reason, it is also the only case history that could be used to evaluate the empirical model of Youd et al. (2002). This shortcoming is not relatively insignificant, as Gillins and Bartlett (2014) found that grain size and distribution is rarely reported on borehole logs. For this reason, they developed a new model that uses soil description in lieu of fines content and mean grain size variables. Gillins and Bartlett (2014) argued that their model should predict lateral spread displacements that are somewhat similar to the Youd et al. (2002) empirical model, because both models are based on an identical case history database and both have similar standard deviations. The first step of our analysis includes the comparison of these two models for the Canchamana data. Observed versus predicted displacements are presented in Figure 4.2.

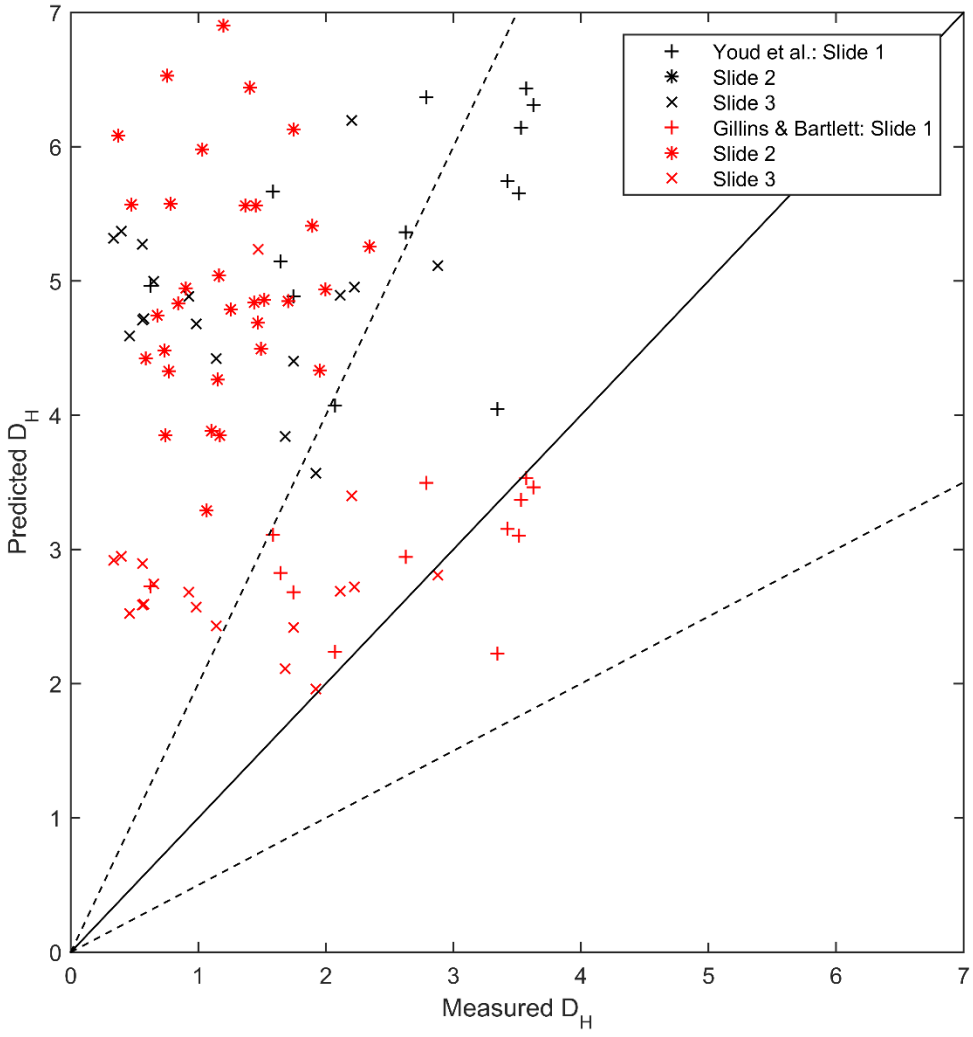

Figure 4.2: Comparison of the performance of the Gillins and Bartlett (2014) and Youd et al. (2002) equations for the Canchamana case history.

Aside from comparing the Youd et al. (2002) and Gillins and Bartlett (2014) equations, this research also proposed the evaluation of alternative methods, including those of Rauch and Martin (2000) and Zhang et al. (2004). The following sections will present the results of our analysis and discuss the performance of the methods for each

case history. For consistency, for each case history discussed below, predictions of lateral spread displacement are made with the same 3 models: Gillins and Bartlett (2014), Rauch and Martin (2000), and Zhang et al. (2004).

Canchamana, Peru

Figure 4.3 compares the results of our analysis to the displacements measured at the Canchamana site. Markers occurring on the solid black line represent perfect predictions, and the two dashed lines bound markers within a factor of 2 of being perfect predictions. The figure will be discussed in detail in the following paragraphs.

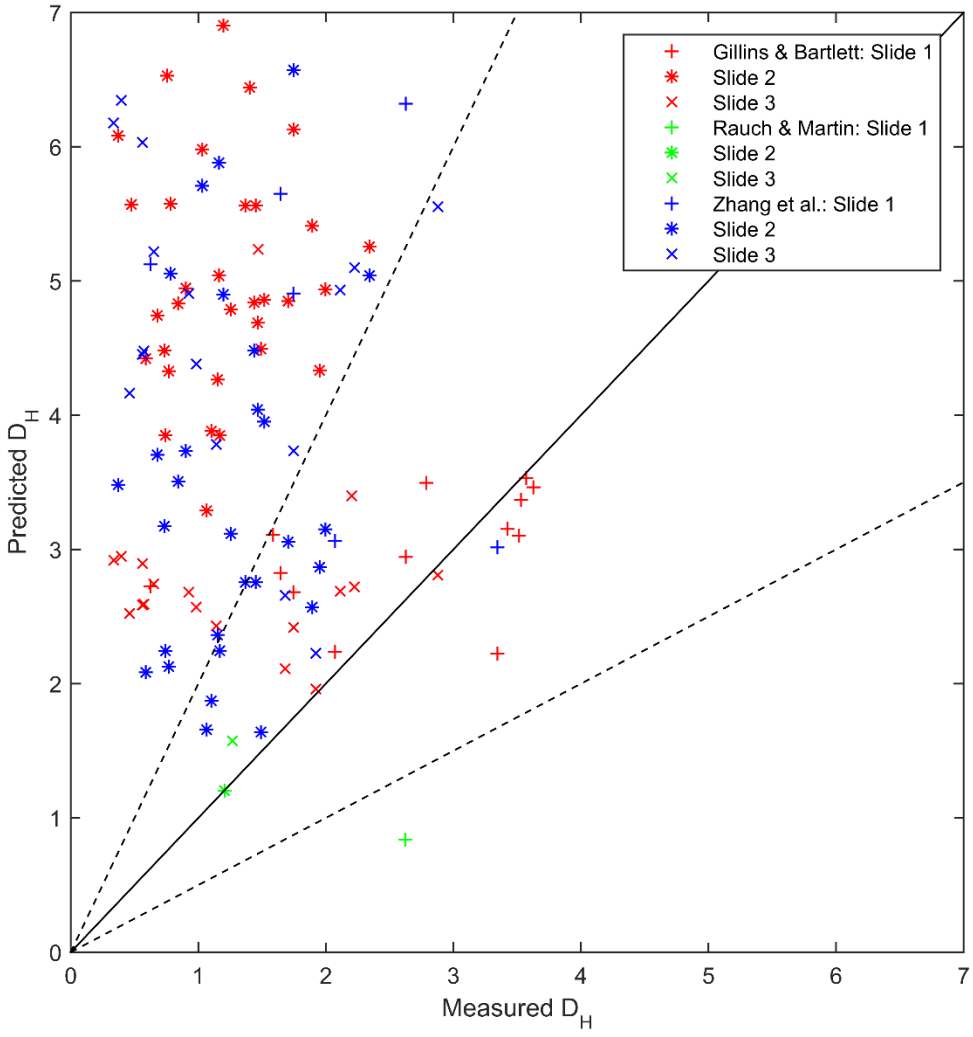

Figure 4.3: Comparison of predicted lateral spread displacements to those observed at the Canchamana site.

Gillins and Bartlett (2014)

From a first glance, the Gillins and Bartlett results presented in Figure 4.3 tend to overestimate lateral spread displacements at Canchamana. Moving forward, this report will attempt to explain what aspect of the equations could have led to the overestimates,

and it is important to briefly reintroduce the uncertainty associated with the displacement information. Recall from chapter 3 that the results obtained from Cox (2014) were developed with the intention of being preliminary results using less than desirable satellite image resolution, and that displacements were erratic in magnitude and location. The filtering performed as part of this research was able to identify clear trends of displacement direction, but the provided displacement magnitudes may be biased, even with the possibility of location correctly identified.

A possible bias in the displacement magnitudes may be evident with over predictions generally being greater for smaller observed displacements, particularly those in slide area 2 (see Figure 3.15). If all displacement magnitudes were incorrect by the same distance, the error would be proportionally larger for the small displacements, and would therefore be more noticeable. The difficulty with this explanation though, lies in the reasonable predictions of Rauch and Martin (2000), which do not appear to suffer, even for slide area 2.

Referring back to the problem statement of the introduction to this report, the failure to incorporate the amplitude and duration of ground motions was considered to be a critical shortcoming for several of the empirical equations. By using earthquake magnitude and the distance, *R*, as a proxy for both ground motion parameters, there is an assumed direct relationship using attenuation models. The 2007 Peru earthquake may be proof to the weakness of this relationship. The ground motions from Ica in Figure 3.13 show that an extended duration of shaking was the result of having ground accelerations that almost appear as two smaller earthquakes occurring in series. For many purposes, the moment magnitude is a strong reflection of the energy released by an earthquake, but that

is only if the rate of energy release is similar in all earthquakes considered. A further difficulty is that the magnitude does not account for the timing of each distinct rupture, or the directivity of those ruptures, in a great magnitude earthquake (i.e. time between the peaks in Figure 3.13). As mentioned in Chapter 3, from Ica to Lima, the rupture responsible for the highest observed ground motions was variable.

The difficulty of rupture timing is particularly important based on the overestimated results, and that is because of its influence on the occurrence of liquefaction. From the Ica ground motions, it is assumed that the first rupture was felt more strongly at Canchamana than the second. From this observation, it is possible liquefaction was initiated during the first rupture and then the lateral spreading occurred. Using the moment rate function of Hayes (2007), displayed in figure 4.4, the magnitude of the earthquake was re-computed to account for only the energy released by the first rupture. A new magnitude of 7.7 was calculated and run in an identical analysis as before. Results of this second analysis are displayed in Figure 4.5, and show improved predictions from the Gillins and Bartlett (2014) equations. Predictions from the other two models hardly changed.

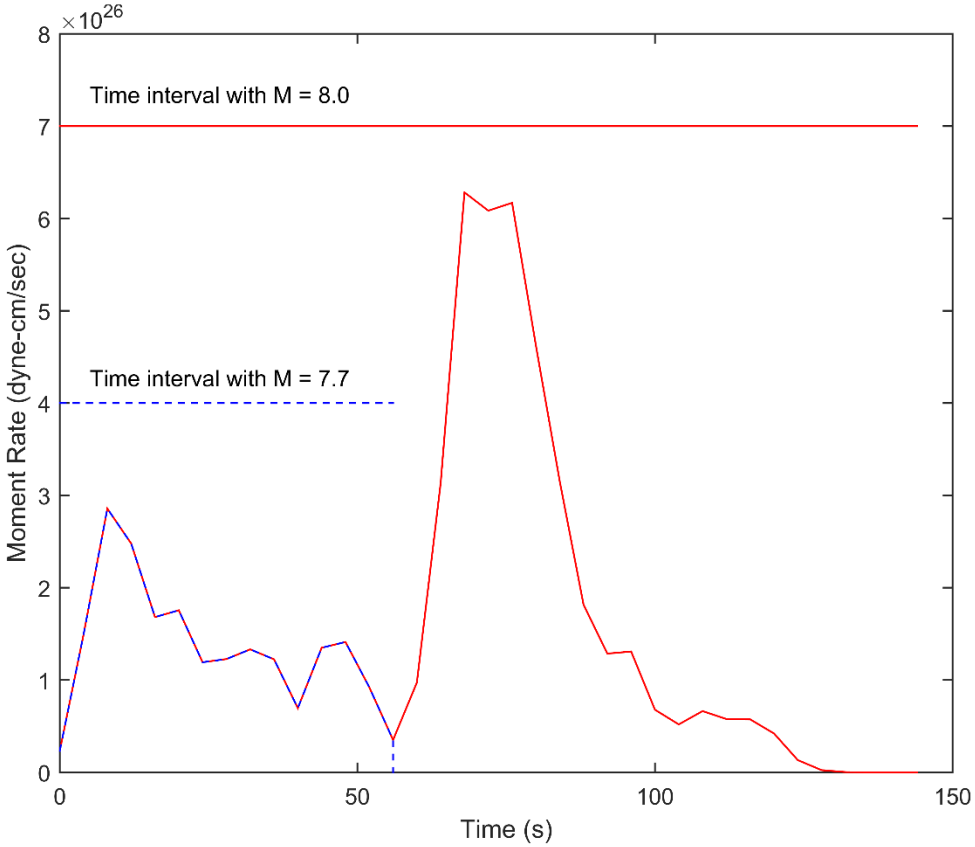

Figure 4.4: Moment rate time series for the 2007 Peru earthquake (from Hayes 2007). Note there are two high peaks which correspond with the two ruptures for this earthquake.

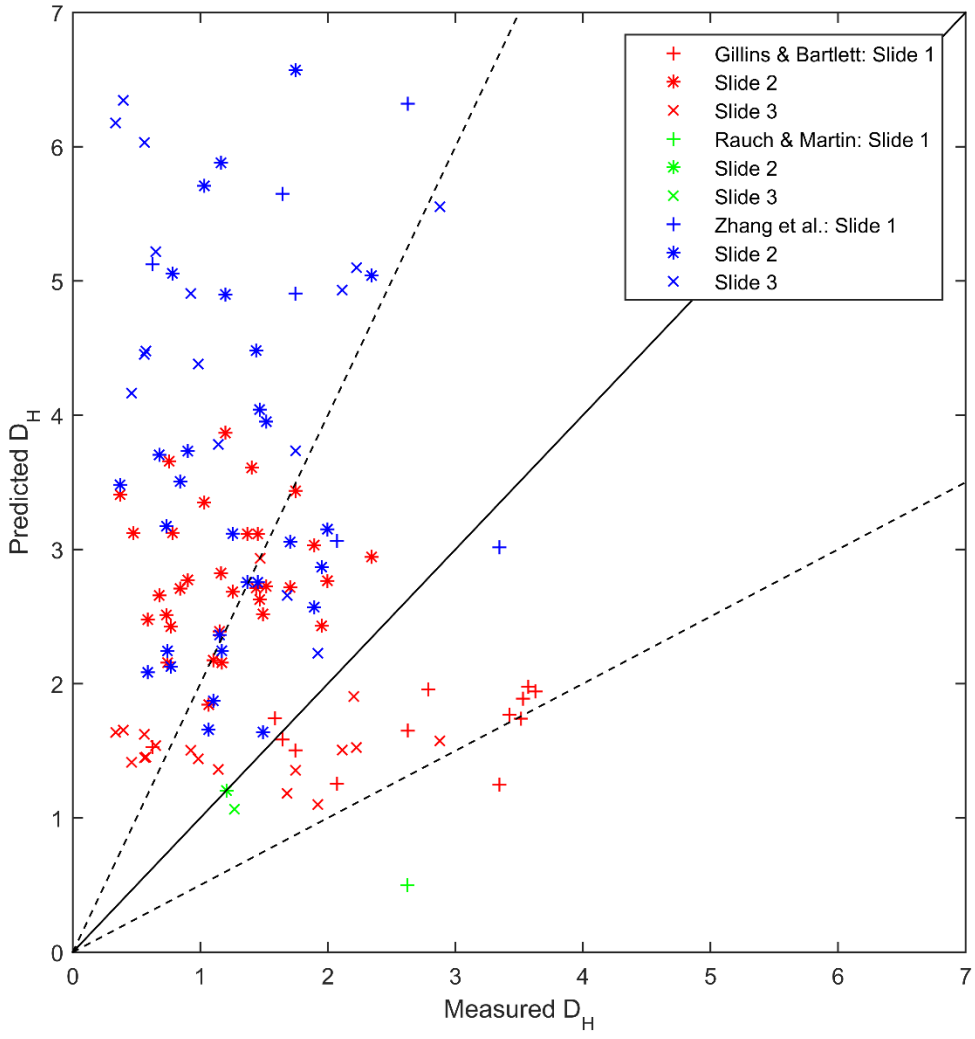

Figure 4.5: Re-evaluation of the Canchamana case history using an adjust M_w of 7.7.

Despite the noticeable improvement caused by adjusting the earthquake magnitude, there is not a diverse enough dataset to simply prove it as an adequate solution. Even if the magnitude were found to be the problem, there is no easy method for determining the timing of an earthquake's rupture before the event has even occurred. For

these reasons, it is important to assess what else may be responsible for the poor predictions using the Gillins and Bartlett (2014) equations.

Recall that the Canchamana site is situated within the Ji and Zeng (2007) fault plane, which implies a relatively small distance to seismic energy source, R. Despite this distance being small (approximately 20 km), it is by no means smaller than several of those used in the Gillins and Bartlett (2014) equations, which include case histories within 5 km of the seismic energy source. The difference is that the case histories incorporated by Gillins and Bartlett (2014) were crustal earthquakes.

Another parameter which could account for poor displacement predictions is T_{15}. Figure 4.6 shows mapped T_{15} thickness based on triangular irregular network (TIN) interpolation of the computed value at each boring. The values appear to describe the site well, with larger T_{15}s underlying the positions of the sliding masses. Based on the figure, the use of inverse distance weighting (IDW) during analysis gives borings with smaller T_{15} values greater weight than is probably correct. Displacements located near the middle of the figure (i.e. those most distant from the borings) receive similar influence from the borings near the left side of the marine terrace, as they do from those on the right side, despite being positioned on terrain much more similar to the latter borings. What this means is that a number of the displacements in Figure 4.3 are potentially under predicted, which does not aid in identifying the source of over prediction. Again, more datasets from similar conditions would be needed to verify this assertion, because it is possible for some bias to exist in the SPT results that influences all T_{15} values.

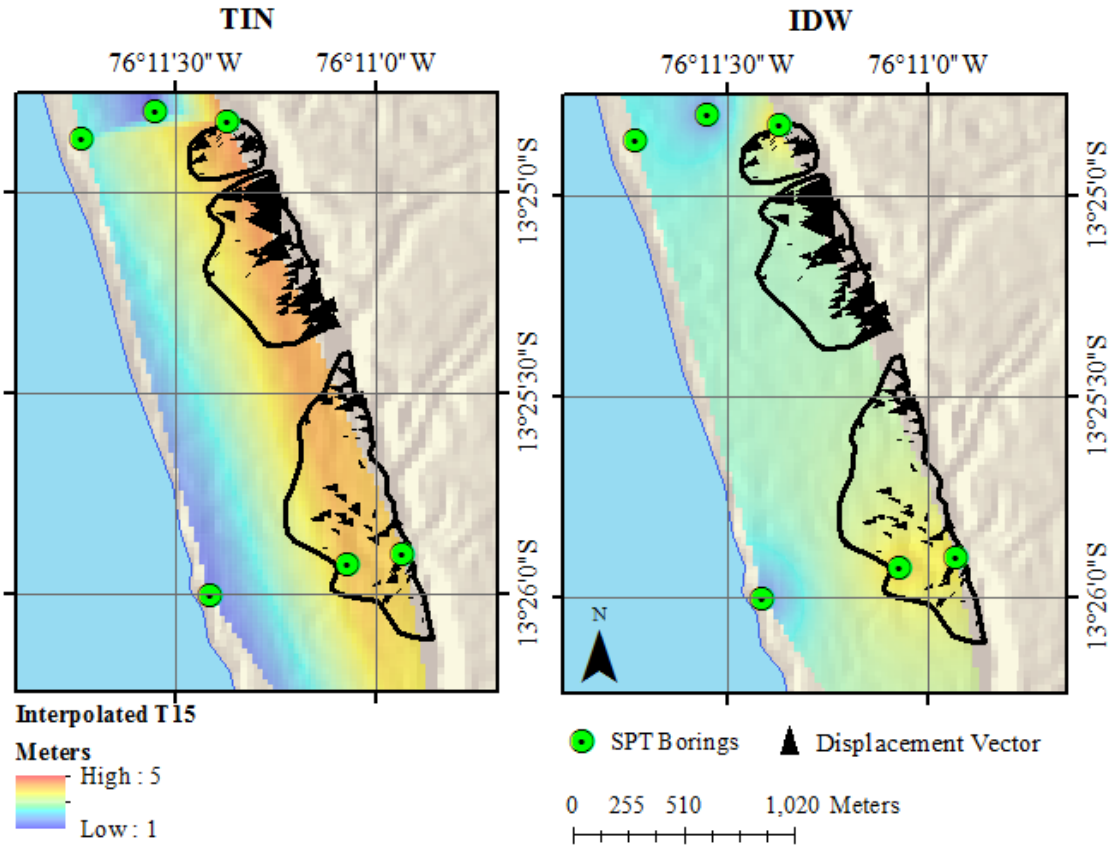

Figure 4.6: Comparison of TIN and IDW as methods of interpolating geotechnical parameters. Note that the T_{15} scale is identical for both images.

Rauch and Martin (2000)

Looking back at Figure 4.3, the Rauch and Martin (2000) equations appear to provide improved predictions for the Canchamana case history. Naturally, the fact that the Rauch and Martin results come from averaged slope and displacement values means that erratic predictions are less likely to occur, but it is possible that by averaging displacements, some potential bias is removed from any false displacements (i.e. artifacts from the image correlation) that passed through the filtering process.

It is likely that further improvement in the predictions comes as a result of Rauch and Martin adding parameters for the duration and amplitude (i.e. PGA) of ground motions. Both parameters provide more detail into the rupture process of this complicated earthquake, and help explain how energy was released from two ruptures. Such detail cannot be explained solely by using *M* and *R*. For a complex rupture, knowing how duration and PGA relate allows for the differentiation between individual strong ruptures and numerous weak ruptures.

The benefits of including more parameters are intuitive, but are only realized if the values in the regression database are similar to those used for analysis. Despite a limited amount of information on great magnitude earthquakes, the EPOLLS database does include several case histories from the 1964 Alaska earthquake, as briefly discussed in chapter 3. Table 4.1 compares several regression parameters from the Alaska earthquake to those used in the three new case histories. Acknowledging that no strong ground motion recordings actually exist for the Alaska earthquake (and thus PGA was estimated from attenuation models), it is still important to see that the values share some similarities, particularly with PGA and *R*. The improved performance of Rauch and Martin's equations for this case history is very likely attributed, at least in part, to the inclusion of these additional seismic parameters and additional sites from the Alaska earthquake.

Table 4.1: Comparison of select seismic parameters from the EPOLLS database with those used in this analysis.

Site	PGA (g)	Duration (s)	R (km)
Resurrection River, Alaska	0.52	88	31
Snow River, Alaska	0.47	87	35
Portage Creek	0.31	75	60
Ship Creek, Alaska	0.18	86	119
Matanuska River, Alaska	0.21	77	100
Canchamana, Peru	**0.35**	**68**	**20 (22)***
Mataquito Bridge, Chile	0.54	112	10 (18)*
Katori, Japan	0.30	68	100

* Values in parentheses represent R_{eq}, which was used in place of R for sites outside of the western U.S. and Japan (Youd et al. 2002).

The rupture of the 2007 Peru earthquake is a strong example for examining the effects of duration and PGA, considering its complex rupture. If, as hypothesized before, the second rupture played a limited role in the initiation of lateral spreading at Canchamana, then the inclusion PGA is expected to have better accounted for the strength of the first rupture. Regardless of the possible benefit of using PGA in this case, the Rauch and Martin equations counterintuitively precede the parameter with a negative coefficient. This difficulty will be discussed further in the next section.

Another parameter used in the Rauch and Martin equations worth discussing is the slide length. For the Canchamana site, slide length was determined by measuring the distance across each slide area in Figure 3.15 in the direction of displacement. For any of the three areas, the slide length could have just as easily been selected as half of the analyzed distance, and it is important to state that this value is difficult to select,

particularly when using satellite image derived displacements where surface cracking is not always visible.

Zhang et al. (2004)

The results obtained using the Zhang et al. (2004) method overestimate lateral spread displacements at this site, and as will be seen later, both other new case histories. Because this behavior is different than for the methods of Gillins and Bartlett (2014) and Rauch and Martin (2000), which each appear to provide good predictions for at least one case, less confidence is placed in the results.

Since no free face conditions were found in any of the new case histories, equation 2.16 was used to compute lateral spread displacements for the method of Zhang et al. (2004). The equation shows that the magnitude of displacements is a function of LDI and ground slope. Figure 4.7 uses vertical lines to show where the average value of these two parameters, as calculated for the Canchamana, Mataquito Bridge, and Katori case histories, lie in relation to the database of Zhang (2001) used to regress the equations of Zhang et al. (2004). The average values of both parameters are additionally provided for each site in Table 4.2.

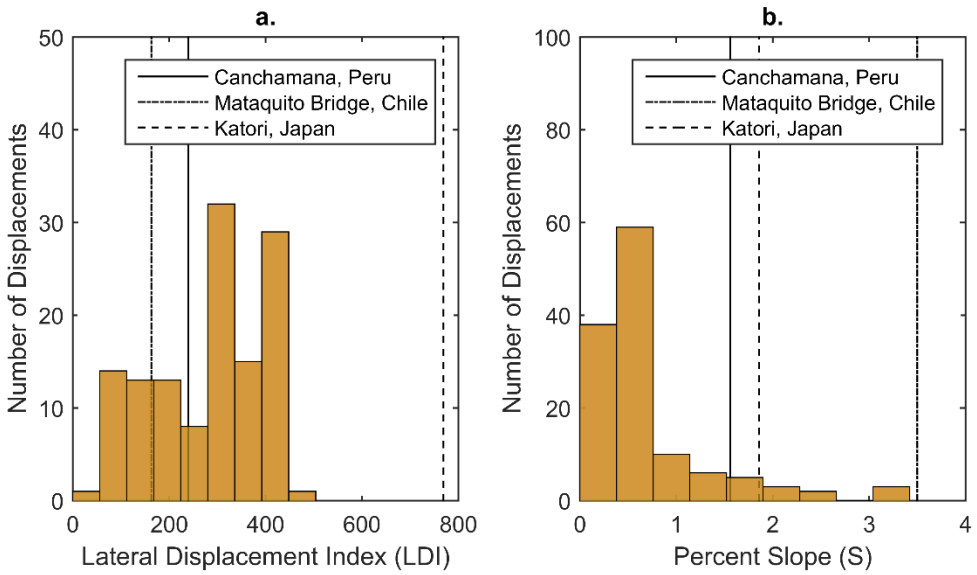

Figure 4.7: Histograms showing the distribution of (a) LDI and (b) slope within the database of Zhang (2001).

Table 4.2: Listing of average LDI and percent slope values for each new case history site.

Site	LDI	Average percent slope
Canchamana, Peru	240	1.6
Mataquito Bridge, Chile	163	2.5
Katori, Japan	769	1.9

Mataquito Bridge, Chile

Figure 4.8 provides an overview of the Mataquito Bridge site, including the approximate extent of liquefaction and the location where lateral displacement was measured. Unlike the satellite image correlations of the Canchamana and Katori case histories, ground deformation was measured directly by the Bray et al. (2010) team. As a result, there is only one displacement that may be analyzed, much like the case histories developed for the Great Alaska earthquake by Bartlett and Youd (1992b).

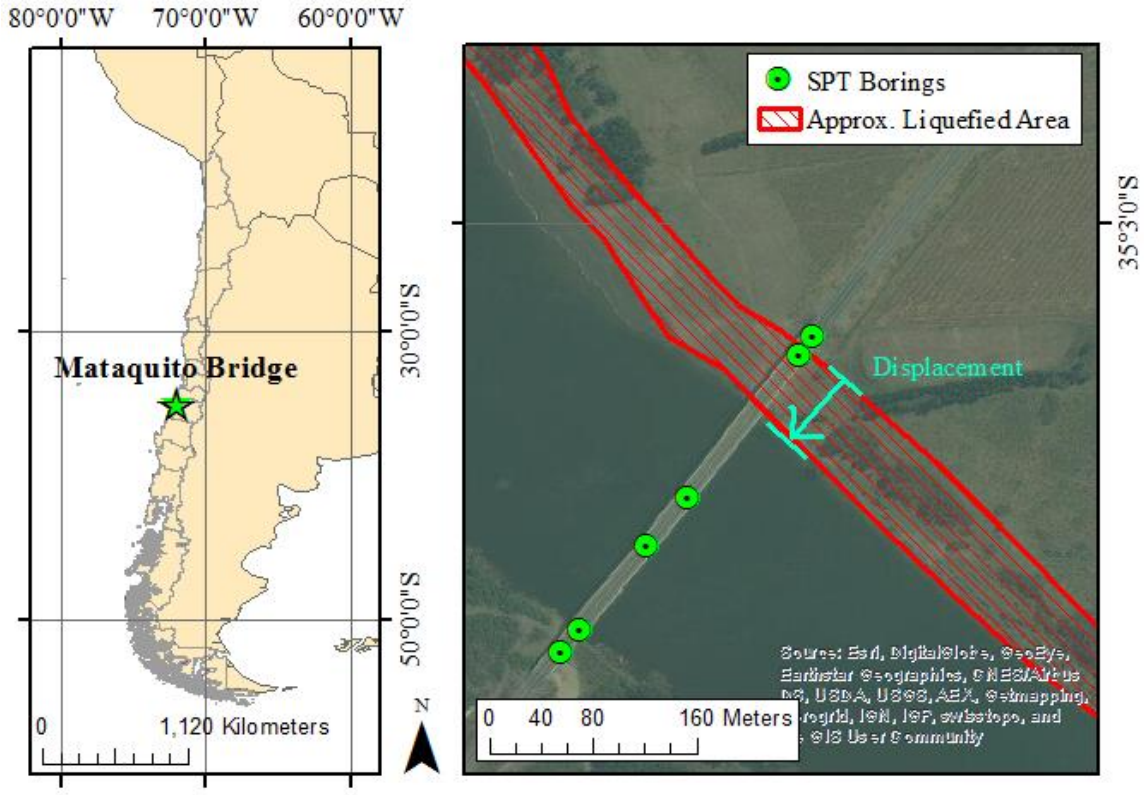

Figure 4.8: Overview of the Mataquito Bridge site.

Working with the displacement labeled in Figure 4.8, the Mataquito Bridge case history was used to evaluate the performance of the Rauch and Martin (2000) and Gillins and Bartlett (2014) empirical equations. Results of the analysis are presented in Figure 4.9.

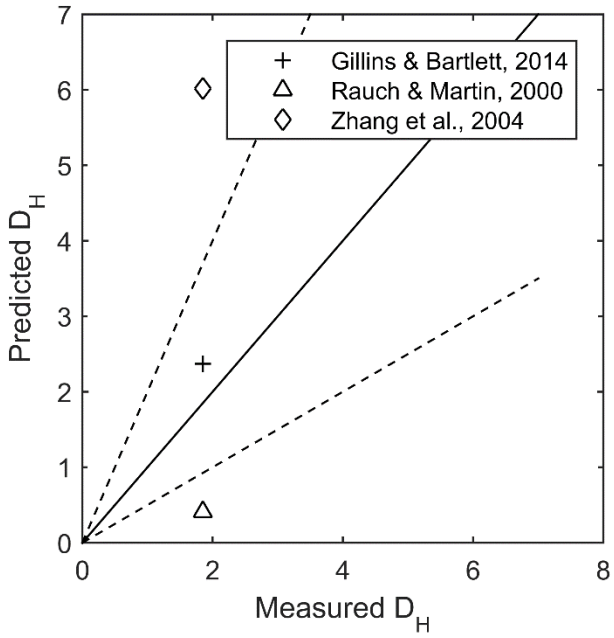

Figure 4.9: Comparison of predicted lateral spread displacements to that observed at the Mataquito Bridge.

A discussion of Figure 4.9 should first begin by considering the resistance introduced by the nearby bridge foundation. Despite the case history being documented similarly to the Alaska case histories of Bartlett and Youd (1992b), the scale and material composition of the Mataquito Bridge makes it a very different study. This difference becomes a concern considering that the Alaska case histories dealt with bridges built on timber piles, which Bartlett and Youd assumed to either break or be carried away in the presence of lateral spreading. The Mataquito Bridge rests upon 1.5 meter diameter concrete piers, which were not severely damaged during the earthquake (McGann and Arduino 2014). The same assumption made by Bartlett and Youd cannot be made in this

case, and the expectation is that the measured displacement is less than the deformation that would have occurred in a free field.

Gillins and Bartlett (2014)

As shown in Figure 4.9, the Gillins and Bartlett (2014) model predicts the lateral spread displacement at the Mataquito Bridge quite well. This may mean that the foundation effects mentioned in the previous paragraph were not actually significant for the Mataquito Bridge. The case histories used to develop the Gillins and Bartlett equations were selected by specifically omitting sites where structures were observed to restrict free lateral movement (Youd et al. 2002), but the expected confidence in the method does not allow for a conclusion to be made.

Based on the discussion of the Canchamana lateral spread in the previous section, another point of discussion comes from the lack of complexities in the earthquake's rupture. Recordings from the two nearest accelerometers to the Mataquito Bridge show a single peak in ground motions. Much like when the 2007 Peru earthquake was reevaluated for a single rupture, the already individual rupture of the Maule earthquake may help explain a good prediction from the Gillins and Bartlett (2014) model.

A final parameter worth discussing is the distance to the nearest seismic energy source, *R*. As *R* is equivalent for the methods of both Gillins and Bartlett (2014), and Rauch and Martin (2000), any effect of variation in the parameter must affect the results similarly. Since the methods yielded differing displacement predictions, it is not possible to identify how severe of a bias might exist. Mention of *R* is still warranted because of the disagreement between several displacement models described in chapter 3.

The value of *R* measured for the Mataquito Bridge was 10 km, approximately half that of the Canchamana site, and the shortest distance considered in this research. Because the site lies outside of the United States or Japan, a R_{eq} of 18 km was also determined according to the procedure of Youd et al. (2002), and used for analysis. Both the 10 and 18 km values yielded similar displacement predictions, and their variability is not considered to be a source of any significant error. A more plausible source of error is that the deformation model of Sladen et al. (2010) estimated that the pivot line (i.e. point of zero uplift or subsidence) was on the opposite side of the site than the selected deformation model. More confidence should still be placed in the Pulido et al. (2011) deformation model because it considers physical measurements made along the Chilean coastline, but the large disagreement between models presents insight into the amount of uncertainty. Further, the disagreement presents the question of whether or not an *R* measured in a region of subsidence should be treated the same as an *R* in a region of uplift. Earthquake directivity lends to the response that the orientation of *R* is also an important consideration.

Rauch and Martin (2000)

Figure 4.9 shows that the Rauch and Martin equations under predicted lateral spread displacements for the Mataquito Bridge site. As mentioned previously, this prediction is opposite of that from the Gillins and Bartlett equations, and provides relevance to exploring the parameters that set the two methods apart.

The most definitive parameters in the Mataquito Bridge case history likely relate to the earthquake's ground motions. Recall from equation 2.12, that parameters A_{max}

(PGA) and T_d (duration) have negative coefficients. Rauch and Martin (2000) regard these values as weaknesses of their method because they produce results that are counterintuitive to theoretical knowledge. A good explanation for why the displacement predictions were under estimated by the Rauch and Martin equations is that the PGA and duration for the Mataquito Bridge were significantly higher than those for the Canchamana site, where the equations performed well.

A final parameter to discuss is slide length. The values of 65 meters was taken from the report of Bray et al. (2010), and does not carry much confidence. Of most concern, the slide length was bounded on one side by the bridge abutment, and on the other side by the Mataquito River at the time of the GEER survey. Seasonal changes in river shorelines, and the possible occurrence of lateral spreading beneath the river mean that the slide length used in analysis could incorrect. Added difficulty comes from determining what slide length would be correct, or if the slide lengths used in the EPOLLS database are consistent themselves. Whatever the case may be, any expected change in slide length would be an increase, which would result in an improved lateral spread prediction.

Zhang et al. (2004)

As discussed in the earlier section about the Canchamana case history, the Zhang et al. (2004) equations overestimated lateral spread displacements for all three of the new case histories, and as a result carry little confidence. Readers interested in the method of Zhang et al. (2004) should refer to the previous section which discusses it for the Canchamana case history, and the accompanying Figure 4.7 for further detail.

Katori, Japan

Of the three original case histories presented in this work, the data from Katori, Japan, is regarded as having the highest quality. The site's location within 1 km of the nearest strong ground motion recording station means greater confidence in the ground motion parameters, and the network of numerous deep (>30m) borings is expected to have provided better geotechnical information. Despite this overall improvement of quality, the case history has three primary weaknesses: inconsistent topographic data, significant ground improvements including roads and buildings that may have pinned or impeded free-field lateral spread displacements, and a poorly understood site to source, *R*, value.

An overview of the site with respect to our analysis is presented in Figure 4.10. Slide areas were determined based on azimuth of displacement, and tend to agree well with expected topography. Unfortunately, erratic elevation values exist in slide area 1 on the 30 m SRTM digital elevation model obtained for the site. Incorrect elevations mean that slopes carry little confidence, and an attempt during analysis was made to mitigate the problem by filtering out displacements on slopes greater than 6 percent. The removed points have been reflected in what is being shown in the figure.

There is reasonable confidence of the displacements, as Martin (2014) obtained displacement vectors from ground surveys performed by the city of Katori, and used them to verify the values correlated in his analysis. Martin's comparison shows that the magnitude of displacements in slide area 3 best match those from the ground survey, although slide area 2 still shows reasonable agreement. The city of Katori did not perform ground surveys near slide area 1, and therefore the displacements have not been verified.

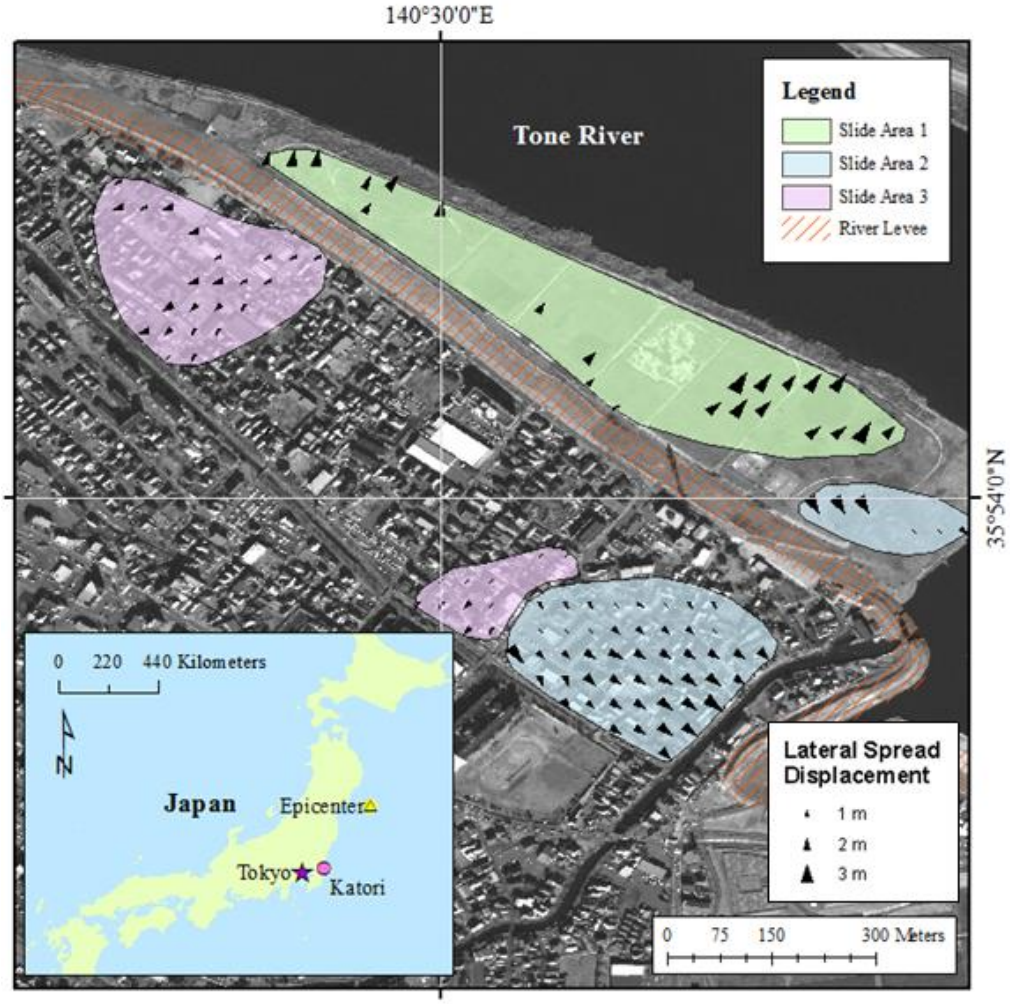

Figure 4.10: Overview of the Katori site.

The poor understanding of the parameter *R* comes from the geographic relationship between the site and the estimated pivot line of coseismic deformation. This problem is the result of the nearest distance to the pivot line occurring at an asymptote on the coseismic deformation contours, as shown in Figure 3.11. Selection of the location of intersection between a vector, *R*, and the pivot line can then possibly vary by dozens of km.

Figure 4.11 displays our results from analyzing the Gillins and Bartlett (2014) and Rauch and Martin (2000) equations for each of the three slide areas. The following paragraphs will discuss possible reasons for the general underestimate of displacements provided by both methods. Severe overpredictions of displacements are obtained from the Zhang et al. (2004) model and are also discussed below.

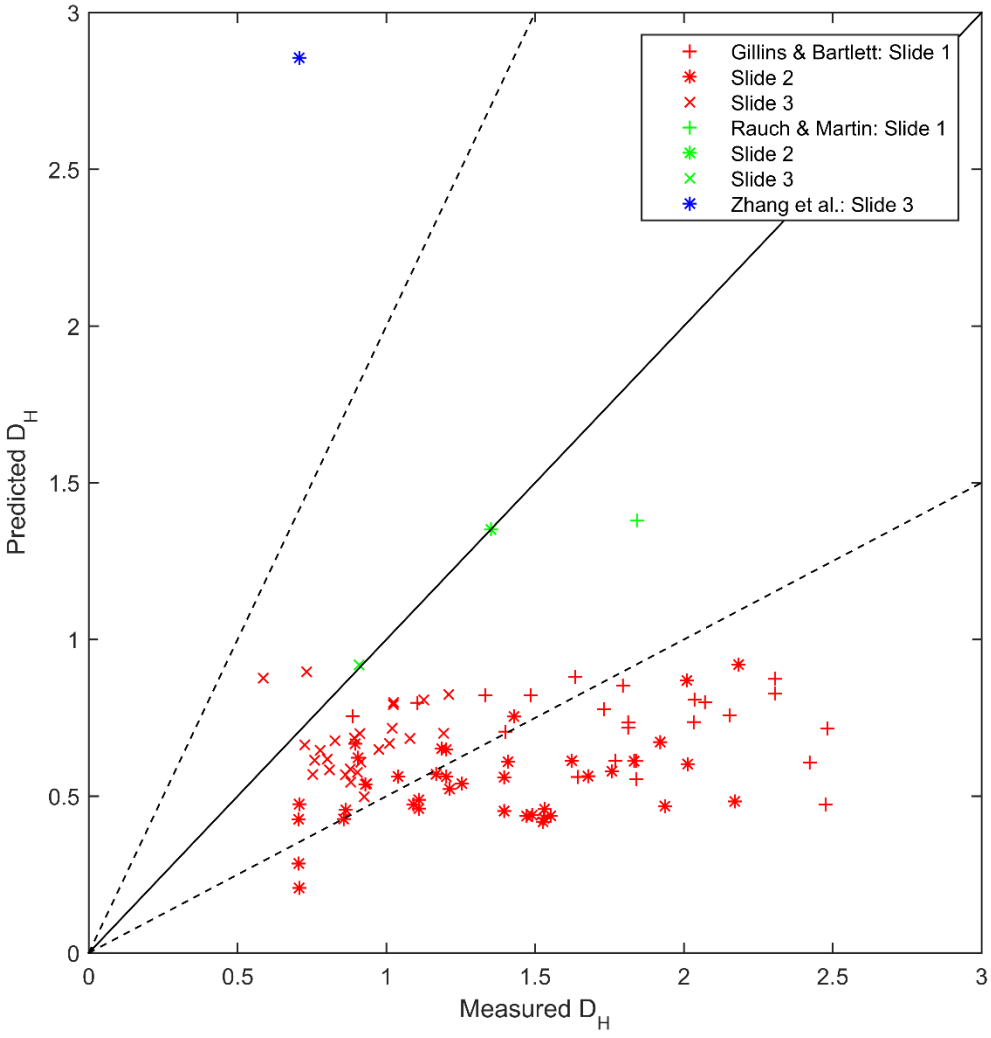

Figure 4.11: Comparison of predicted lateral spread displacements to that observed at Katori.

Gillins and Bartlett (2014)

Figure 4.11 shows that the Gillins and Bartlett equations under predict lateral spread displacements for all three of the slide areas at the Katori site. The best explanation for these under predictions comes from uncertainty of the *R* parameter discussed in the preceding section. Minor adjustments of *R* show that much better predictions can be obtained (i.e., within the 1:2 and 2:1 sloped lines in Figure 4.11); however, with no justification for one *R* over another, it is difficult to decide on a defensible value.

Another observation to be made about the Katori case history is that the average T_{15} is of a similar value to the highest values used in the Youd et al. (2002) database. If T_{15} was incorrectly overestimated, it would result in over predicted displacements, which does not correspond with Figure 4.11.

Rauch and Martin (2000)

The Rauch and Martin (2000) equations produce very good predictions for average lateral spread displacements at all 3 slide areas at Katori. Based on the expected source of under predictions from the Gillins and Bartlett (2014) method, improved results are likely explained by the incorporation of PGA and duration, which reduce the influence of *R*.

Another explanation for the better performance of the Rauch and Martin (2000) equations comes with the method's averaging of displacements and slopes within each slide mass. By averaging values across a slide mass, the analysis is less susceptible to noise which may be present in the satellite imagery and could be considered an

improvement. There is a problem with this approach though, and that is that it removes much of the potentially insightful variability in the displacements within a slide area. The Rauch and Martin (2000) model will provide an average displacement across an entire slide area, but as can be seen in Figure 4.10, there is variability in the magnitude of sliding within each slide area. This shortcoming may also be the reason behind the poor prediction at the Mataquito Bridge, which involved one specific location.

Zhang et al. (2004)

As discussed in the earlier section about the Canchamana case history, the Zhang et al. (2004) equations overestimated lateral spread displacements for all three of the new case histories, and as a result carry little confidence. Readers interested in the method of Zhang et al. (2004) should refer to the Canchamana section, and the accompanying Figure 4.7 for further detail.

Only one displacement analyzed using Zhang et al. (2004) is presented in Figure 4.11. All other displacements with slopes less than 3.5 percent were evaluated, but none of them were predicted to be less than 3 m by the equation.

Chapter 5: Conclusions and Recommendations

Summary

Predicting the magnitude of lateral spread displacements has been an important area of geotechnical earthquake engineering research over recent decades, and the outcomes have become valuable tools for practicing engineers in earthquake-prone regions. Unfortunately, many of the conditions that contribute to lateral spreading are

poorly understood, or prohibitively complex in theory and scale. For these reasons, several empirically-derived equations have become popular due to their ease of implementation and reasonable performance when verified against the information from which they were derived.

The fundamental difficulty with these empirical equations is that they are expected to only be capable of making predictions when conditions are similar to those used in their development. A test for the equations then comes from great earthquakes, of which only the 1964 Great Alaska earthquake has currently been incorporated. Considering relative infancy of geotechnical earthquake engineering in 1964, the Alaska earthquake is best viewed with less confidence due to data that is of a low or dated quality, or is altogether unavailable.

Earlier in this report, detail was provided for the development of three new case histories. All three case histories are of sites that had been impacted by great earthquakes during the past decade and consist of data from numerous sources, existing in varying qualities, with no single case exemplifying the consistently high quality data that would provide the confidence or bulk of information necessary to form a robust database for great earthquakes. Despite their shortcomings, each case helped to identify weaknesses in the existing empirical models, and did well to showcase the ways in which a great subduction zone earthquake is, and is not, like a smaller crustal event.

Conclusions

This research was performed in two distinct parts. First, the Great Earthquake Lateral Spread Case History (GELCH) database was compiled, and second, the GELCH database was used to evaluate the performance of existing empirical models for

predicting lateral spread displacements. Both parts carry their own conclusions, and will be discussed separately.

Conclusions associated with building the GELCH database are as follows:

1. Although lateral spreads have been frequently noted following recent great earthquakes, the amount of lateral movement is rarely carefully measured or reported. There is generally a higher possibility of other necessary data (i.e. topography, ground motions, and subsurface investigations) from alternative sources being nearby, and applicable for the site; oddly, the lateral displacements tend to be rarely reported which reduces the number of available lateral spreading case histories for analysis. This problem could be overcome by performing post-earthquake surveys and reconnaissance with the specific goal of building complete lateral spread case histories. As noted in the next conclusion, numerous technologies exist for high-accuracy and high-resolution surveys of lateral spread displacements.

2. Topographic data was generally among the lowest quality of all information used in our case history evaluations for this study. For the Canchamana and Katori case histories, slopes were obtained using digital elevation data with coarse (30 m) resolution obtained from satellite imagery. This problem was greater for the predictive equations that examined each individual displacement vector (e.g., Gillins and Bartlett (2014) model), than for the Rauch and Martin (2000) equations, which average values across a soil mass and appears to be less susceptible to noise in the topographic model. The lack of high-accuracy topographic data underscores the importance of performing surveys of lateral spreading sites after an extreme event.

Better yet, if such surveys were also performed before an event, then accurate displacements could be readily found by comparing pre and post-event survey data. Numerous modern technologies such as GPS/GNSS, LiDAR, and structure-from-motion are available for rapidly performing highly detailed, centimeter to sub-centimeter accuracy, 3D topographic surveys. Of course, high-accuracy topographic surveys must be coupled with subsurface explorations in order to develop a full case history. For this research, LiDAR data was obtained at other great earthquake sites as part of this research, but the lack of nearby subsurface information meant that the LiDAR data could not be used to develop a case history for evaluating the lateral spreading empirical models.

3. Commonly found geotechnical subsurface information existed in the form of standard penetration test (SPT) results with soil descriptions, or unaccompanied shear wave velocity profiles. Very little cone penetration test (CPT) data was available, and laboratory results for index parameters, such as *D50* and fines content, were nearly nonexistent. Ideally, more shear-wave velocity and CPT measurements should be taken at case history sites to characterize subsurface conditions and vastly improve the lateral spreading case history database. Such data is nearly continuous with depth and is well-correlated with liquefaction potential.

Conclusions associated with existing empirical equations are as follows:

1. The values estimated as inputs for each of the empirical models (R, Z_{liq}, T_{15}, etc.) were generally not excessively high when comparing the GELCH values with the range of values in the existing lateral spreading case history databases. An

obvious exception is the earthquake magnitude for all GELCH case histories are much greater, and less obvious, the geotechnical values for Katori are generally thicker.

2. The method of Youd et al. (2002) could not be applied to two of the three case histories due to a lack of available fines and grain size information. For the case with available data, the results of Youd et al. (2002) are similar, but not exactly the same, as those obtained using the method of Gillins and Bartlett (2014).
3. Neither the method of Rauch and Martin (2000), nor that of Gillins and Bartlett (2014) provide good predictions for all three case histories, but they do perform well at least once. Rauch and Martin (2000) performed well on the Katori case history, while Gillins and Bartlett (2014) performed well on the Mataquito Bridge case history. The method of Zhang et al. (2004) resulted in over predicted displacements for all three sites.
4. The parameters, Z_{FSmin} and T_{15}, from Rauch and Martin (2000) and Gillins (2014), respectively, are sensitive to small changes in SPT N-value, which may dramatically alter lateral spread predictions. For example, if a liquefiable layer of soil has an $(N_1)_{60}$ value equal to 16, it is omitted from the calculation of T_{15}. This problem is particularly important for cases like Canchamana, where the quality of SPT data is questionable. A parameter, such as the lateral displacement index (*LDI*) from Zhang et al. (2004), which integrates values for the depth of a boring, is expected to be less sensitive. However, the results from this research do not provide enough evidence that the Zhang et al. (2004) model is appropriate for predicting lateral spread displacements due to great subduction zone earthquakes.

5. The complex rupture processes behind great subduction zone earthquakes are much different than crustal earthquakes which were predominantly used for developing the lateral spreading case history databases and current empirical models. For great earthquakes, ruptures may occur in multiple locations separated by significant distances, and it is possible that liquefaction and lateral spreading occurs as a result of individual ruptures, and not the entire earthquake. These complexities do not make great earthquakes conducive to predictions based on empirical models because the location, duration, timing of rupture, and pivot line between subsidence and uplift are very difficult to predict. This conclusion is exemplified by Kramer et al. (1998), who considered 30 possible Cascadia Subduction Zone earthquakes in an effort to estimate ground motions throughout Washington State.
6. From the previous conclusion, and as evidenced in Canchamana, moment magnitude (M_w), which is a function of the total amount of energy released during an earthquake, may not adequately model the seismicity that initiated lateral spreading at a site.
7. The distance *R*, which was originally defined by Bartlett and Youd (1992b) and is used in the empirical models of Youd et al. (2002), Rauch and Martin (2000) and Gillins and Bartlett (2014), can differ significantly based on how regional coseismic deformation is estimated. In terms of applying any existing empirical method to predict lateral spread displacements, it is very difficult to know coseismic ground deformations in order to predict the location of the pivot line between subsidence and uplift in advance of a subduction zone earthquake.

Therefore, it is very difficult to model a defensible value for *R* for great earthquakes. In addition, *R* does not account for which direction energy was released during a subduction zone event.

8. Peak ground acceleration (PGA) and duration of shaking both provide site-specific detail concerning the complex rupture of a great earthquake, but are problematic in the Rauch and Martin (2000) equations because of their counterintuitive negative coefficients for lateral spread predictions. This problem may explain the under predicted displacements at the Katori case history in the GELCH database. Further research is recommended to develop new models based on PGA and duration of shaking.
9. The slide length parameter from Rauch and Martin (2000) can vary by a factor of two based on how a user interprets the extent of a sliding mass, which has a significant effect on lateral spread predictions. Additionally, for many cases the parameter is impossible for an engineer to estimate in practice when the ground has not yet deformed.

Recommendations

None of the current empirical/semi-empirical models for predicting lateral spread displacements appear to consistently work well for predicting displacements occurring during great subduction zone earthquakes. Based on the findings of this report, an improved model would require further subduction zone case histories for great earthquakes and a reselection of regression parameters. The development of new case histories would require post-earthquake surveys and reconnaissance with a focus on collecting the following information:

1. Site topography: average ground slope within several meters of the displacement and the height and distance to a nearby free face (if applicable). This information is easily measured using traditionally survey equipment, such as a digital level or total station, but a practical recommendation would be the use of survey-grade GPS/GNSS. More ideally, LiDAR or photogrammetry could also be used to develop a full 3D model of the site for detailed analyses.
2. Magnitude of displacement: measurements of the horizontal movement of surficial soil, either by summing the width of visible cracks on site using conventional survey methods, or from using LiDAR or photogrammetry survey data. Oddly, such data is rarely reported in the literature.
3. Subsurface data: results from in-situ and laboratory geotechnical tests. At a minimum, these include standard penetration test (SPT) blowcounts and soil descriptions, but it is beneficial to also include particle size distribution curves for each soil layer encountered. More ideally, cone penetration tests (CPTs) and shear wave velocity tests should be performed to collect near-continuous geotechnical measurements with depth. Such near-continuous data will greatly improve the characterization of the subsurface.
4. Earthquake strength: earthquake magnitudes and nearby ground motions can be obtained after the earthquake. Sites of similar soil condition that are located nearer to recorded ground motions should be given precedence when selecting case histories. Full acceleration time-series are recommended for great earthquakes because they provide further insight and detail into the complex rupture timing.

The primary purpose of reselecting regression parameters is to overcome the uncertainties caused by complex earthquake ruptures. To accomplish this task, it is recommended to remove earthquake magnitude and the parameter *R* from analyses. Local ground motions are not only a better reflection of how an earthquake is felt at a particular site, but they are becoming more widely available for the design earthquakes that an engineer may use in practice. Although not proven, the anticipated effect of regressing PGA and duration, without magnitude and *R*, is that the negative coefficients observed by Rauch and Martin (2000) would become positive. It is important to mention that due to a lack of recording stations and limited seismic data at the time, Bartlett and Youd (1992) used available *M* and *R* to approximate PGA and duration of shaking.

Currently, based on these research findings and recommendations, we are developing a proto-type model for predicting lateral spread displacements due to subduction zone earthquakes. However, such a model will be based on a limited number of case histories. The most important outstanding work to date is the need to collect more, detailed lateral spreading case history data after subduction zone earthquakes.

References

Ashford, S.A., Boulanger, R.W., Donahue, J.L., and Stewart, J.P., 2011. Geotechnical quick report on the Kanto plain region during the March 11, 2011 off Pacific coast of Tohoku earthquake, Japan, *Quick Report 1*, GEER Association.

Bardet, J.P., Tobita, T., Mace, N., and Hu, J., 2002. Regional modeling of liquefaction-induced ground deformation, *Earthquake Spectra*, 18(1), 19-46.

Bartlett, S.F., and Youd, T.L., 1992a. Empirical analysis of horizontal ground displacement generated by liquefaction-induced lateral spreads, *Technical Report NCEER-92-0021*, National Center for Earthquake Engineering Research, Buffalo, NY.

Bartlett, S.F., and Youd, T.L., 1992b. Case histories of lateral spreads caused by the 1964 Alaska Earthquake, Volume 2, *Technical Report NCEER-92-0002*, National Center for Earthquake Engineering Research, Buffalo, NY.

Bartlett, S.F., and Youd, T.L., 1995. Empirical prediction of liquefaction-induced lateral spread, *Journal of Geotechnical Engineering*, 121(4), 316-329.

Boroschek, R., Soto, P., and Leon, R., 2010. Maule Region Earthquake: February 27, 2010 Mw = 8.8, *RENADIC Report 10/08 Revision 2*. University of Chile Faculty of Mathematics and Physical Sciences, Civil Engineering Department.

Boroschek, R.L., Contreras, V., Kwak, D.Y., and Stewart, J.P., 2012. Strong Ground Motion Attributes of the 2010 M_w 8.8 Maule, Chile, Earthquake, *Earthquake Spectra*, 28(S1), S19-S38.

Boulanger, R.W., and Idriss, I.M., 2010. CPT and SPT Based Liquefaction Triggering Procedures, *Center for Geotechnical Modeling*, Report No. UCD/CGM-14-01, University of California Davis, Davis, CA.

Bray, J., and Frost, D., 2010. Geo-engineering Reconnaissance of the 2010 Maule, Chile Earthquake, *GEER Association*.

Cox, B.R., 2014, Personal communication.

Cox, B.R., Cothren, J., Barnes, A., Wartman, J., Rodriguez-Marek, A., and Meneses, J., 2011. Towards quantifying movement of a massive lateral spread using high resolution satellite image processing.

DOGAMI, 2013. Cascadia Subduction Zone earthquakes: A magnitude 9.0 earthquake scenario, *Open-File Report 0-13-22*, Oregon Department of Geology and Mineral Industries, Portland, OR.

Farias, M., Vargas, G., Tassara, A., Carretier, S., Baize, S., Melnick, D., and Bataille, K., 2010. Land-Level Changes Produced by the M_w 8.8 Chilean Earthquake, *Science*, 329(5994), p. 916.

Faris, A.T., Seed, R.B., Kayen, R.E., and Wu, J., 2006. A semiempirical model for the estimation of maximum horizontal displacement due to liquefaction-induced lateral spreading, *Managing Risk in Earthquake Country (8NCEE): Proceedings of the 8th U.S. Conference on Earthquake Engineering*, Volume 3, Earthquake Engineering Research Institute, Oakland, CA, 1584-1593.

Fletcher, G.F.A., 1965. Standard penetration test: its uses and abuses, *Journal of the Soil Mechanics and the Foundations Division*, 91(4), 67-75.

Gillins, D.T, 2012. Mapping the Probability and Uncertainty of Liquefaction-induced Ground Failure, *Phd dissertation*, University of Utah, Salt Lake City, UT.

Gillins, D.T, and Bartlett, S.F., 2014. Multilinear Regression Equations for Predicting Lateral Spread Displacement from Soil Type and Cone Penetration Test Data, *Journal of Geotechnical and Geoenvironmental Engineering*, 140(4).

Hamada, M., and O'Rourke, 1992. Case studies of liquefaction and lifeline performance during past earthquakes, Volume 1: Japanese Case Studies, *Technical Report NCEER-92-0001*, National Center for Earthquake Engineering Research, Buffalo, NY.

Hamada, M., Yasuda, S., Isoyama, R., and Emoto, K., 1986. Study on liquefaction induced permanent ground displacements, Association for the Development of Earthquake Prediction in Japan, Tokyo.

Hayes, G., 2010. Updated result of the Feb 27, 2010 Mw 8.8 Maule, Chile Earthquake, *U.S. Geological Survey Earthquake Hazards Program.* <http://earthquake.usgs.gov/earthquakes/eqinthenews/2010/us2010tfan/finite_fault.php>.

Hayes, G., 2011. Updated result of the Mar 11, 2011 Mw 9.0 earthquake offshore Honshu, Japan, *U.S. Geological Survey Earthquake Hazards Program*. <http://earthquake.usgs.gov/earthquakes/eqinthenews/2011/usc0001xgp/finite_fault.php>.

Idriss, I.M., and Boulanger, R.W., 2010. SPT-based Liquefaction Triggering Procedures, *Center for Geotechnical Modeling*, Report No. UCD/CGM-10-02, University of California Davis, Davis, CA.

INGEMMET, 2008. Hazard Map of Pisco and San Andrés, *Geological, Mining, and Metallurgical Institute*. (in Spanish).

Ji, C., and Zeng, Y., 2007. Preliminary Result of the Aug 15, 2007 Mw 8.0 Coast of Central Peru Earthquake, *U.S. Geological Survey Earthquake Hazards Program*. <http://earthquake.usgs.gov/earthquakes/eqinthenews/2007/us2007gbcv/finite_fault.php>.

Kelson, K., Witter, R.C., Tassara, A., Ryder, I., Ledezma, C., Montalva, G., Frost, D., Sitar, N., Moss, R., and Johnson, L., 2012. Coseismic Tectonic Surface Deformation during the 2010 Maule, Chile, M_w 8.8 Earthquake, *Earthquake Spectra*, 28(S1). S39-S54.

Koketsu, K., and Kikuchi, M., 2000. Propogation of seismic ground motion in the Kanto Basin, Japan, *Science*, 288(5469), 1237-1239.

Kramer, S.L., 1996. Geotechnical Earthquake Engineering, *Prentice Hall*, Upper Saddle River, NJ.

Kramer, S.L., Silva, W.J., and Baska, D.A, 1998. Ground Motions Due to Large Subduction Zone Earthquakes, *Washington State Department of Transportation*, Research Report WA-RD 450.1.

Kulhawy, F.H., and Mayne, P.W., 1990. Manual on estimating soil properties for foundation design, *Report No. EL-6800*, Electric Power Research Institute (EPRI).

Ledezma, C., Hutchinson, T., Ashford, S.A., Moss, R., Arduino, P., Bray, J.D., Olson, S., Hashash, Y.M.A., Verdugo, R., Frost, D., Kayen, R., and Rollins, K., 2012.

Effects of Ground Failure on Bridges, Roads and Railroads, *Earthquake Spectra*, 28(S1). S119-S143.

Lorito, S., Romano, F., Atzori, S., Tong, X., Avallone, A., McCloskey, J., Cocco, M., Boschi, E., and Piatanesi, A., 2011. Limited overlap between the seismic gap and coseismic slip of the great 2010 Chile earthquake, *Nature Geoscience*, 4(3), 173-179.

Martin, J.G., 2014. Measuring liquefaction-induced deformation from optical satellite imagery, *Master's Thesis*, University of Texas, Austin, TX.

McCulloch, D.S., Bonilla, M.G., 1970. Effects of the earthquake of March 27, 1964 on the Alaska railroad, *U.S. Geological Survey Professional Paper 545-D.*

McGann, C.R., and Arduino, P., 2014. Numerical Assessment of Three-Dimensional Foundation Pinning Effects during Lateral Spreading at the Mataquito River Bridge, *Journal of Geotechnical and Geoenvironmental Engineering*, 140(10).

MOP, 2007. Puentes Mataquito y Llico consolidan Ruta Costera en la Región, Boletin Electronico, *Ministerio de Obras Públicas, Gobierno de Chile*, Marzo 2007.

MOP, 2012. Estudio Hidrogeológico Cuenca del Río Mataquito, *Aquaterra Ingenieros Limitada, Report No. 296*, Santiago, Chile.

National Research Institute for Earth Science and Disaster Prevention (NIED), 2013. Strong-motion seismograph networks. < http://www.kyoshin.bosai.go.jp/> (July 9, 2015).

NCEER, 1997. Proceedings of the NCEER Workshop on Evaluation of Liquefaction Resistance of Soils, *National Center for Earthquake Engineering Research,* Technical Report NCEER-97-0022.

ODOT, 2014. Geotechnical design manual, Volume 1, *Oregon Department of Transportation.*

Olson, S.M., and Johnson, C.I., 2008. Analyzing liquefaction-induced lateral spreads using strength ratios, *Journal of Geotechnical and Geoenvironmental Engineering*, 134(8), 1035-1049.

Petrus Consultores Geotecnicos, 2006. Informe complementario de mecánica de suelos, Puente Mataquito (Ruta Costera), Camino Quivolgo-Iloca (Cruce J-60), *Infrome No. 2619-ING-SGC-150/2006 (Rev 1)*, Petrus Consultores Geotecnicos, Santiago, Chile.

Plafker, G., and Galloway, J.P., 1989. Lessons learned from the Loma Prieta, California, earthquake of October 17, 1989, *U.S. Geological Survey Circular 1045*.

Pradel, D., Wartman, J., and Tiwari, B., 2014. Impact of anthropogenic changes on liquefaction along the Tone River during the 2011 Tohoku earthquake, *Natural Hazards Review*, 15(1), 13-26.

Pulido, N., Yagi, Y., Kumagai, H., and Nishimura, N., 2011. Rupture process and coseismic deformations of the 27 February 2010 Maule earthquake, Chile, *Earth, Planets, and Space*, 63, 955-959.

Rauch, A.F., 1997. EPOLLS: an empirical method for predicting surface displacements due to liquefaction-induced lateral spreading in earthquakes. *PhD dissertation*, Virginia Polytechnic Institute and State University, Blacksburg, VA.

Rauch, A.F., and Martin, J.R., 2000. EPOLLS model for predicting average displacements on lateral spreads, *Journal of Geotechnical and Geoenvironmental Engineering*, 126(4), 360-371.

Rodriguez-Marek, A., Hurtado, J.A., Cox, B., Meneses, J., Moreno, V., Olcese, M., Sancio, R., Wartman, J., 2007. Preliminary Reconnaissance Report on the Geotechnical Engineering Aspects of the August 15, 2007 Pisco, Peru Earthquake, GEER Association.

Ross, G.A., Seed, H.B., and Migliaccio, R.R., 1973. Performance of highway bridge foundations, *The Great Alaska Earthquake of* 1964, Engineering Volume, National Academy of Sciences, Washington, D.C., 190-242.

Serrano, C., 2014, Personal communication.

Shao, G., Li, X., Zhao, X., Yano, T., and Ji, C., 2010. Preliminary slip model of the Feb 27, 2010 Mw 8.9 Maule, Chile Earthquake, *National Earthquake Information Center of the U.S. Geological Survey.* <http://www.geol.ucsb.edu/faculty/ji/big_earthquakes/2010/02/27/chile_2_27.htmh>.

Shao, G., Li, X., Ji, C., and Maeda, T., 2011. Focal mechanism and slip history of the 2011 M_w 9.1 off the Pacific coast of Tohoku Earthquake, constrained with teleseismic body and surface waves, *Earths Planets Space*, 63. 559-564.

Sladen, A., 2010. Preliminary Result 02/27/2010 (Mw 8.8), Chile, *Caltech Tectonics Observatory*. < http://tectonics.caltech.edu/slip_history/2010_chile/index.html>.

Sladen, A., Tavera, H., Simons, M., Avouac, J.P., Konca, A.O., Perfettini, H., Audin, L., Fielding, E.J., Ortega, F., and Cavagnoud, R., 2010. Source model of the 2007 M_w 8.0 Pisco, Peru earthquake: Implications for seismogenic behavior of subduction megathrusts, *Journal of Geophysical Research*, 115, BO2405.

SCDOT, 2010. Geotechnical design manual, version 1.1, *South Carolina Department of Transportation.*

Tavera, H., Bernal, I., Strasser, F.O., Arango-Gaviria, M.C., Alarcón, J.E., and Bommer, J.J., 2009. Ground motions observed during the 15 August 2007 Pisco, Peru, earthquake, *Bulletin of Earthquake Engineering*, 7(1), 71-111.

Tsukamoto, Y., Kawabe, S., and Kokusho, T., 2012. Soil liquefaction observed at the lower stream of Tonegawa river during the 2011 off the Pacific Coast of Tohoku Earthquake, *Soils and Foundations*, 52(5), 987-999.

USGS, 2015a. M9.3-Southern Alaska Earthquake, *Earthquake Hazards Program*, U.S. Geological Survey. <http://earthquake.usgs.gov/earthquakes/eventpage/iscgem869809#general_summary>.

USGS, 2015b. M9.0-Near the east coast of Honshu, Japan, *Earthquake Hazards Program*, U.S. Geological Survey. <http://earthquake.usgs.gov/earthquakes/eventpage/usp000hvnu#general_summary>.

USGS. Shuttle Topography Mission, 1-arc second scene n35_e140_1arc_v3, 2011. <http://earthexplorer.usgs.gov/>.

Verdugo, R., Sitar, N., Frost, J.D., Bray, J.D., Candia, G., Eldridge, T., Hashash, Y., Olson, S.M., and Urzua, A., 2012. Seismic Performance of Earth Structures

during the February 2010 Maule, Chile, Earthquake: Dams, Levees, Tailings Dams, and Retaining Walls, *Earthquake Spectra*, 28(S1). S75-S96.

Wald, D.J., Worden, B.C., Quitoriano, V., and Pankow, K.L., 2006. ShakeMap Manual, *Advanced National Seismic System*, Version 1.0. < http://pubs.usgs.gov/tm/2005/12A01/>.

Wei, S., and Sladen, A., 2011. Updated result: 3/11/2011 (Mw 9.0), Tohoku-oki, Japan, *Caltech Tectonics Observatory*. <http://tectonics.caltech.edu/slip_history/2011_taiheiyo-oki/index.html>.

Youd, T.L., Hansen, C.M., and Bartlett, S.F., 2002. Revised multilinear regression equations for prediction of lateral spread displacement, *Journal of Geotechnical and Geoenvironmental Engineering*, 128(12), 1007-1017.

Youd, T.L., and Perkins, D.M., 1987. Mapping of liquefaction severity index, *Journal of Geotechnical Engineering*, 113(11), 1374-1392.

Zhang, G., 2001. Estimation of Liquefaction-induced Ground Deformations by CPT & SPT-based Approaches, *PhD dissertation*, University of Alberta, Edmonton.

Zhang, G., Robertson, P.K, and Brachman, R.W., 2004. Estimating liquefaction-induced lateral displacements using the standard penetration test or cone penetration test, *Journal of Geotechnical and Geoenvironmental Engineering*, 130(8), 861-871.